AN INTEGRATED ISOTOPIC/PHYSICAL APPROACH TO A NUMERICAL MODEL OF GROUNDWATER FLOW IN THE SAN JUAN BASIN

by

Fred M. Phillips
Principle Investigator
Department of Geoscience

and

Michael K. Tansey
Graduate Research Assistant
Department of Geoscience

TECHNICAL COMPLETION REPORT
Project Nos. 1345668 & 1423606

December 1984

New Mexico Water Resources Research Institute

in cooperation with

Department of Geoscience
New Mexico Institute of Mining and Technology

The research on which this report is based was financed by the State of New Mexico through State appropriations.

Project Numbers: 1345668 and 1423606

DISCLAIMER

The purpose of WRRI technical reports is to provide a timely outlet for research results obtained on projects supported in whole or in part by the institute. Through these reports, we are promoting the free exchange of information and ideas and hope to stimulate thoughtful discussion and action which may lead to resolution of water problems. The WRRI, through peer review of draft reports, attempts to substantiate the accuracy of information contained in its reports, but the views expressed are those of the authors' and do not necessarily reflect those of the WRRI or its reviewers.

ABSTRACT

Natural resource developments in the San Juan Basin of New Mexico have the potential to affect the availability of groundwater supplies. To quantify possible impacts on the basin's Tertiary aquifers, a quasi-three-dimensional numerical model was developed. Due to the limited amount of present groundwater usage, the detailed hydrogeologic information often was not available. The modeling effort utilized a combination of groundwater dating by carbon-14, geostatistics, and geophysical methods to determine appropriate hydrogeological parameters for the groundwater flow model. After calibration, transient analysis of a potential well field site was performed. This simulation indicated that regional water level changes will result from the proposed pumpage.

Groundwater dating was employed to determine the hydraulic conductivity of basin aquifers. Several conceptual models were examined to analyze the effects of dispersion and diffusion on groundwater ages. For the particular aquifers studied, the results indicate that the magnitude of these processes is approximately equivalent to the uncertainty inherent in the measurement of carbon-14 activity. A probabilistic conceptual model was developed to explain the reduction in the effective solute-transport velocity as predicted by the derivation of a stochastic solute transport equation.

The geostatistical technique of kriging was used to estimate hydraulic head values from available data for use in the groundwater flow model. Electric logs were employed to obtain point observations of formation thicknesses. These values were analyzed by multiple regression techniques to obtain appropriate model inputs. Thermal logs were used to estimate the hydraulic conductivity of basin aquitards.

Keywords: aquifer model, carbon radioisotopes*, dispersion, ground water, ground water movement*, stochastic models.

TABLE OF CONTENTS

LIST OF FIGURES

LIST OF TABLES

PROBLEM AND APPROACH

Future economic development in the arid regions of the world will be highly dependent on the availability of groundwater. This situation already exists in the San Juan Basin of New Mexico. The supply of surface water from the San Juan River is fully committed to present and future water projects, forcing potential users to look to groundwater to meet their water needs. However, because shallow groundwater is not available at many sites, attention is naturally directed to deeper, regional aquifers. The hydrology of such aquifers is significantly more difficult to study. Generally, field measurements of hydraulic properties are of limited availability and are sporadically distributed. The high cost of obtaining new information by drilling wells and measuring aquifer parameters often prohibits the use of traditional techniques in an investigation of regional extent where aquifer depth may exceed 500 meters.

The approach followed in this study is to utilize existing information and to develop new hydrologic data by using carbon-14 dating as an indicator of groundwater movement. In the San Juan Basin, several types of useful information are already available. Stone et al. (1983) provide a compendium of reported water level, transmissivity, and storativity values. Without this information, the present investigation would not have been possible. Examination of this material, however, reveals the sparsity and non-uniform spatial distribution of the data. Therefore, a means of estimating parameter values at arbitrary locations from observed values becomes important. Furthermore, knowledge of the validity of the estimation is useful in evaluating the confidence to be placed on hydrologic interpretations drawn from such estimated values. In this study, the geostatical technique known as kriging is employed to address this problem.

The San Juan Basin is rich in mineral resources. The development of these resources has resulted in a wealth of geophysical logging information. Two types used in this investigation are electric and thermal logs. The electric logs are used to ascertain the thicknesses of the aquifer and aquitard units. These logs are also combined with traditional pumping tests to examine the spatial variability of aquifer hydraulic conductivity. Thermal logs are employed to determine the hydraulic conductivity of the basin aquitards. The details of these methods will be discussed in subsequent sections.

During this investigation, several types of isotopic information were collected. These included the stable isotopes of hydrogen and oxygen: deuterium and oxygen-18; the noble gases: argon, krypton, and xenon; and the carbon isotopes: carbon-13 and carbon-14. In this paper, discussion of deuterium, oxygen-18, and the noble gases will be of a very limited extent. These isotopes are more aptly discussed in the larger context of the paleoclimatic history of the San Juan Basin. This study focuses primarily on the hydraulic properties of the basin aquifers and, therefore, provides a foundation for hydrological inferences about basin paleoclimatic history. The analysis presented will make extensive use of the carbon isotopes for the determination of hydraulic conductivity in regional aquifers.

The hydraulic properties deduced by the various methods were employed in a quasi-three-dimensional numerical model and a steady-state calibration of the model, guided by the calculated certainty in estimated parameter values, was performed. A transient simulation of the impacts of a potential well field site located in the eastern part of the study area was also conducted.

INTRODUCTION

Location of Study Area

The study area is located in the San Juan Basin of New Mexico, USA. The basin is situated in the northwestern part of the state (figure 1). The principal area of investigation is bounded to the north by the San Juan River; to the east by the line dividing ranges 6 and 5 west; and to the south and west by the outcrop of the Ojo Alamo Sandstone. Major population centers are Farmington, Bloomfield, and Cuba. Other small settlements include Dulce, Dzith-Na-O-Dith-Hle, Lybrook, Nageezi, and several camps for gas company employees. State Highways 44, 64, and 537 are the major paved roads. Access to most areas is excellent due to numerous oil and gas company roads.

Climate

A semiarid, continental climate is characteristically found throughout the area. Precipitation is strongly influenced by elevation. As reported by Gabin and Lesperance (1977), mean annual precipitation ranges from 20.6 cm at Farmington (1644 m) to 32.3 cm at Gobernador (2195 m). The town of Cuba (2147 m) to the southeast of the study area receives a mean annual precipitation of 34.9 cm. To the south, Chaco Canyon (1882 m) receives an average of 21.9 cm of precipitation annually. Generally greater than 50 percent of the total yearly precipitation falls during the summer months (July through September). This moisture arises from the circulation of air from the Gulf of Mexico. Strong surface heating of this moist air combined with orographic lifting produces the often intense thunderstorms common during the summer. Winter precipitation usually occurs in the form of snowfall. Amounts in excess of 15 cm are common at higher elevations in the study area. Unlike summer precipitation, winter moisture arises from frontal activity associated with the eastward movement of Pacific Ocean storms. During the

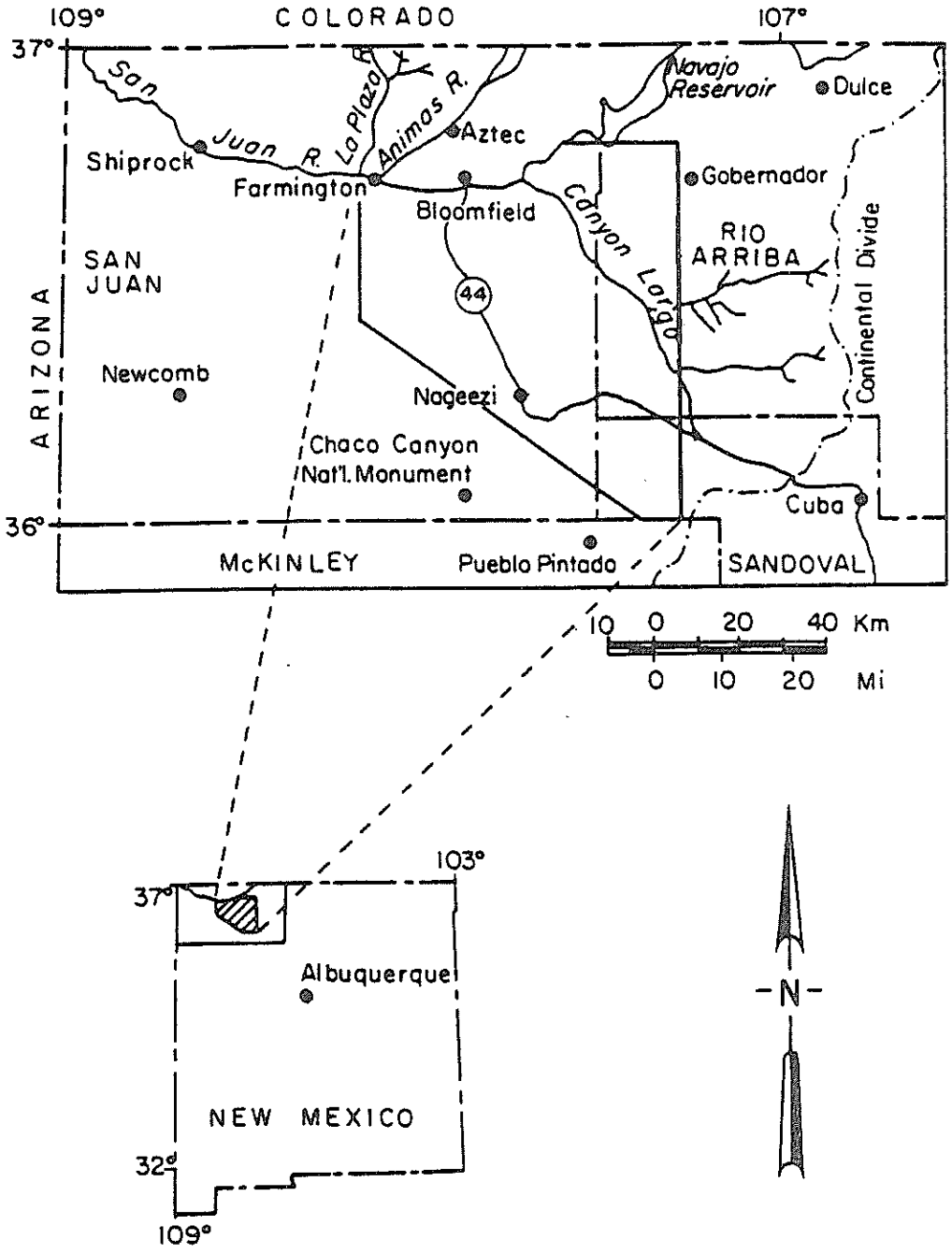

Figure 1. Location Map of the Study Area.

months of December through March, precipitation exceeds potential evapotranspiration (Gabin 1977). During this interval, the majority of basin-wide groundwater recharge presumably occurs.

Mean annual temperatures also reveal a significant elevation correlation. They range from 10.6°C at Farmington to 8.6°C at Lybrook (2179 m). Orographic features can exert an influence on temperatures. Although lower than Lybrook, Otero Store, (2012 m) located in a slight topographic depression, has a mean annual temperature of only 7.7°C. In general, however, this effect is not the dominant factor influencing temperatures in the basin. Differences between summer and winter temperatures are marked. Lower winter temperatures provide the opportunity for the relatively scant precipitation to be more effective in terms of groundwater recharge.

Vegetation

Vegetational associations are largely controlled by the amount and effectiveness of precipitation. The more drought tolerant communities are found at the lower altitudes. These communities are largely grasses and various herbaceous and woody plants. Common among these are snakeweed, four-wing saltbrush, and sagebrush. Although factors other than precipitation affect the species present, the upper limit of precipitation of the lowest vegetational zone is approximately 24 cm of mean annual precipitation. This vegetation zone is found mostly in the western and southern parts of the study area.

A second zone characterized by mean annual precipitation ranging from 25 to 40 cm is the pinyon-juniper woodland. Many of the species found in the lower zone are still present with the major difference being the increasing amount of the coniferous species. The ratio of pinyon to juniper typically increases with increasing precipitation. In the San Juan Basin, this association is found in the eastern portion of the principal study area. Most of the zone is located to the north and east of Highway 44.

A third vegetative community is found only in scattered and isolated microclimates in the higher parts of the area studied. This community is characterized by the presence of ponderosa pine. This association requires in excess of 40 cm of annual precipitation. Although such large amounts of precipitation do not generally occur within the study area, this vegetational community is present in the high country to the east of the principal investigation area.

Geomorphic Features

The San Juan Basin is a northeasterly trending structural depression bounded to the north by the San Juan Mountains, to the east by the Nacimiento Uplift, to the south by the Zuni Mountains, and to the west by the Defiance Uplift (figure 2). The current investigation is confined to a part of the central basin as defined by Kelley (1950). The western half of this section is a broad, gently sloping plateau locally eroded by several ephermeral streams. Near the outcrop of the Ojo Alamo Sandstone, these drainages flow southward toward the Chaco River. To the north, drainages flow northward toward the San Juan River (figure 3). In the northeastern quadrant, the drainages have formed deeply incised, nearly vertical walled canyons. This erosion has left behind a number of high isolated mesas. The southeastern quadrant, while similar in form to the northeast, is not as markedly rugged.

The elevation of the study area ranges from 1640 m (5380 feet) at the San Juan River near Farmington to over 2200 m (7200 feet) along the eastern margin. Relief, especially in the eastern half, can be quite pronounced due to the characteristic erosional processes.

The San Juan River forms the northern boundary of the area investigated. The river arises in the San Juan Mountains north of the town of Pagosa Springs. This perennial drainage provides the major outlet for both the surface and groundwater of the study area.

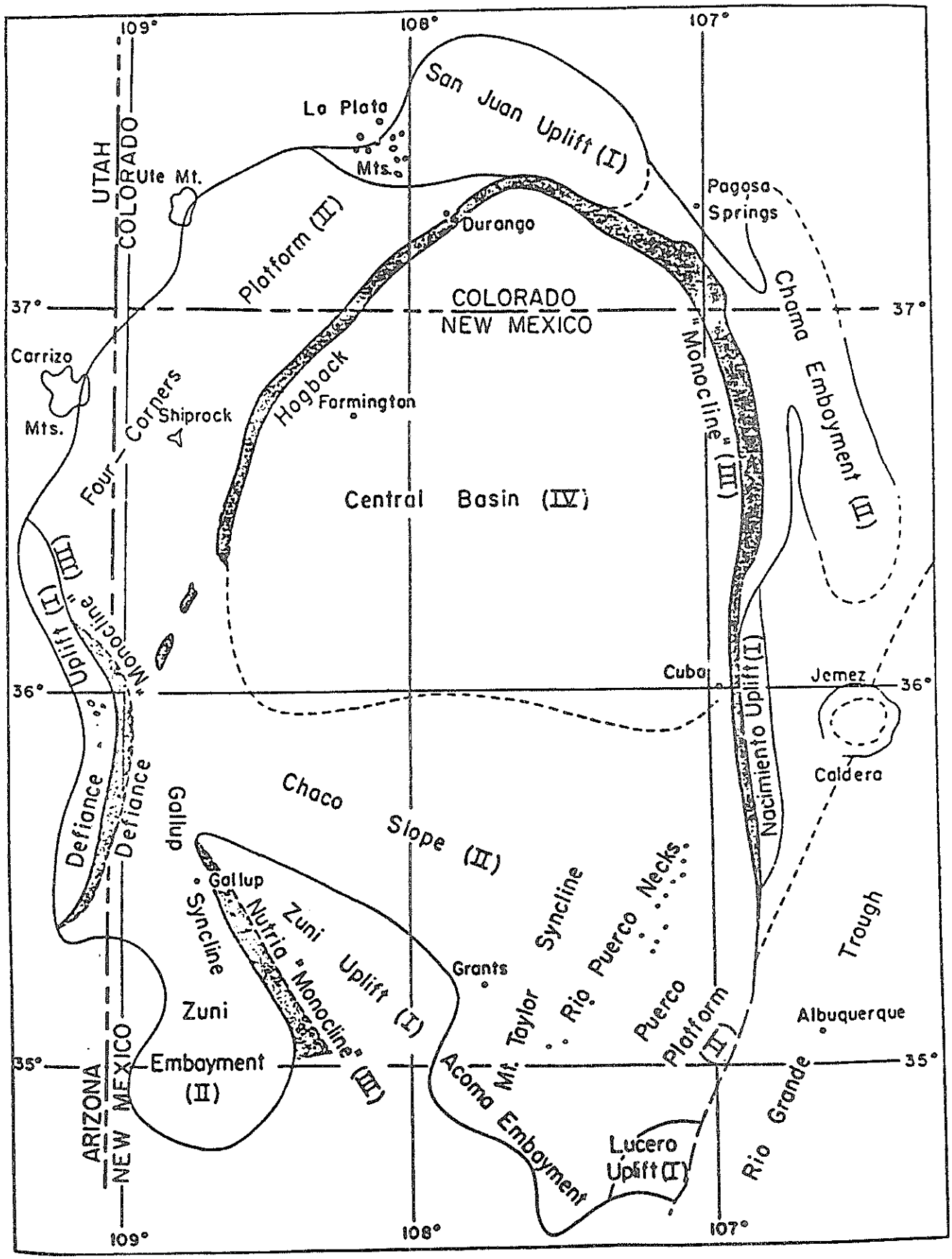

Figure 2. Structural Elements of the San Juan Basin (from Kelley 1950).

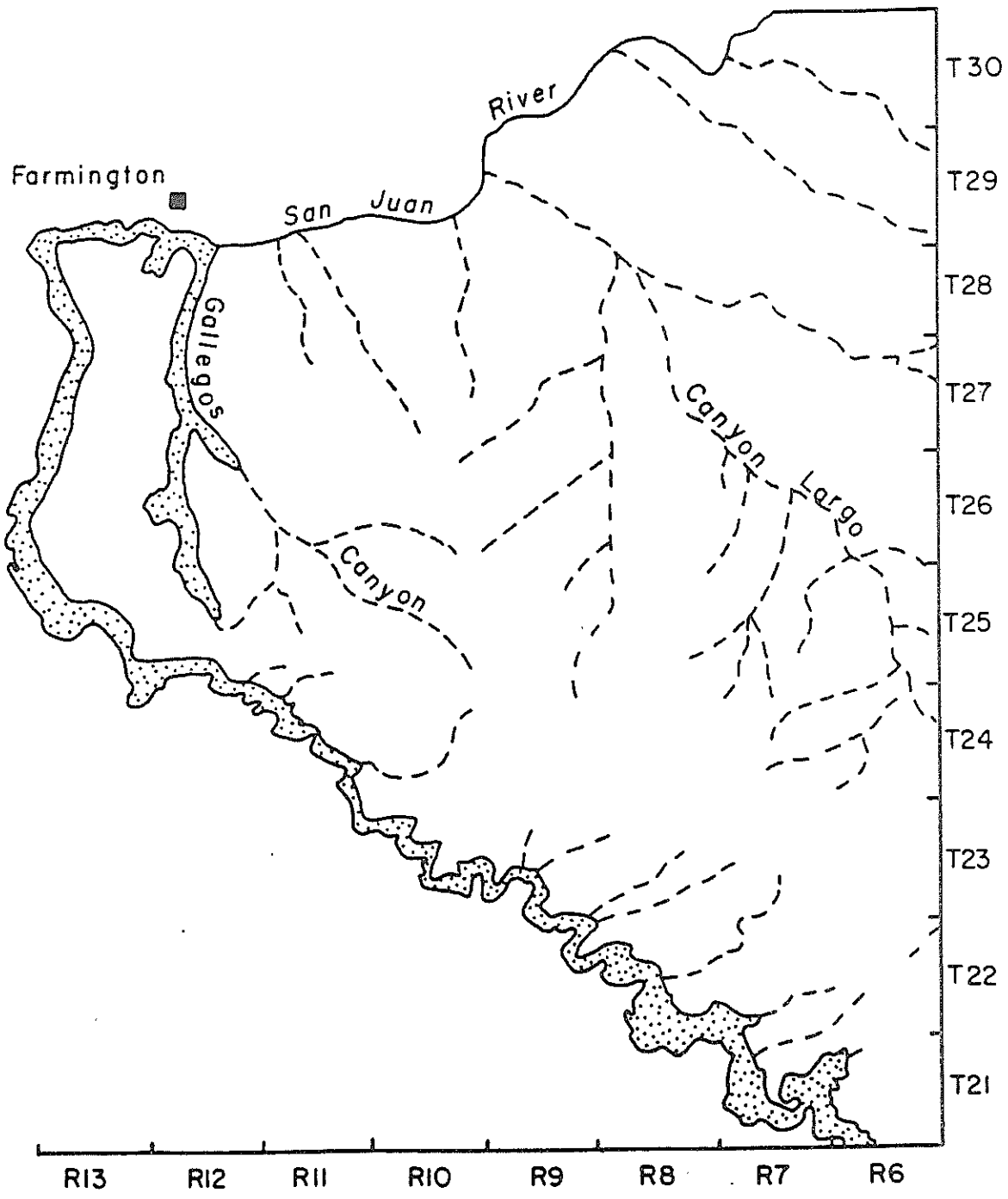

Figure 3. Surface Water Drainages in the Study Area.

Hydrogeology

This discussion of the hydrogeology of the San Juan Basin will focus only on those formations deemed important to a quantitative study of the impacts of groundwater development in the research area. It is especially important to understand the geology of a region prior to any modeling effort. From model conceptualization to final calibration, decisions must be made which will affect the results obtained. Often detailed quantitative information is simply not available. At such times, the hydrologist must rely on a knowledge of the basic hydrogeologic properties of the area in order to produce as reliable a model as possible. Figure 3A is a geologic cross section of the formations studied. The following abridgement of the region's geology will attempt to develop such insights. Most of the information comes from E. H. Baltz's (1967) classic paper.

Pictured Cliffs Sandstone. The Pictured Cliffs Sandstone is the lowest stratigraphic unit considered in this study. It rests conformably on the Lewis Shale and intertongues with it. This unit underlies the entire study area but does not outcrop. It is found at depths ranging from approximately 325 m in the southeast to 1200 m in the northeast. The depth increases in a northeasterly direction paralleling the basin axis. Stone et al. (1983) reported thicknesses ranging from 12 to 52 m.

The Pictured Cliffs is a marine sandstone deposited in littoral and offshore marine environments during the retreat of the Cretaceous Sea. The unit is composed of varied proportions of thin to thick bedded sandstone, siltstone, and shale. Stone et al. (1983) described the sandstone as very fine to fine grained.

Figure 4 is a contour map of the potentiometric surface in the Pictured Cliffs Sandstone. This map was constructed from a contour map in Berry (1959). Since this unit will be used only as a constant head boundary in the modeling effort, its other hydraulic properties are not essential to this study.

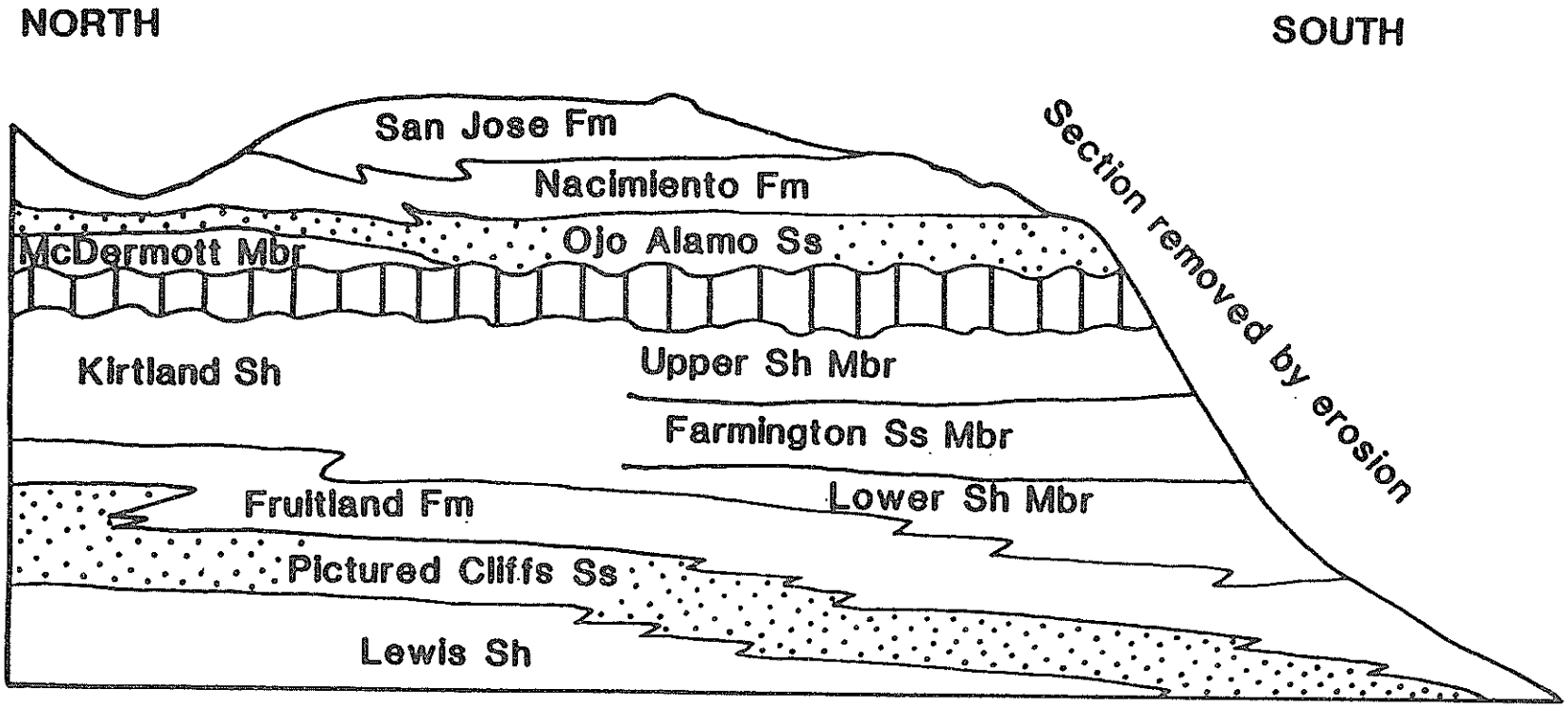

Figure 3A. Geologic Cross Section of Formations.

Fruitland Formation and Kirtland Shale Undivided. The Fruitland Formation and Kirtland Shale underly the entire study area. The thickness of the undivided sequence was estimated from the differences in multiple linear regression surface fittings to observations of the top of the Pictured Cliffs Sandstone and the base of the Ojo Alamo Sandstone. The observations of the elevation of the Pictured Cliffs Sandstone were taken from figure 34 in Stone et al. (1983). The altitude of the base of the Ojo Alamo was determined from electric logs. These values are presented in figure 5. The contours of the calculated thickness are presented in figure 6. In the study area, thickness ranges from less than 100 m in the southeast to nearly 400 m in the northwest. Multiple regression coefficients for the fitted surfaces were in excess of 0.97. The maximum standard deviation in predicted values was less than 20 m.

Lithologically, the units are composed of a complex sequence of thin zones of shale, siltstone, fine to coarse grained sandstone, and coal. The coal is largely confined to the lower Fruitland Formation. The units are generally conformable with each other and the underlying Pictured Cliffs. The sequence represents the final regression of the Cretaceous Sea to the east. Fossils of marine origin in the lower parts of the Fruitland are replaced by terrestrial species in the Kirtland Shale. This retreat of the sea corresponds the beginning of the Laramide Orogeny. The increase in the thickness of the units to the northwest is probably related to rising of the San Juan Mountains as a source area for the fluvial deposits.

Little is known of the hydraulic properties of these units. Stone et al. (1983) reported that tests performed by the U.S. Geological Survey found values of transmissivity on the order of 1.0×10^{-5} ft ^{2}/S. Using thermal data to be presented later, the transmissivity of the Fruitland/Kirtland aquitard is estimated to be about an order of magnitude lower. The low transmissivity of these sediments generally precludes them from

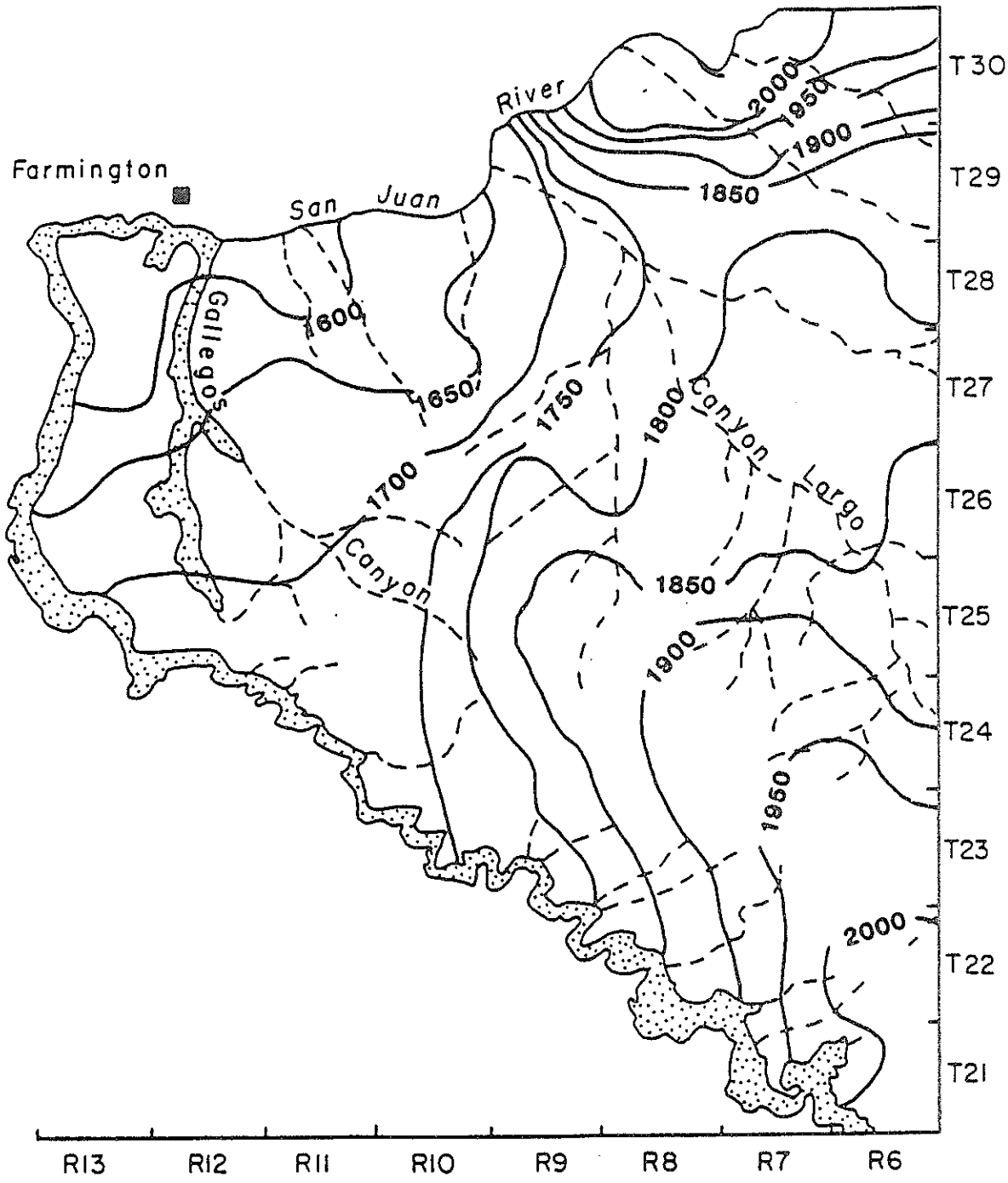

Figure 4. Potentiometric Surface of the Pictured Cliffs Sandstone.

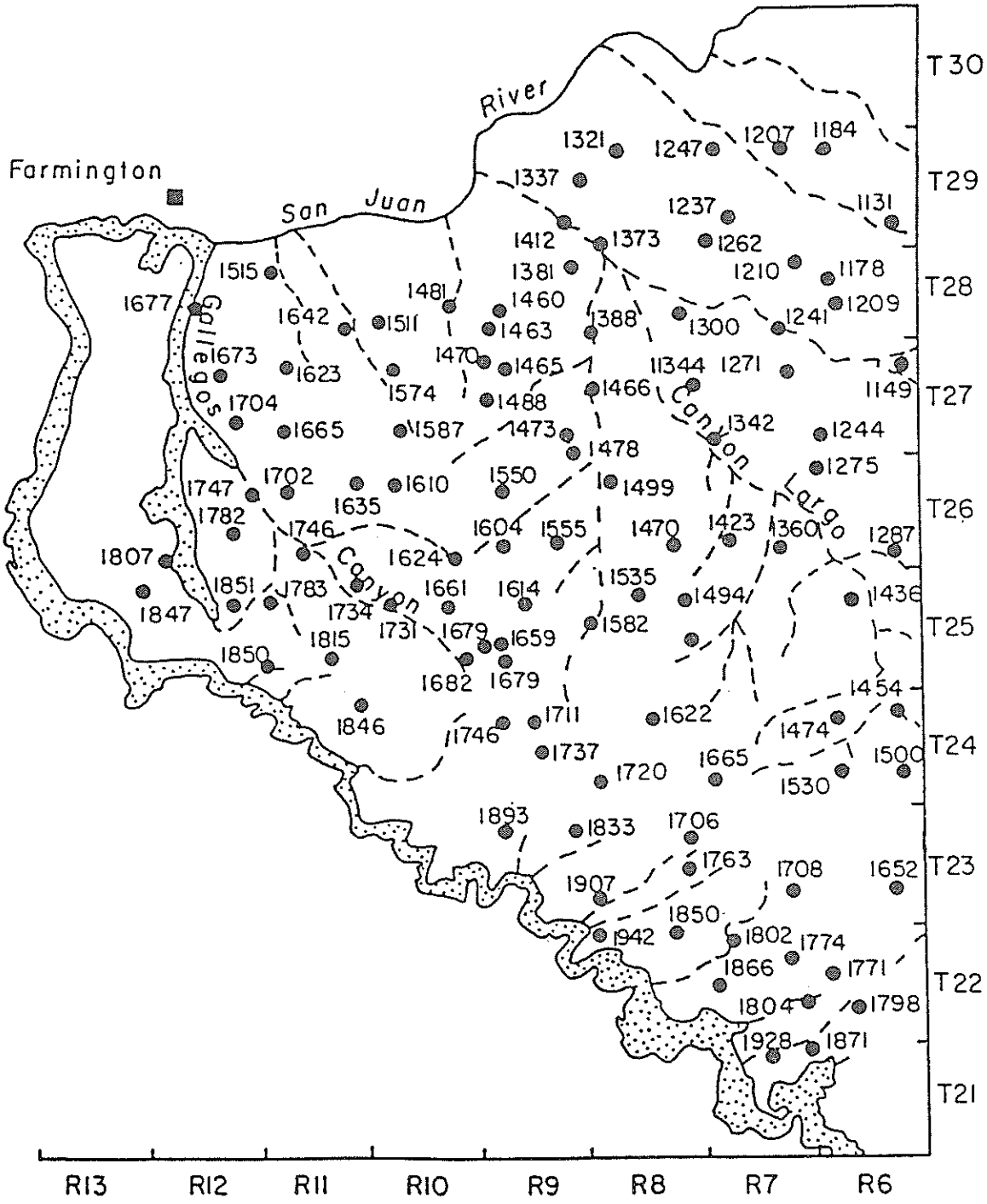

Figure 5. Elevation (m) of the Base of the Ojo Alamo.

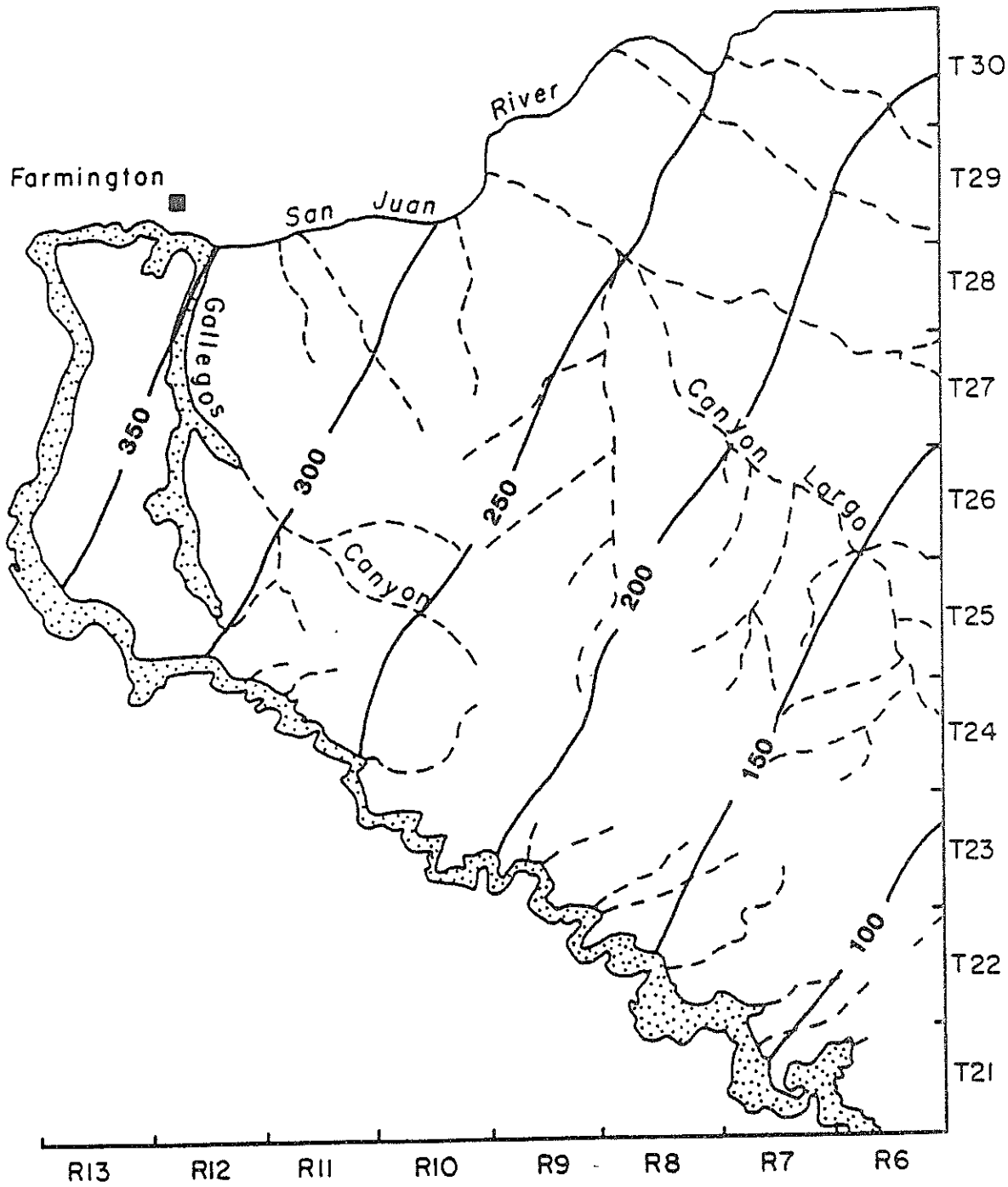

Figure 6. Thickness (m) of the Fruitland Formation and Kirtland Shale Undivided.

being aquifers. In addition, the quality of water yielded from wells tapping them is usually poor.

Ojo Alamo Sandstone. The outcrop of the Ojo Alamo Sandstone forms the western and southern boundaries of the study area. In the subsurface, it is continuously present. Due to an erosional surface at the contact of the Ojo Alamo and the underlying Kirtland Shale, its thickness is somewhat variable. Stone et al. (1983) reported thicknesses ranging from 22 to 95 m. Examination of electric logs revealed an average value of approximately 55 m.

Baltz (1967) described the lithology of the unit as being composed of several beds of medium to very coarse grained sandstone with intervening shales. The basal sandstone layer is often the coarsest and may locally contain sediments of cobble size. This feature is reflected by the large increase in formation resistivity observed in electric logs at the contact of the Ojo Alamo and Kirtland Shale. Baltz (1967) stated the Ojo Alamo was deposited by overlapping stream-channel deposits flowing into the basin from several sides as the present regional structure developed. These source areas were to the north, northeast, and northwest. Powell (1972) statistically analyzed the results of 7,000 measurements of the direction of cross strata at 69 localities along the outcrop of the upper sandstone of the Ojo Alamo. His results showed a marked uniformity of the average depositional directions observed throughout the basin. The average direction was determined to be 138°. Powell compared his results with several possible depositional models. A solitary alluvial fan was rejected because of the constancy of the depositional directions throughout the basin. A coalescing alluvial fan model would result in a higher variability in depositional directions at the local scale. The model Powell deemed the most appropriate was a broad alluvial plain of fluvially deposited sediments with the San Juan Mountains being the source area. Powell also cited a northward thickening of the upper sandstone which is in agreement with such a model.

Brimhall (1973) described the Ojo Alamo as being composed of two types of deposits. The first type are broad floodplain deposits which are laterally continuous for several miles. These deposits are described as being relatively thin and of finer grain size. The second type of deposit is formed by thick coarse channel sediments. Brimhall asserts these deposits are generally of an areal extent of less than one mile. The examination of hundreds of electric logs throughout the study area does not support Brimhall's hypothesis. Locally, there are areas of thinning of the Ojo Alamo but these areas are the rare exception. In general, the uniformity of the Ojo Alamo as expressed in the electric logs is striking. Although the thickness does vary, the Ojo Alamo usually remains about 55 m thick. These observations concur with the sedimentation model proposed by Powell. The data used by Brimhall comes from the very southeastern part of the basin and may reflect localized conditions.

As part of an effort to understand an apparent anomaly in the potentiometric surface of the Ojo Alamo, detailed structural cross sections along the strike and dip of the Ojo Alamo were constructed in Township 24 North, Range 9 West. These figures are contained in Appendix I. Figure 7 is along the dip of the Ojo Alamo. With the exception of profile No. 5, the electric log signal and Ojo Alamo thicknesses are remarkably constant along this 3-mile transect. Profile No. 5 does not lie in direct path between the two adjacent profiles, as may be seen on the location map. It lies about half a mile to the southeast. The structural transect along the strike of the unit is shown on figure 8. The gradual reduction in the magnitude of the resistance signal can be interpreted as the result of an increasing amount of fine grained sediments in the Ojo Alamo maxtrix. The presence of fine textured sediments can be related to a reduction in stream velocity. The occurrence of an area of such sediments centered around Section 17 indicates the likely presence of a lacustrine or swampy environment.

Additional support for this hypothesis can be seen in the potentiometric surface of groundwater in the Ojo Alamo (figure 9). The 1950 m contour bends to the south around the area. Groundwater flow paths inferred from this surface indicate that flow occurs preferentially around rather than through the area. This would be reasonable given the presence of a low permeability region such as the one proposed. A swampy environment such as postulated is not unreasonable given the likely existence of high lands to both the north and south. The rising of the Chaco Slope towards the Zuni Mountains could have produced a reduction in the topographic gradient of the alluvial plain thereby causing lower stream velocities and the deposition of fine grained sediments. Brimhall's report of similar thinning in Ojo Alamo to the southeast of the study area would be concordant with such a depositional model. It must be emphasized that these areas are not typical of the Ojo Alamo.

Only limited data are available on the hydraulic properties of the Ojo Alamo Sandstone. Figure 9 shows contours of the potentiometric surface. This figure was developed by the statistical estimation technique of kriging. Its development is discussed in the methods section. Brimhall (1973) summarized aquifer pumping test for six wells tapping the Ojo Alamo. Transmissivities ranged from 6×10^{-5} m^2/S to 2×10^{-4} m^2/S. Anderholm (1979) measured a value of 9.8×10^{-5} m^2/S in the Ojo Alamo southwest of Cuba. Lyford (1979) and Stone (1979) indicated representative values to be less than 1.2×10^{-4} m^2/S. Storage coefficients reportedly ranged from 2×10^{-4} to 6.7×10^{-3}. Yields from wells tapping the formation generally range from 191 to 981 m^3/day (35 to 180 gpm). Water quality within the study area is generally fairly good. During the course of this study, electrical conductivities ranging from 260 to 1500 usiemens/cm were measured. The sulfate concentration of these waters ranged from 48 to 660 mg/l. These data are presented in table 1.

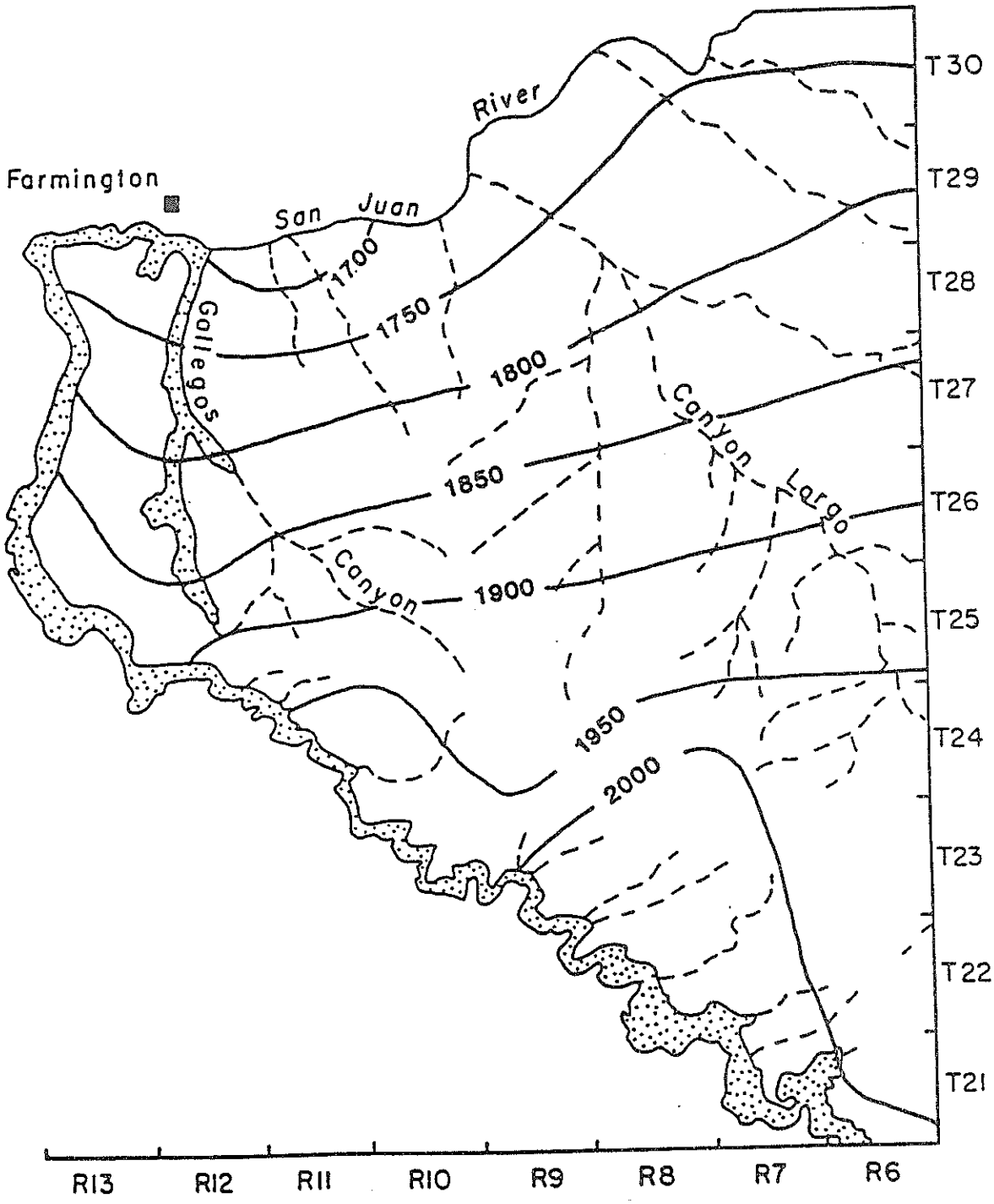

Figure 9. Contours of Hydraulic Head (m) in the Ojo Alamo Sandstone.

Nacimiento Formation. The Nacimiento Formation is present above the Ojo Alamo Sandstone throughout the area. Like the Ojo Alamo, the Nacimiento thickens northward. Stone et al. (1983) reported the thickness to range from 127 to 680 m.

Baltz (1967) described the lithology of the Nacimiento Formation as interbedded shale and soft to resistant, fine to medium grained sandstone. He noted an increase in the ratio of the thickness of sandstone to shale occurs from the south to the north. Baltz (1967) also reported the sandstones in the middle and upper part of the formation are better sorted and more evenly bedded.

Both the lithology and faunal evidence indicate the Nacimiento to be a terrestrial deposit. Baltz (1967) stated the shaley facies in the south and west seem to have been deposited in a lacustrine environment at the distal edge of a huge apron of orogenic material derived from the high lands to the north and northeast. This depositional model is the same as proposed by this author for the distal parts of the Ojo Alamo. Examination of electric logs in the study area revealed a trend toward increasing sandstone thickness in the northeasterly direction. Along the northeastern boundary, Nacimiento Sandstone zones predominate over the shale zones by large margin.

Brimhall (1973) stated "the Nacimiento Formation is not, in its entirety, an aquifer." He based this statement on a presumed lack of continuity of the Nacimiento Sandstone zones in the subsurface and the lack of outcropping of all the sandstone zones. In outcrop, the Nacimiento characteristically appears to be a shale with little or no sandstone. This is due in part to most of the outcrops being in the more distal shaley parts of the formation and in part to the soft, unconsolidated nature of the Nacimiento Sandstones. Subsurface electric logs tell a different story. These logs reveal the presence of numerous thin sandstone zones that are discontinuous. However, they also reveal several thick sandstone zones that appear to be continuous throughout the study area. Detailed correlation of the

Table 1. Chemical analyses for samples (ion concentrations in mg/1; t indicates trace amount present). Carbonate, bicarbonate, pH, EC and temperature values were determined from field measurements performed by the authors. Chemical analyses for:

SJB-1,2,3,4,5,6,9,13,19-0A from Stone et al. (1983).

SJB-8,10,15,16,17,18-0A analyzed by N.M.B.M.M.R.

SJB-11,12,14-0A provided by El Paso Natural Gas Co.

Sample #	Ca^{++}	Mg^{++}	Na^{+}	HCO_3^-	$CO_3^=$	Cl^-	$SO_4^=$	pH	EC	Temp
SJB-01-0A	1.7	0.0	250	303.78	25.20	7.5	230	9.48	930	24.8
SJB-02-0A	1.0	0.0	180	266.57	42.60	3.6	91	9.62	630	15.8
SJB-03-0A	---	---	---	297.01	0.0	---	---	7.88	1050	14.5
SJB-04-0A	1.0	.6	270	290.36	17.40	6.4	340	8.96	990	16.0
SJB-05-0A	15	4.3	450	234.48	13.68	92	660	8.51	1500	13.5
SJB-06-0A	60	3.5	21	74.48	5.28	5.1	100	8.26	385	11.0
SJB-08-0A	1.6	0.0	260	115.47	26.70	8.5	110	8.68	1000	22.0
SJB-09-0A	11	.9	43	46.91	0.0	9.2	48	7.36	260	10.0
SJB-10-0A	3.9	.02	190	330.38	40.74	3.0	160	9.26	680	14.0
SJB-11-0A	10	t	243	270.72	0.0	8	315	8.47	970	17.5
SJB-12-0A	0.0	0.0	158	323.97	68.28	6	91	9.23	780	16.0
SJB-13-0A	4.0	t	290	270.72	47.76	22	310	9.32	980	18.0
SJB-14-0A	48	8	250	220.21	0.0	14	335	8.18	1000	18.0
SJB-15-0A	21	1.3	170	240.22	0.0	4.4	300	8.33	600	15.0
SJB-16-0A	4.7	.03	200	292.19	55.92	5	154	9.27	680	15.5
SJB-17-0A	4.1	.04	240	342.70	64.86	6	---	9.11	650	--
SJB-18-0A	5.0	.04	320	369.05	72.00	11	---	9.04	820	--
SJB-19-0A	--	---	---	192.58	46.86	7.0	---	9.36	590	--

zones is beyond the scope this investigation but examination of figures 7 and 8 shows as much continuity of the Nacimiento Sandstone zones in the upper part of the log as is seen in the lower Ojo Alamo. Brimhall's criticism that all sandstone zones do not outcrop neglects the fact that recharge of regional aquifers does not occur only at the outcrops. As discussed by Stephens (1983), recharge in dipping multi-layered aquifer systems such as this one is not so simple or restricted.

Figure 10 is a statistically analyzed potentiometric surface map of the Nacimiento Formation. Its development will be discussed more fully in the methods section. Stone et al. (1973) suggested that transmissivities in the Nacimiento Formation may be equal to those encountered in the Ojo Alamo. This seems reasonable given the similarity in depositional environments and source materials for the two formations. In data collected from El Paso Natural Gas Company wells, yields ranging from 1 to 6 m^3/day (16 to 100 gpm) have been reported. Brimhall (1973) concluded that wells tapping the Nacimiento may yield from 35 to 200 gpm. The quality of water in the Nacimiento is somewhat poorer than the Ojo Alamo. The water ranges from less than 1,500 to greater than 4,000 usiemens/cm.

San Jose Formation. The San Jose Formation is exposed along the eastern side of the study area. The formation thickens toward the center of the basin, ranging from 61 to 823 m. Like the underlying Nacimiento, the San Jose is composed of alternating zones of sandstone and shale. Baltz and West (1967) divided the formation into four zones. The basal Cuba Mesa Member is a sandstone with interbedded shale which rests with erosional unconformity on the Nacimiento. The Regina Member is a clay shale and siltstone with interbedded sandstone. The next layer is another dominantly sandstone unit with thin beds of shale called the Llaves Member. Finally an upper dominantly shale zone called the Tapicitos is recognized. These four zones often intertongue, making their stratigraphy exceptionally complex.

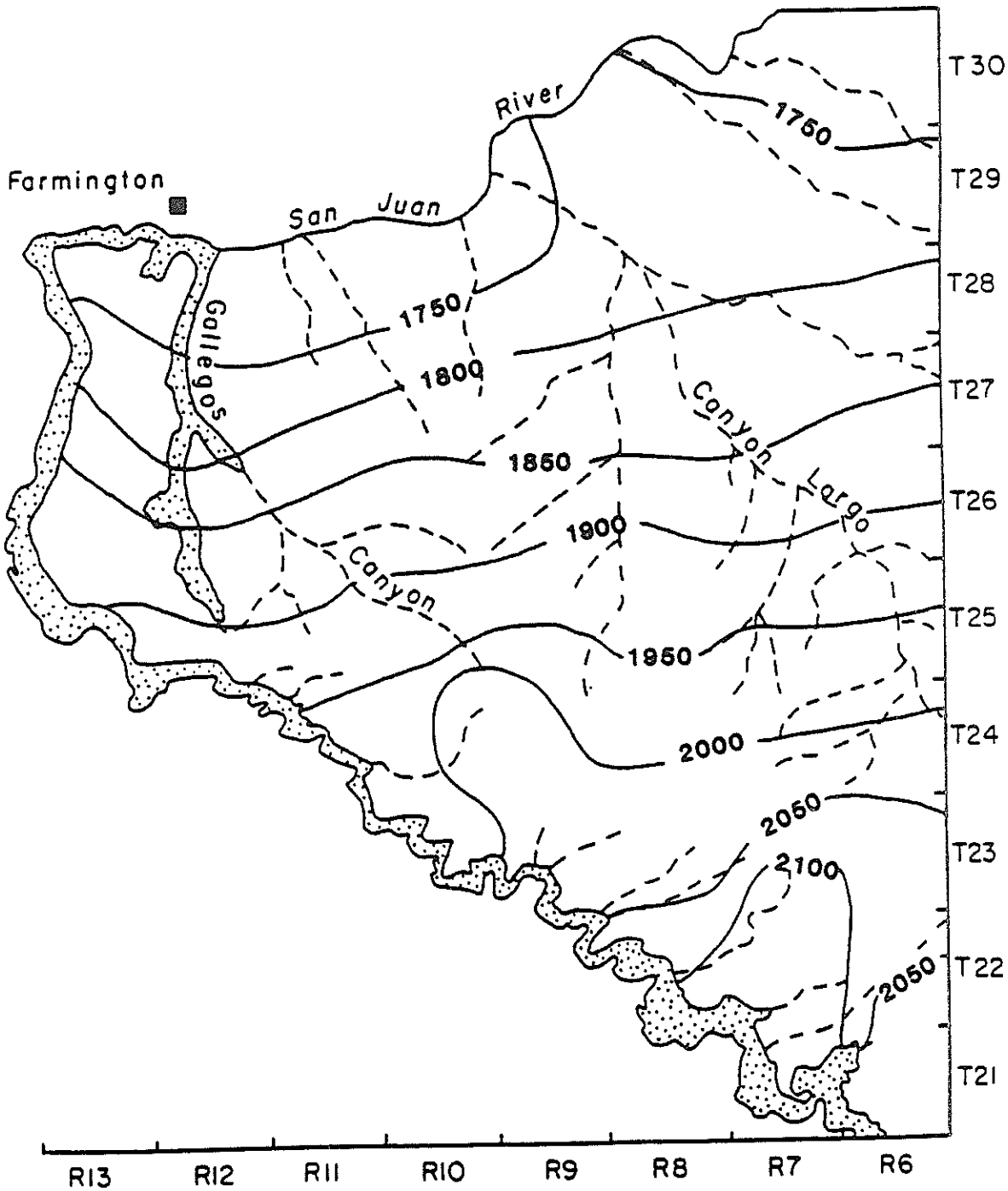

Figure 10. Contours of Hydraulic Head (m) in the Nacimiento Formation.

It had initially been hoped that the San Jose could be included in the numerical flow model. However, the achievement of meaningful results would have required extending the model to regions outside of the intended study area. All data collected from the San Jose Formation are included in this report. The potentiometric surface was estimated by the same statistical methods used for the previous aquifers. The formation is presented in figure 11. In the calibration of the flow model, the San Jose Formation hydraulic head values are used as constant head boundaries.

There is little doubt the San Jose Formation can yield significant quantities of water to wells. Baltz and West (1967) estimated possible yields in excess of 1000 gpm. Stone et al. (1983) reported transmissivities ranging from 4×10^{-5} to 1.3×10^{-4} m^2/S. The quality of the water is often poor and high concentrations of sulfate are reported.

Sample Locations and Numbering Systems

During the two-year course of this study, 35 wells and springs were sampled for various chemical analyses. The locations of these sites are listed by the federal system of land subdivision in table 2. The four parts of the location number refer to the township, range, section, and subsection. Since all townships and ranges in the study area are located north and west of the New Mexico Principle Base and Meridian Lines, the north and west abbreviations have been omitted. Figure 12 also shows the sample locations and field numbers. The last letter(s) of the field symbol refers to the geological unit producing water at the sample site. The Ojo Alamo, Nacimiento, and San Jose Formations are respectively designated by the symbols: OA, N, and CM. Stone et al. (1983) provided tables of detailed well records containing estimates of the producing formation.

Previous Investigations

Several prior investigations of the hydrogeology of the central San Juan Basin are available. Renick (1931), Baltz and

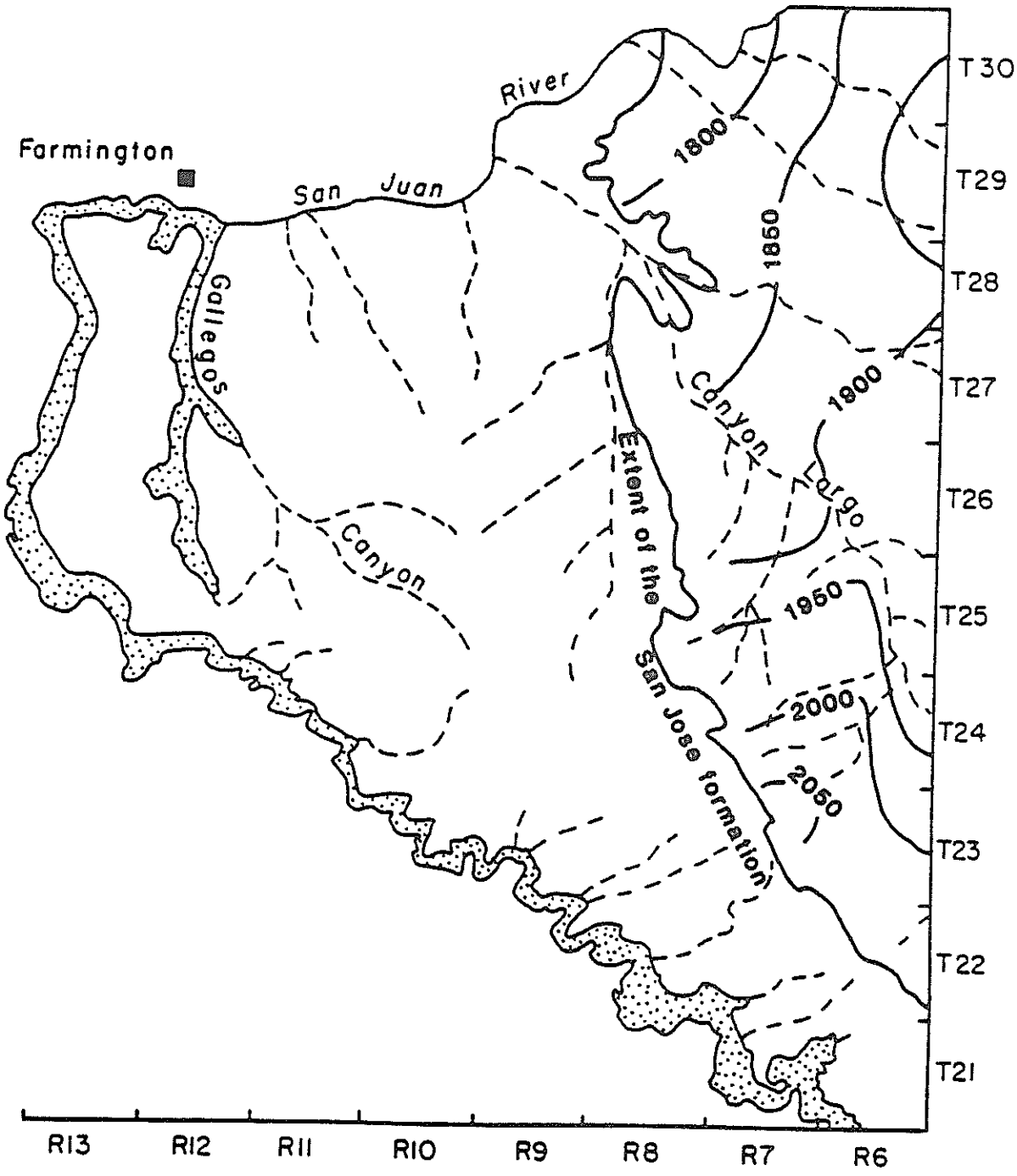

Figure 11. Contours of Hydraulic Head (m) in the San Jose Formation.

Table 2. Sample Number, Name, and Location.

Sample No.	Name	Location
SJB-01-0A	Lybrook	23.07.14.1
SJB-02-0A	B of C Mission	24.10.12.2223
SJB-03-0A	Pete Spring	27.12.35.4244
SJB-04-0A	Powerline WM	23.09.25.3131
SJB-05-0A	Kimbeto WM	24.10.33.4441
SJB-06-0A	Ojo Socorro	21.07.19.4441
SJB-08-0A	Dzilth	25.09.19.1111
SJB-09-0A	Ojo Encino	20.05.22.4422
SJB-10-0A	Johnsons TP	20.02.19.124
SJB-11-0A	Huerfano #2	26.10.25.4141
SJB-12-0A	Huerfano #1	26.10.13.423
SJB-13-0A	Nageezi CH	23.09.01.1141
SJB-14-0A	Chaco Camp #9	27.12.13.142
SJB-15-0A	Hilltop	27.11.26.4111
SJB-16-0A	Kah-Des-Pah	26.08.18.3114
SJB-17-0A	Tsah Tah	24.10.15.114
SJB-18-N	Largo School	26.07.13.344
SJB-19-CM	Pat Montoya	29.07.32.442
SJB-20-N	Milton Lechner	29.10.30.233
SJB-21-N	Tenneco	28.10.26.32
SJB-22-N	Huerfano TP	25.10.13.141
SJB-23-N	19T-342	25.08.31.224
SJB-24-N	19T-349	24.09.01.331
SJB-25-N	29T-298	23.08.27.111
SJB-26-N	Wilfred Pete	25.10.30.441
SJB-27-CM	NW Pipeline #11	29.06.35.111
SJB-28-CM	NW Pipeline #13	29.06.26.444
SJB-29-CM	EPNG Gonzales	25.06.03.414
SJB-30-CM	EPNG 27-5	27.05.03.214
SJB-31-N	EPNG Ridge Rd	29.07.28
SJB-32-CM	EPNG Gould	27.07.15.241
SJB-33-CM	EPNG Largo	26.07.15.412
SJB-34-CM	EPNG Lindrith	24.05.18.421
SJB-35-N	EPNG Ballard #1	26.09.26.442

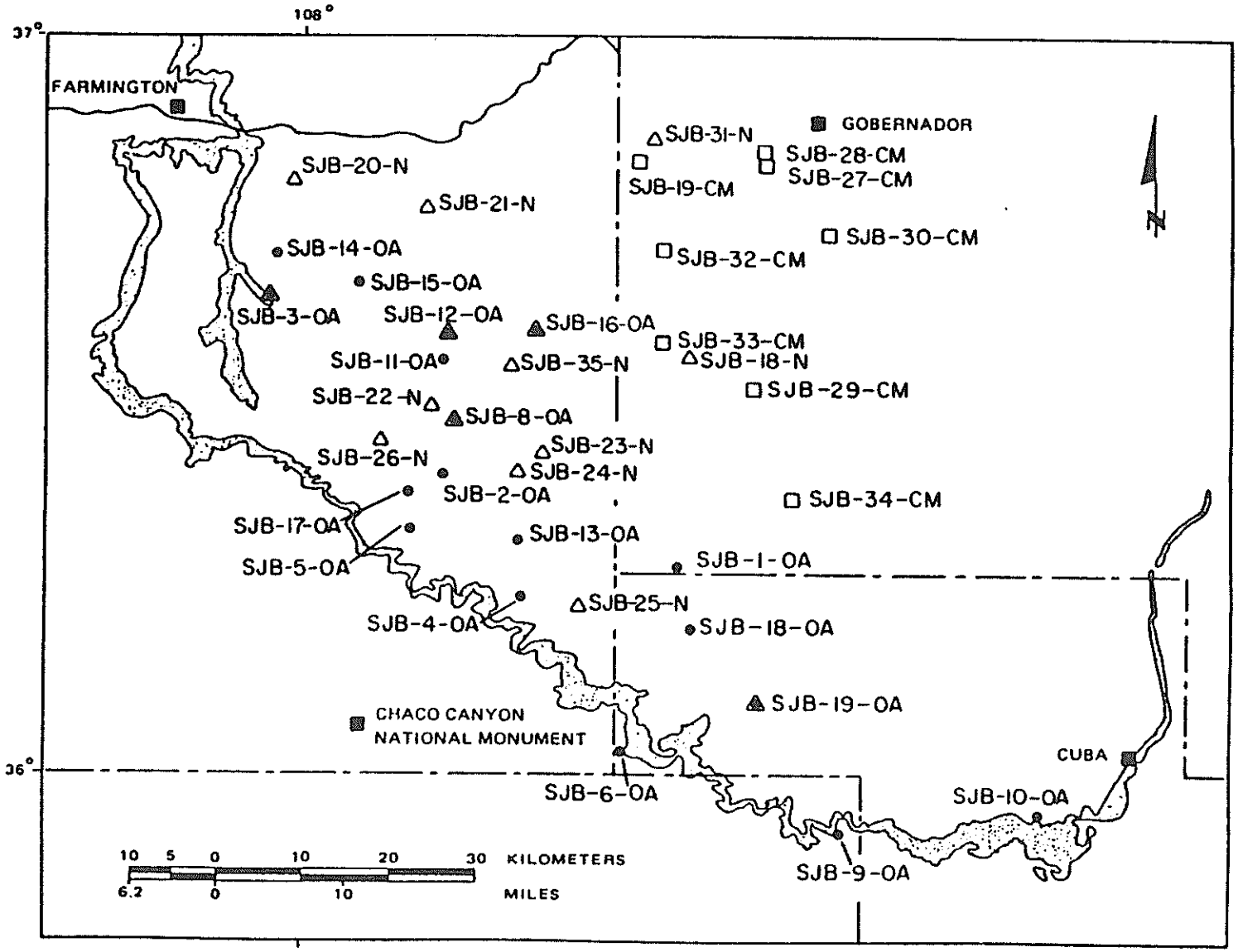

Figure 12. Sample Location Map.

West (1967), Anderholm (1979), and Craigg (1980) studied areas located to the south and east of the present investigation. Rapp (1959) and Brown (1976) studied the hydrogeology of the Farmington and Aztec areas along the northern edge of the study area. Brimhall (1973) discussed the hydrogeology of an area encompassing the present study area. Lyford (1979) also included this study area in a larger one. Stone et al. (1983) compiled the information available from these and other sources into a comprehensive hydrogeologic reference for the entire San Juan Basin.

Groundwater Dating

The simplest radioactive groundwater dating model assumes an ideal tracer traveling through the aquifer in piston-flow fashion. In essence, these assumptions imply the only factor determining the concentration of the tracer at any point in the flow regime is the travel time. To make such an assumption, the effects of dispersion, diffusion, chemical reactions, and mixing with other water must be nonexistent or at least negligible. The appropriateness of such assumptions should always be evaluated on a case by case basis.

The basic equation describing the rate at which a radioactive substance decays is given by

$$\frac{dN}{dt} = -\beta N \qquad (1.1)$$

where N is the number of atoms of the radioactive element, β is a proportionality constant describing the rate at which the substance decays, and t is time. When this equation is integrated subject to the initial condition: $N = N_o$ at $t = 0$, it yields

$$N = N_o\, e^{-\beta t} \qquad (1.2)$$

This equation may be expressed in terms of concentration rather than number of atoms by

$$C = C_o\, e^{-\beta t} \qquad (1.3)$$

where C is the concentration (mass per volume) and C_o is the initial concentration. Often units of activity are used in which case equation 1.2 would be expressed

$$A = A_o\, e^{-\beta t} \qquad (1.4)$$

where A and A_o are respectively the final and initial activities (disintegrations per time per unit total mass).

The solution of equation 1.4 for the elasped time is straightforward.

$$t = -\frac{1}{\beta} \ln \frac{A}{A_o} \qquad (1.5)$$

Subject to the assumptions already discussed, the elasped time is equivalent to the time since recharge occurred. This is termed the groundwater age.

A more comprehensive approach to groundwater dating can be developed by considering the effects of tracer dispersion within the aquifer. The governing equation describing the steady state transport of a radioactive solute through a porous medium is the convection-dispersion equation.

$$D \frac{d^2C}{dX^2} - U \frac{dC}{dX} - \beta C = 0 \qquad (1.6)$$

where D is the coefficient of dispersion (L^2/T) and U is seepage velocity (L/T).

Equation 1.6 is a steady state equation and contains no explicit time variable. To use this equation for groundwater dating requires that the seepage velocity be determined. If all the parameters in equation 1.6, except the velocity, are known, the velocity can be found by matching observed concentrations along the flow path. Of course, this implies the flow path must be known. When this is the case, the groundwater age can be calculated from the ratio of distance to velocity. In practice, the lack of precise data for the coefficient of dispersion requires both velocity and dispersion to be estimated. Unfortunately, such a solution is not unique. In subsequent sections, several estimation techniques are to be combined with stochastic solute transport theory to develop an iterative method for estimating the coefficient of dispersion and the tracer velocity.

The steady state assumption inherent in equation 1.6 also requires a relatively constant input rate for the tracer. For this to be a valid assumption, the atmospheric production rate of carbon-14 should be fairly constant. Studies of the long-term variations in the activity of atmospheric carbon-14 (Suess 1980) have revealed that relatively small changes do occur.

These fluctuations about the mean activity of 100 percent modern carbon (pmc) are not large and thus no correction will be employed in the subsequent analysis.

Sudicky and Frind (1981) pointed out that equation 1.6 neglects the possibility of the loss of the tracer by diffusion into the surrounding aquitards. Neglecting this loss will lead to the determination of an age greater than the real age. The equation describing the convective dispersive transport of a tracer with diffusion into adjacent aquitards is

$$D \frac{d^2C}{dX^2} - U \frac{dC}{dX} - \beta C = \frac{q}{nb} \qquad (1.7)$$

where q is the mass flux (M/L^2T) of the tracer into the aquitard, b is the thickness of the aquifer, and n is porosity of the aquifer. By Fick's first law, the mass flux of the tracer into the aquitards is described by

$$q = - n'D' \left. \frac{dc'}{dZ} \right|_{Z = b} \qquad (1.8)$$

where n' is the porosity of the aquitard, D' is the coefficient of diffusion in the aquitard, and $dc/dZ\big|_{Z = b}$ is the concentration gradient at the aquifer-aquitard interface. The concentration of a diffusing, radioactively decaying tracer in the aquitard is governed by the equation

$$D' \frac{d^2c'}{dZ^2} - \beta c' = 0 \quad b \leq Z \leq \infty \qquad (1.9)$$

Since the aquitards are thick relative to the aquifer and continuity of the tracer concentration must exist at the aquifer-aquitard interface, the boundary conditions for the solution of equation 1.9 are

$$c'(b,X) = C(X)$$

$$c'(\infty ,X) = 0$$

Thus solving equation 1.9 yields

$$c' = c'_o \exp - \{ (\beta/D')^{\frac{1}{2}} (Z - b)\} \qquad (1.10)$$

This expression can be differentiated with respect to Z and evaluated at Z = b to yield

$$\left.\frac{dc'}{dZ}\right|_{Z = b} = -(\beta/D')^{\frac{1}{2}} C$$

Substituting into equation 1.8 and using the result in equation 1.7 yields

$$D \frac{d^2C}{dX^2} - U \frac{dC}{dX} - \left\{\beta + \frac{n'(\beta D')^{\frac{1}{2}}}{nb}\right\} C = 0 \qquad (1.11)$$

The boundary conditions for the solution of this equation are

$$C(0) = C_o$$

$$C(\infty) = 0$$

This is an ordinary differential equation which has the solution:

$$C = C_o \exp\left[\left\{\frac{U}{2D} - \left(\left(\frac{U}{2D}\right)^2 + \frac{\beta}{D} + \frac{n'(\beta D')^{\frac{1}{2}}}{nbD}\right)^{\frac{1}{2}}\right\}\right] X \qquad (1.12)$$

The use of this equation requires several tacit assumptions concerning the properties of the aquifer, aquitard, and tracer. First, the characteristics of the aquifer and aquitards are considered to be representable by a single value over the flow path. Thus, the equation variables are effective values rather than point-specific properties. This is also true of the tracer velocity, and the calculated groundwater age is, therefore, an average age. The assumption has also been made that the tracer has not been affected by chemical reactions or interactions with the aquifer which would either deplete its concentration or retard its transport relative to the bulk solution. If these processes are important, it is possible to account for them. The real problem is obtaining the necessary data to make the corrections.

Initial Carbon-14 Activity

Groundwater dating requires the determination of the initial carbon-14 activity. Due to chemical effects in the

vadose zone prior to recharge, the initial activity of carbon-14 is not necessarily 100 percent modern carbon (pmc). In the pH range encountered in most soils, the bicarbonate anion is the dominate species. It is formed by the reaction of gaseous carbon dioxide, water, and mineral carbonate. If calcite is the primary carbonate mineral, the reaction may be expressed as

$$CO_{2(g)} + H_2O + CaCO_3 \rightleftarrows 2HCO_3^- + 2Ca^{2+}$$

If carbon dioxide with an activity of 100 pmc and "dead" calcite carbon (0 pmc) react as indicated, the activity of the recharge water would be 50 pmc. The presence of unreacted carbonic acid and dissolved carbon dioxide increase the initial activity. Additionally, isotopic fractionations of carbon-14 occur in the vadose zone. These processes further alter the initial activity. Several models have been developed to quantify the extent of these reactions. Most of the correction techniques rely on the use of carbon-13. The basic assumption is that the isotopic behavior of carbon-14 is similar to carbon-13. Since carbon-13 is a stable isotope and its fractionation is known to be one-half that of carbon-14, changes in its composition can be used to correct for non-radioactive changes in the carbon-14 content. The remaining question is which fractionations should be considered. In this study, five models were applied. A brief description of each model follows.

Vogel's Approach. Vogel (1967, 1970) measured the carbon-14 activity of 100 modern groundwater samples. Based on these observations, he proposed a value of 85 $\pm$ 5 pmc. Since these samples represent only a limited area in northwestern Europe, the applicability of these values to other areas and aquifers is questionable.

Tamers' Model. Tamers' (1967, 1975) model accounts for carbon-14 dilution by the addition of dissolved calcite. If the pH is less than 8.3, the fraction of dissolved carbon derived from soil CO_2 may be written

$$F = \frac{mH_2CO_3^* + 0.5\ mHCO_3^-}{mH_2CO_3^* + mHCO_3^-}$$

where m signifies molality and $H_2CO_3^*$ is the sum of the dissolved aqueous carbon dioxide and carbonic acid species. If A_{min} is the activity of the mineral carbon-14, the initial activity can be expressed as

$$A_o = F\ Ag + (1 - F)\ A_{min} \qquad \textbf{(1.13)}$$

where Ag is the activity of the soil gas. When an open system equilibrium at 20°C with additional dissolved carbonate ion of mineral origin (0 pmc) is included, the previous equation may be expressed as a function of pH.

$$A_o = (Ag - A_{min}) \frac{2*10^{-pH} + 10^{-6.3}}{2(10^{-pH} + 10^{6.3} + 10^{(-16.6 + pH)})} + A_{min}$$

Pearson's Model. Ingerson and Pearson (1964) developed a method that accounts for both dilution by dissolved calcite and isotopic fractionation between carbon dioxide gas and bicarbonate, as well as fractionation between bicarbonate and calcite. A simple linear mixing model is used to express the carbon-13 content.

$$\delta_o = F\ \delta_g + (1 - F)\ \delta min \qquad \textbf{(1.14)}$$

where δ_o is the observed carbon-13 content in del notation (per mille relative to the PDB standard); δg and δmin are the carbon-13 content of the soil gas and carbonate mineral, respectively. F is the fraction of carbon-13 of mineral origin. Solving equation 1.14 for F and substituting into equation 1.13 and rearranging yields

$$A_o = \frac{\delta_o - \delta min}{\delta g - \delta min} (Ag - A_{min}) + A_{min}$$

Accounting for the isotopic fractionation effects previously mentioned yields

$$A_o = \frac{\delta_o - (\delta_{min} + E_9)}{(\delta g - E_2) - (\delta_{min} + E_9)} \left[(Ag - .2E_2) - (A_{min} - .2E_9) \right] + (A_{min} - .2E_9)$$

where E_2 and E_9 are the fractionation factors for carbon dioxide to bicarbonate and bicarbonate to $CaCO_3$, respectively. The values used for E_2 and E_9 at 25°C are -8 o/oo and -2 o/oo, respectively.

Mook's Model. Mook (1972, 1976) developed a model based on mineral dissolution and isotopic fractionation between dissolved bicarbonate and carbon dioxide gas in the vadose zone. This model also considers fractionation between dissolved aqueous carbon dioxide and bicarbonate. The carbon-14 activity of the soil water can be expressed as

$$A_{bi} = F\ A_{ba} + (1 - F)\ A_{bm} \qquad (1.15)$$

where A_{bi} is the activity of the soil water bicarbonate, A_{ba} is the activity of the soil water bicarbonate derived from the exchange with soil CO_2, A_{bm} is the activity of the soil water bicarbonate derived from the exchange with mineral carbonate and F is the fraction of soil water bicarbonate derived from exchange with soil CO_2. Assuming the total soil water activity is the same as the initial activity in the saturated zone, the following equation may be written

$$m_a A_{ci} + m_b A_{bi} = m_a A_c + m_b A_b \qquad (1.16)$$

where m_a and m_b are respectively the molalities of the dissolved CO_2 and bicarbonate, A_{ci} is the activity of dissolved CO_2 due to fractionation with soil carbon dioxide, A_c is the activity of dissolved carbon dioxide in the saturated zone after isotopic exchange with dissolved bicarbonate, and A_b is the activity of the dissolved bicarbonate in the saturated zone. Because equilibrium fractionation is being considered, the left-hand side of the last equation can be expressed entirely in terms of the bicarbonate activity. The isotopic fractionation between dissolved CO_2 and bicarbonate may be written as

$$A_c = \frac{A_b + .2\ E_3}{1 + 2\ E_3/10^3}$$

or to a good approximation by

$$A_c = A_b + 0.2\ E_3 \qquad (1.17)$$

Substituting this result into equation 1.16 and solving for A_{bi} yields

$$A_{bi} = \frac{1}{m_b} [(m_a + m_b)\ A_b - m_a A_{ci} + 0.2 m_a E_3] \qquad (1.18)$$

The total activity of the groundwater is given by the expression

$$m_T A_o = m_a A_c + m_b A_b \qquad (1.19)$$

where m_T is total dissolved carbonate concentration and A_o is the initial activity. Substituting equation 1.17 into 1.19 and solving for A_b yields

$$A_b = A_o - 0.2 \frac{m_a}{m_T} E_3$$

When this expression is used in equation 1.18, the result becomes

$$A_{bi} = \frac{1}{m_b} (m_T A_o - m_a A_{ci}) \qquad (1.20)$$

In order to use carbon-13 as a tracer of the reactions involving carbon-14, an expression equivalent to equation 1.15 is written for carbon-13.

$$\delta_{bi} = F\ \delta_{ba} + (1 - F)\ \delta_{bm} \qquad (1.21)$$

Solving equation 1.21 for F and using the result in equation 1.15 yields

$$A_o = \frac{1}{m_T} m_a A_{ci} + m_b (A_{ba} - A_{bm}) \frac{\delta_{bi} - \delta_{bm}}{\delta_{ba} - \delta_{bm}} + m_b A_{bm} \qquad (1.23)$$

The initial bicarbonate carbon-13 content of the soil water, δ_{bi}, is given by an expression corresponding to equation 1.20.

$$\delta_{bi} = \frac{1}{m_b} (m_T\ \delta_o - m_a\ \delta_{ci}) \qquad (1.24)$$

δ_o is the observed carbon-13 content of the water sample. To determine the initial carbon-14 by equation 1.23, the following isotopic fractionation relationships are used:

$$A_{ci} = \frac{Ag - 0.2\ E_8}{1 + 2\ E_{8/10^2}}$$

Which accounts for exchange between dissolved H_2CO_3* and atmospheric CO_2;

$$A_{bm} = \frac{1}{2}\ A_{ci} + \frac{A_m - 0.2\ E_9}{1 + 2\ E_{9/10^2}}$$

Which accounts for exchange between dissolved bicarbonate and calcite; and

$$A_{ba} = \frac{Ag - 0.2E_2}{1 + 2E_{2/10^2}}$$

Which accounts for exchange between dissolved bicarbonate and soil CO_2. Recalling the isotopic fractionation of carbon-13 is one-half that of carbon-14, one may write fractionation equations similar to those above for the carbon-13. Values for the isotopic fractionation factors can be obtained from Friedman and O'Neil (1977).

Fontes' Model. Fontes and Garnier (1979) developed an approach based on dissolution of mineral carbonate and isotopic exchange between: (1) mineral carbonate and soil CO_2; and (2) dissolved carbonate and mineral carbonate. In this model, the possibility of incomplete exchange is taken into consideration. If the molality of dissolved mineral carbonate exchanged with soil CO_2 is denoted as q, a mass balance may be written

$$m_T\ \delta_o = m_g\ \delta_g + (m_{min} - q)\ \delta_{min} + q\ (\delta_g - E_5) \qquad \textbf{(1.25)}$$

where δ_o is the observed carbon-13 content, m_g is the molality of carbon-13 due to solution of soil CO_2, m_{min} is the molality of total dissolved mineral carbonate, δ_{min} is the carbon-13 content of the calcite, and E_5 is the isotopic fractionation factor between soil CO_2 and mineral calcite. The terms m_g and m_{min} can be expressed more explicitly.

$$m_g = m_T - m_{min}$$

$$m_{min} = m_c + 0.5\ m_b$$

where m_c is the molality of the dissolved carbonate species.

The model also considers exchange between dissolved carbonate originating from soil CO_2 and mineral carbonate. Denoting the molal concentration of the dissolved 'active' carbonate by q', a mass balance equation similar to the previous one can be written.

$$m_T \delta_o = (m_g - q')\delta_g + m_{min}\delta_{min} + q'(\delta_{min} + E_5) \qquad \textbf{(1.26)}$$

It can be demonstrated that q and q' are simply the negative of each other. This implies we may determine whether soil CO_2 or mineral carbonates dominate the isotopic exchange processes. If q is a positive quantity, soil CO_2 controls the exchange. If q is negative, mineral carbonate controls the exchange.

An equation analogous to 1.25 can be set up for carbon-14. The solution of this equation leads to the initial activity correction equation.

$$A_o = \left(1 - \frac{m_{min}}{m_T}\right) Ag + \frac{m_{min}}{m_T} A_{min} + (Ag - 0.2\,E_5 - A_{min}) * \frac{\delta_o - \frac{m_{min}}{m_T}\delta_{min} - \left(1 - \frac{m_{min}}{m_T}\right)\delta_g}{\delta_g - E_5 - \delta_{min}} \qquad \textbf{(1.27)}$$

Chemical Reactions

With the exception of Fontes' model, none of the initial activity correction methods accounts for changes in the carbon-14 content due to processes occurring in the aquifer. In Fontes' method, isotopic exchange between dissolved carbonates and mineral calcite is considered, but additional chemical reactions involving carbon-14 are not quantified. In principle, the use of mass balance and chemical speciation programs such as BALANCE, WATEQF and reaction path models like PHREEQE (Plummer et al. 1983) allows for such corrections to be made. The difficulty in using such methods is obtaining the detailed data required to simulate changes in water chemistry along the flow path. Sudicky and Frind (1981) discussed the need to make corrections for changes in carbon-14 content. They concluded that

groundwater dating may be based on carbon-14 activity provided no significant change in total dissolved carbon occurs from the point of recharge to the sampling locality.

Since the carbonate cement in most regional aquifers is very old, its carbon is essentially non-radioactive. If such 'dead' carbon were to dissolve and mix with radioactive carbon-14, it would increase the apparent age of the water, due to the way carbon-14 activity is defined. Modern carbon with an activity of 100 pmc is known to decay at a rate of 13.56 disintegrations per minute per gram of carbon. Any dilution of the 'active' carbon by 'dead' carbon will lower this activity because the disintegrations are measured on a per gram total carbon basis. Given that only dissolution of nonradioactive aquifer carbon-14 occurs, a simple correction is possible. In groundwater dating by the solute transport method, our real interest is in changes in the radioactive tracer concentration. If the total dissolved carbon concentration is known, the carbon-14 concentration can be determined. By using equation 1.1 and the definitions of modern carbon and molality, the correction equation can be expressed

$$m^{14}C = pmc * mTDC * 1.174 \times 10^{-14} \qquad (1.28)$$

where $m^{14}C$ is the molality of carbon-14, pmc is percent modern carbon of the sample, and mTDC is molality of the total dissolved carbon. This equation is a valid conversion equation regardless of whether dissolution or precipitation of carbonates is occurring in the aquifer. Its application as a correction tool in groundwater dating is, however, limited only to instances where radioactive carbon-14 is being diluted by dead aquifer carbon. If carbon is being precipated, other means such as reaction path modeling must be used to correct for the non-decay losses of carbon-14.

Stochastic Solute Transport

In addition to the initial tracer concentration, the use of the solute transport equation for groundwater dating requires a value for the coefficient of dispersion. In this section, a

perturbation method is used to develop a physical understanding and mathematical description of the dispersion process. This approach was initially applied to solute transport by Gelhar et al. (1979) and Gelhar and Gutjahr (1982).

In groundwater dating, the tracer concentration is used to indicate the residence time. Dispersion reduces the concentration of the tracer creating an apparent age greater than the actual one. To account for this discrepancy, a solute transport model can be employed. If the coefficient of dispersion and the initial and final tracer concentrations are known, the seepage velocity is uniquely specified. The actual tracer residence time is simply the distance down the flow path divided by the flow velocity. One of the benefits of the stochastic perturbation approach is that a relationship between fundamental porous medium properties and dispersion can be derived. This relationship ties dispersion to the spatial variability of hydraulic conductivity.

In this study, a one-dimensional steady-state form of the solute transport equation is employed. Several constraints are inherent in the application of such a model. First, since the approach is one-dimensional, the flow path of the solute must be known. In regional aquifers, this streamline is generally curvilinear and, therefore, the independent variable (distance) is not an orthogonal coordinate. Second, for a flow system at steady state, the flow path can be determined from the configuration of the hydraulic head field. From a conceptual viewpoint, steady state flow with velocity perturbations cannot be strictly one-dimensional. As Gelhar and Gutjahr (1982) point out, the existence of seepage velocity variations under conditions of steady flow requires equivalent compensating changes in the cross sectional width of the streamline and/or changes in the aquifer porosity.

The perturbation approach considers an observed system parameter to differ from its mean value by some small random

amount. Using tracer velocity as an example, this can be expressed mathematically by

$$\hat{U} = U + u \qquad (2.1)$$

where $\hat{U}$ is an observed velocity, U is the mean velocity and u is a random perturbation in the velocity. The expected value of the perturbations is considered to be zero.

$$E(u) = 0 \qquad (2.2)$$

where "E" is the expected value operator. The expected value operation on an assemblage of observed velocities produces the mean parameter value.

$$E(\hat{U}) = U \qquad (2.3)$$

In the stochastic approach, a relationship between the variability of parameters is often sought. Using the above properties, a simple and important relationship can be developed. Darcy's law relates the seepage velocity to the hydraulic conductivity and gradient.

$$\hat{U} = \hat{K}J \qquad (2.4)$$

where $\hat{K}$ and J are the hydraulic conductivity and gradient respectively. In this case, the gradient is considered a deterministic rather than random variable. Substituting equation 2.1 into 2.4 yields

$$(U + u) = (K + k)\, J \qquad (2.5)$$

Taking the expected value yields

$$U = KJ \qquad (2.6)$$

This is the mean equation and was derived by employing the mean zero property of the perturbations. If equation 2.6 is subtracted from 2.5, the result is

$$u = kJ \qquad (2.7)$$

This is the mean zero perturbation equation. The relationship between the variance of the velocity and the hydraulic conductivity is obtained by dividing 2.7 by 2.6 and performing the variance operation.

$$\frac{\sigma_u^2}{U^2} = \frac{\sigma_k^2}{K^2} \qquad (2.8)$$

where σu^2 and σk^2 are the velocity and hydraulic conductivity variances. Using the definition of the coefficient of variation (C_i), equation 2.8 can be expressed equivalently as

$$C_u^2 = C_k^2 \tag{2.9}$$

This relationship is important because it equates the variability in groundwater flow velocity to the variability of the hydraulic conductivity.

The mean-concentration solute-transport equation is developed using the same concepts. At the laboratory scale, the steady-state equation for a radioactively decaying solute is written

$$\alpha U \frac{d^2C}{dX^2} - U \frac{dC}{dX} - \beta C = 0 \tag{2.10}$$

where α is the local dispersivity. This dispersivity arises due to flow path tortuosity at a small scale. Typically, experimental values are on the order of centimeters. Dispersivities a thousand times greater have been observed in the field. The dependence of dispersivity on experimental scale has been documented in the literature. By the stochastic approach, an equation analogous to 2.10 will be developed. A benefit of the approach is the insight into the physical causes for the scale dependence of dispersivity.

Assuming that small-scale (i.e., laboratory or "local" scale) dispersion has a negligible effect, equation 2.10 can be expressed

$$U \frac{dC}{dX} + \beta C = 0 \tag{2.11}$$

Proceeding as before with the perturbation approach, substitutions are made

$$(U + u)\left[\frac{dC}{dX} + \frac{dc}{dX}\right] + \beta(C + c) = 0 \tag{2.12}$$

The mean equation is given by

$$U \frac{dC}{dX} + \overline{u \frac{dc}{dX}} + \beta C = 0 \qquad \textbf{(2.13)}$$

The bar indicates the expected value operation has been performed. Subtracting equation 2.13 from 2.12 and neglecting products of perturbations yields the mean zero perturbation equation.

$$U \frac{dc}{dX} + \beta c = - u \frac{dC}{dX} \qquad \textbf{(2.14)}$$

Multiplying equation 2.14 by u and taking the expected value yields an expression for the dispersive flux term.

$$\overline{u \frac{dc}{dX}} = - Cu^2 \frac{dC}{dX} - \overline{\frac{\beta}{U} (uc)} \qquad \textbf{(2.15)}$$

To formulate the mean equation, the last term on the RHS of equation 2.15 must be expressed in terms of the mean concentration. Equation 2.14 is a first order ordinary differential equation and its solution is

$$c(X) = - \frac{1}{U} \int_0^X u(y) \frac{dC}{dy} \exp\left\{ - \frac{\beta}{U} (X - y)\right\} dy \qquad \textbf{(2.16)}$$

Where y is a dummy variable of integration.

The boundary condition used in the solution is

$$c(0) = 0$$

Multiplying by u(X) and taking the expected value yields

$$\overline{u(X)c(X)} = - \frac{\sigma_u^2}{U} \int_0^X R(X - y) \frac{dC}{dy} \exp\left\{ - \frac{\beta}{U} (X - y)\right\} dy \qquad \textbf{(2.17)}$$

where R(X-y) is the covariance of the velocity perturbations. If an exponential covariance function is assumed, equation 2.17 can be expressed

$$\overline{u(X)c(X)} = - \frac{\sigma_u^2}{U} \int_0^X \frac{dC}{dy} \exp\left\{ - (X - y) \frac{U + \lambda\beta}{\lambda U}\right\} dy \qquad \textbf{(2.18)}$$

where λ is the correlation length scale of the velocity field. This is an inherent aquifer property which is related to the distance over which variations in the seepage velocity remain

correlated. A proportional relationship exists between the degree of correlation and the magnitude of the correlation length scale. An approximate solution of equation 2.18 can be developed by expanding the mean concentration gradient term in a Taylor series about the point X. Neglecting terms of order greater than two, this yields

$$\overline{u(X)c(X)} \simeq - \frac{\sigma_u^2}{U}\left[\frac{dC}{dX}\int_0^X \exp\left\{-(X-y)\frac{U+\lambda\beta}{\lambda U}\right\} dy + \frac{d^2C}{dX^2}\int_0^X (y-X)\exp\left\{-(X-y)\frac{U+\lambda\beta}{\lambda U}\right\} dy\right] \quad \textbf{(2.19)}$$

Performing these integrations and substituting the results into equations 2.15 and 2.13 yields

$$A(X) - B(X)\,U\frac{d^2C}{dX^2} - U\left[1 - Cu^2 + D(X)\right]\frac{dC}{dX} - \beta C = 0 \quad \textbf{(2.20)}$$

where

$$A(X) = \frac{\lambda^2\beta Cu^2}{U(1+a)^2}\left[1 - e^{-bX}\right]$$

$$B(X) = \frac{\lambda\beta Cu^2}{U(1+a)}\left[Xe^{-bX}\right]$$

$$D(X) = \frac{\lambda\beta Cu^2}{U(1+a)}\left[1 - e^{-bX}\right]$$

$$a = \frac{\lambda\beta}{U} \quad \text{and} \quad b = \frac{U + \lambda\beta}{\lambda U}$$

The form of equation 2.20 is the same as the laboratory scale solute transport equation. In this case, however, the dispersivity is related to the spatial variability of the seepage velocity field. The assumption of an exponential covariance function gives rise to an asymptotic dispersivity relationship.

If the relationship between the seepage velocity and hydraulic conductivity variability (equation 2.9) is used with the large distance form of equation 2.20, the resultant equation is

$$AU \frac{d^2C}{dX^2} - U^* \frac{dC}{dX} - \beta C = 0 \qquad (2.21)$$

where

$$A = \frac{\lambda^2 \beta C_k^2}{U(1+a)^2}$$

$$U^* = U\left[1 - \frac{C_k^2}{1 + a}\right]$$

The term U* is referred to as the effective velocity. It should be noted that the effective velocity is less than the mean velocity.

To explain the reason for the effective solute transport velocity being less than the mean flow system velocity, a conceptual model analogous to a renewal theory probability model can be employed. Nir and Lewis (1975) discussed such a model. The tracer velocity can be thought of as a random variable. This means a tracer particle can travel through the porous media with any one of an ensemble of possible velocities. The distribution of potential tracer velocities is related to the spatial variability of hydraulic conductivity in the medium. The residence time of a specific tracer particle is its travel time through the system. The particles are considered to travel independently of each other. At any observation point, there exists an ensemble of tracer particles with various residence times. The expected value of the particle residence times is the groundwater age at the observation point.

The reduction of the effective velocity with respect to the mean system velocity is similar to the "inspection paradox" of renewal theory. From a conceptual viewpoint, the phenomena can be explained by the distribution of tracer velocities. If a number of particles are simultaneously introduced into the flow system, the velocity of each particle is determined by the distribution of possible velocities which is a property of the medium. When the tracers are observed at some distance away, particles with velocities greater than the ratio of the observa-

tion point distance to the elapsed time will have already passed the observation point. The expected value of these observed tracer velocities will be less than the mean flow system velocity because the higher velocity particles are not being included in the summation.

With a radioactive tracer, the activity of the tracer particles may be used as the measure of time. In this case, the velocity and radioactive decay probability distributions can be used to explain the reduced effective velocity. Regardless of the exact form of the radioactive decay distribution, all such distributions have common characteristics. At the moment of creation, the probability of decay of a radioactive substance is zero. As time elapses, the probability of decay increases and becomes unity at some infinite time. The specific form of the distribution varies with the type of isotope. In a steady state flow regime, the distribution of velocities at any point in the flow system does not change. Particles traveling with velocities greater than or equal to the ratio of the distance to the elapsed time arrive at the observation point with probabilities of decay reflecting their residence time. Particles with smaller velocities arrive with an increased decay probability.

Assuming the probability of decay to be an independent random variable, the expected value of the tracer decay probability is, therefore, increased with respect to the mean system. The observed activity of the tracer particles can be expressed by

$$A = -K\,[1 - F(t)] \qquad \textbf{(2.22)}$$

where F(t) is the decay distribution function and K is a proportionality constant. The increased probability of decay implies that the "effective activity" is reduced and hence the "effective age" is greater. This further implies a reduced "effective velocity."

A more strictly mathematical approach can be derived. Nir and Lewis (1975) proposed a general probability model of steady state tracer transport. In their development, the average mass

flux transit time was demonstrated to be the ratio of the second to the first statistical moments of the tracer residence time. These can be denoted by

$$E(t) = \frac{m_2}{m_1} \tag{2.23}$$

where m_1 and m_2 are the first and second statistical moments, and E(t) is the average mass flux transit time. Following a derivation provided Dr. Allan Gutjahr (personal communication), the effective velocity can be expressed

$$U^* = \frac{X}{E(t)}$$

or

$$U^* = \frac{X}{m_1}\left[\frac{1}{m_2/m_1^2}\right] \tag{2.24}$$

Thus

$$U^* = U\left[\frac{1}{1 + C_t^2}\right] \tag{2.25}$$

where C_t is the coefficient of variation of the residence time. A binomial expansion of the term in parenthesis leads to the expression

$$U^* \simeq U[\,1 - C_t^2 + \ldots\,] \tag{2.26}$$

Neglecting higher order terms and using the equivalence of the velocity and residence time variations, equation 2.26 becomes

$$U^* \simeq U[\,1 - C_u^2\,] \tag{2.27}$$

When radioactive decay is neglected, this result is equivalent to the effective velocity term derived by the perturbation method.

A practical consequence of these results is the discrepancy that will exist between groundwater ages calculated from Darcy's law and those calculated by the solute transport method. Since Darcy's law gives a mean velocity value, groundwater ages determined from this velocity will be less than the age determined

from solute transport calculation. The magnitude of the difference is related to the spatial variability of the porous medium's hydraulic conductivity. Providing the hydraulic conductivity is relatively homogeneous, the two ages will be almost identical. In any event, the effective velocity and age can be converted to mean values providing the necessary statistical information is available.

Estimating Spatial Variations of Hydraulic Conductivity

Direct calculation of the coefficient of macrodispersion, A, requires knowledge of the statistics of the hydraulic conductivity and its spatial correlation structure. To make statistically valid estimates of the variance and mean of the hydraulic conductivity requires a considerable amount of data. In general, such detailed information is not available. The study area is exceptional, however, because of the large number of oil and gas wells which have been drilled there. Most of these wells have been logged using various geophysical methods. One of the more common types of logs employed in oil field exploration is the electric log. This log essentially measures the resistivity of the formation to an applied electric current. A characteristic of these logs is the low electrical resistivity of the shale layers as compared with sandstone layers. Figure 13 shows two electric logs from water wells located at the Bureau of Indian Affairs Dzilth-Na-o-dith-hle Boarding School (T25 R9W Sec. 19). The deflection of the resistivity curves to the right can be correlated with driller's logs indicating sandstones. The shale zones are indicated by the low resistivity parts of the log which remain close to the depth markers.

These characteristic patterns occur because of the inherent differences in the electrical properties of sandstone and shale. Sandstones composed largely of non-conductive quartz exhibit a high resistivity to the flow of electric current. Shales composed largely of clays, possessing electrically conductive cations, do not resist the flow of electric current. It is commonly observed that increasing percentages of shale embedded in

a sandstone matrix results in progressively lower resistivities. This is reasonable in light of the previous argument and can be verified by examining well logs.

Certain complications can arise. Since the measured resistivity is also related to the associated groundwater resistivity, differences in resistivity could be affected by changes in water chemistry. Such changes can be observed in the San Juan Basin both regionally and locally. Generally, the electrical resistivity of groundwater decreases away from the formation outcrop and with depth at a given location in the basin. These observations are consistent with mineral dissolution occurring in the aquifer.

The oil and gas industry has often employed geophysical logs to calculate intrinsic permeability. In this study, our approach will be to develop a means of calibrating actual aquifer pumping test determinations of transmissivity with electric logs from the pumped well. The resulting calibrated model can then be used to estimate the hydraulic conductivity distribution.

Two fundamental concepts are inherent in the attempt to calibrate an electric log to transmissivity data. The first concept is that increasing amounts of shale in the sandstone matrix result in decreasing electric resistivity. While it is recognized this is not an exclusive interpretation, clearly, there is a sound physical basic for this correlation. The second concept is that of an effective hydraulic conductivity. It can be demonstrated that the effective hydraulic conductivity of a layered medium in which flow is parallel to horizontally continuous, homogeneous layers is the arithmetic mean of the hydraulic conductivities of the individual layers. This may be represented mathematically by

$$K_e = \sum_{i=1}^{N} \frac{b_i K_i}{b_T} \qquad (3.1)$$

where K_e is the effective hydraulic conductivity. K_i and b_i are the hydraulic conductivities and thicknesses of each of the N layers and b_T is the total vertical depth. Since aquifer pumping tests of interbedded sandstone and shales are similar to the type of flow system described above, equation 3.1 may be related to the observed transmissivity by

$$T_{obs} = \sum_{i=1}^{N} b_i K_i \qquad (3.2)$$

where T_{obs} is the observed transmissivity. This equation cannot be solved because of the excess number of unknowns. At this stage, however, an electric log can be employed to aid in the development of a physically based empirical solution. This entails assuming that the ratio of the hydraulic conductivity of a layer to the average hydraulic conductivity of all the layers can be correlated with the ratio of the resistivity of the same layer to the average resistivity of all the layers. The physical reasons for assuming the existence of this relationship have already been discussed. Mathematically, this may be expressed by

$$K_i = R_i \frac{K_{AV}}{R_{AV}} \qquad (3.3)$$

where R_i is the resistivity of a given layer, R_{AV} is the arithmetic mean resistivity of the layers, and K_{AV} is the arithmetic mean hydraulic conductivity.

If a value for the hydraulic conductivity of the aquitards is assumed, substituting equation 3.3 into equation 3.2 yields an equation which can be solved for K_{AV}

$$T_{obs} = \sum_{i=1}^{N} b_i \frac{R_i}{R_{AV}} K_{AV} + K_{SH}\, b_{SH} \qquad (3.4)$$

where K_{SH} and b_{SH} are the hydraulic conductivity and total thickness of the shale layers. Since the hydraulic conductivity of the shales is generally four orders of magnitude less than

the sandstones, they have little affect even when there is a considerable amount of shale. The weighting of the estimated hydraulic conductivity to the average resistivity has an additional benefit. As discussed previously, the chemical characteristics of groundwater vary along the flow path. These variations result in corresponding differences in the average resistivity of the groundwater. Providing the same relative vertical distribution of solutes is maintained, weighting to the average resistivity eliminates the influence of changes in water quality in the direction of flow.

Without transmissivity data, a mathematical form expressing the relationship between resistivity and hydraulic conductivity must be known or assumed. This is because it would be unreasonable to assume K_{AV} remains constant over the entire flow path. In this study, several empirical relationships were developed. One model assumed a linear relationship between resistivity and hydraulic conductivity. A similar model assuming a linear relationship between resistivity and the log of the hydraulic conductivity was also tried. The first model was unsuccessful. It generally overestimated the observed transmissivity. The second relationship was better but required coefficients whose physical meaning was uncertain. The best model developed has essentially the same form as an exponential variogram function. It can be expressed mathematically by

$$K_i = c(1 - e^{-R_i/R_{AV}}) \qquad (3.5)$$

The coefficient c is determined by the constraint that at $R_i = R_{AV}$, $K_i = K_{AV}$ where K_{AV} is determined from the calibration to the aquifer pumping test. Once an appropriate value for c has been determined, equation 3.1 can be used to make estimates of effective hydraulic conductivity at other points along the flow path.

Kriging

Kriging is a technique that allows the estimation of a parameter, such as hydraulic head, at some point in the flow system where its value has not been measured. The estimated parameter value is based on mathematical formulations incorporating the spatial relationship between the location at which the estimate is to be made and the values and locations of all the known observations of the parameter.

Other techniques, such as linear regression and trend surface analysis are available for estimation purposes, but an advantage of kriging is its estimates are unbiased. This means the technique exactly reproduces all known parameter observations. The same is not necessarily true of polynomial or multiple regression estimation procedures. Another advantage of the method is that quantification of the uncertainty in the predicted parameter values can be readily accomplished. A disadvantage of all of these estimation techniques is that they predict average values.

Kriging requires the assumption of a certain degree of statistical uniformity. The particular set of constraints used in this study is called the "intrinsic hypothesis." In mathematical terms, they can be expressed as follows:

$$E\,[V(X)] = m$$

and (4.1)

$$\mathrm{Var}\,[\,V(X+h) - V(X)\,] = 2\gamma(h)$$

where E and Var are the expected value and variance operators; V(X) and V(X+h) are observed parameter values at a separation distance of length h; m is the mean value of the parameter observations; and $\gamma(h)$, the semi-variogram, depends only on h.

The important statistical properties expressed by these equations are the independence of the mean and variance from the spatial location of the observations. The independence of the expected value implies that the mean is constant along any tran-

sect through the observations. The dependence of the variance on only the magnitude of the separation distance is called stationarity of increments. These constraints are similar to strong stationarity wherein the joint probability density function must be invariant under the simultaneous translation of the parameter locations. The conditions stated by equations 3.1 are termed weak second order stationary. Random fields with these properties are called intrinsic random fields of order zero (IRF - 0).

One of the parameters of importance in hydrologic studies is hydraulic head. The physical laws governing groundwater movement dictate that hydraulic head changes in a trending manner. This implies a mean hydraulic-head value which depends on position within the flow domain, a condition which violates the intrinsic hypothesis. One method of overcoming this problem is the utilization of IRF's of order greater than zero. With these functions, stationary of some higher order increment is obtained. An alternate technique is to remove the trend from the observed hydraulic heads. This can be accomplished by fitting a surface to the observed data using multiple regression. Each observation of hydraulic head will generally deviate from the regression fitted surface. This deviation is called the residual. If the hydraulic head field was completely known, these residuals would represent the randomness of hydraulic head at each point in space. In actual fact, the true residuals are being estimated from an incompletely known hydraulic head field. This introduces a degree of error into the determination of the statistical properties of the hydraulic head field.

The advantages of kriging over some of the other estimation techniques stems from the constraints used in its formulation. The unbiasedness of kriging has already been mentioned. Kriging also incorporates the constraint of minimizing the mean squared error, MSE. By definition, the mean squared error is expressed

$$MSE = E\,[V(X_o) - V_o)^2] \qquad (4.2)$$

where $V(X_o)$ and V_o are the true and estimated values of the parameter V at the point X_o. The best estimator is one which has the minimum MSE. For a random field with n known parameter observations, the solution to this problem can be shown to be the conditional expected value of $V(X_o)$. To obtain this expected value, joint probability density functions are needed. This requires more information than is likely to be available. Kriging is a compromise known as the "best linear unbiased estimator."

The parameter estimate, V_o, is made by determining a system of weights, λ_i, one for each known observation such that the linear combination of the products of the kriging weights and the parameter observations forms the parameter estimate.

$$V_o = \sum_{i=1}^{N} \lambda_i \, V(X_i) \tag{4.3}$$

where n is the number of observed parameters. The unbiasedness and mean squared error constraints can be expressed:

$$E\left[\sum_{i=1}^{N} \lambda_i \, V(X_i)\right] = E\left[V(X_o)\right] \tag{4.4}$$

$$MSE = E\left[\left(\sum_{i=1}^{N} \lambda_i \, V(X_i) - V(X_o)\right)\right]^2 = \text{minimum.} \tag{4.5}$$

The unbiasedness and constant mean conditions impose a constraint on the λ_i's such that

$$\sum_{i=1}^{N} \lambda_i = 1 \tag{4.6}$$

This property allows equation 4.5 to be expressed:

$$MSE = E\left[\left\{\sum_{i=1}^{N} \lambda_i \, (V(X_i) - V(X_o))\right\}^2\right]$$

and this expression is equivalent to

$$MSE = \sum_{i=1}^{N} \sum_{j=1}^{N} \lambda_i \lambda_j E[\{ V(X_i) - V(X_o)\} * \{V(X_j) - V(X_o)\}] \quad (4.7)$$

By definition, the semi-variogram is expressed:

$$\gamma (X_i - X_j) = \frac{1}{2} E [(V(X_i) - V(X_j))^2]$$

Adding and subtracting $V(X_o)$ and squaring yields

$$\gamma (X_i - X_j) = \gamma (X_i - X_o) + \gamma (X_j - X_o) - E [\{ V(X_i) - V(X_o)\} * \{ V(X_j) - V(X_o)\}]$$

The last term is the mean square error for two points. Solving for the MSE over the entire domain and simplifying yields:

$$MSE = 2 \sum_{i=1}^{N} \lambda_i \gamma (X_i - X_o) - \sum_{i=1}^{N} \sum_{j=1}^{N} \lambda_i \lambda_j \gamma (X_i - X_j) \quad (4.8)$$

Using the technique of Lagarange multipliers, this equation is minimized to yield the following set of equations:

$$\sum_{j=1}^{N} \lambda_j \gamma (X_i - X_j) + \mu = \gamma (X_i - X_o) \qquad i = 1 \rightarrow n \quad (4.9)$$

$$\sum_{j=1}^{N} \lambda_j = 1$$

From this system of equations, the kriging weights can be determined.

The prediction error at the point of estimation can be found by multiplying 4.9 by λ_i and summing over all the i's. This yields

$$\sum_{i=1}^{N} \sum_{j=1}^{N} \lambda_i \lambda_j \gamma (X_i - X_j) = - u + \sum_{i=1}^{N} \lambda_i \gamma (X_i - X_o)$$

Substituting this result into the equation 4.8 yields

$$MSE = \sum_{i=1}^{N} \lambda_i \gamma (X_i - X_o) + u \qquad (4.10)$$

The MSE is also called the kriging variance. An important property of the kriging variance is its independence from the actual observed parameter values. It depends only on the separation distances between the prediction location and the actual observations.

The semi-variogram is an important function both because it is required to make kriging estimates and because it also expresses the spatial statistical structure of the parameter. A useful relationship between the semi-variogram, variance, and covariance can be derived. By definition of the variance of a sum, equation 4.1 can be expressed:

$$2\gamma(h) = Var(V(X+h)) + Var(V(X)) - 2\,Cov(V(X+h), V(X))$$

where Var and Cov are respectively the variance and covariance.

Since the intrinsic hypothesis for an IRF-0 requires constancy of the variance, the preceding equation is equivalent to:

$$\gamma(h) = \sigma^2 - R(h) \qquad (4.11)$$

where σ^2 is the variance and R(h) is the covariance. By definition, the correlation coefficient r(h) is the ratio of the covariance to the variance. This allows equation 4.11 to be expressed as

$$\gamma(h) = \sigma^2 (1 - r(h)) \qquad (4.12)$$

When no correlation exists, r(h) is zero and the semi-variogram equals the population variance. At an observation (h equals zero), the correlation coefficient is always unity and, therefore, the semi-variogram is zero. Thus, the magnitude of the semi-variogram is inversely proportional to the degree of correlation in the parameter studies and so the semi-variogram increases with separation distance.

To perform kriging, the semi-variogram must be known. This is accomplished by estimating equation 4.1 from

$$\gamma(h) = 1/2n \sum_{i=1}^{N} [\, V(X + h) - V(X)]^{2} \qquad \textbf{(4.13)}$$

The summation is performed over the number of pairs (n) of parameter values [V(X's)] having a separation distance of h. In practice, the separation distance is usually an average distance over some prescribed range of acceptable separation lengths. The semi-variogram is calculated at several separation distances. The results are commonly expressed as a graph of $\gamma(h)$ versus h.

From theoretical considerations, it can be demonstrated that only certain types of functions can be used as variograms. Essentially, the restriction arises from the requirement that the variance of the parameter estimate must be positive or zero. This results in the constraint that the variogram be a conditional positive definite function.

In this study, the variogram function used is called an exponential variogram. Mathematically, it can be expressed

$$\gamma(h) = S\ (1 - e^{h/R}) \qquad \textbf{(4.14)}$$

where h is the separation distance, S is called the "sill", and R is a scaling factor. The value of S should be equivalent to the sample variance, σ^2. The value of R is estimated by matching equation 4.14 to the semi-variogram.

Estimating the Hydraulic Conductivity Correlation Length Scale

To calculate dispersivity by equation 2.21 requires that an estimate of the correlation length scale of hydraulic conductivity be made. Conceptually, the correlation length scale is a measure of the dependence of parameter values on their separation distance. When the parameters are highly dependent on each other, they are highly correlated. The covariance relationship expresses the dependency of random variables. It is the expected value of the product of differences of the random vari-

ables and their respective mean values. Thus, a large positive or negative covariance value implies a high degree of correlation. If the random variables are independent of each other, the covariance will be zero. However, the converse is not necessarily true. That is, zero covariance does not imply independence. Inasmuch as, the value of the covariance depends on the scale of measurement, it is difficult to determine whether a particular covariance value is large. When the covariance is normalized by the variance, the result is an index of dependency called the correlation coefficient. Its value can be demonstrated to vary between -1 and 1. Perfect correlation would result in either a value of -1 or 1.

Figure 13 is a hypothetical covariance relationship. R(h) is the covariance, h

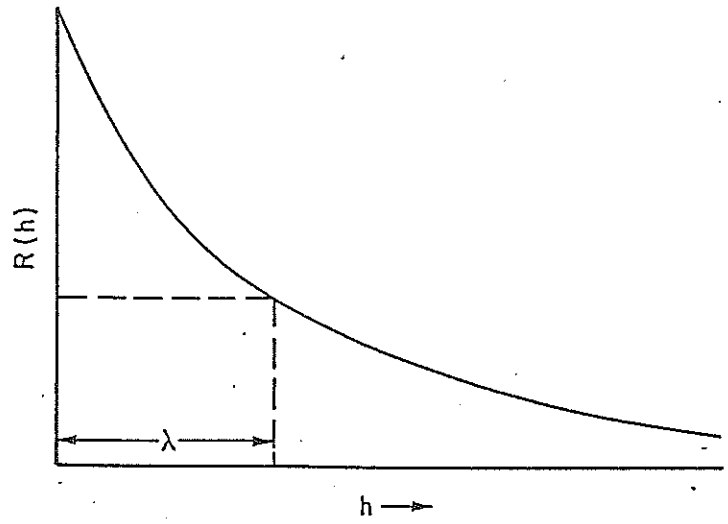

Figure 13. Hypothetical Covariance Function and Correlation Length Scale.

is the separation distance between parameter values, and λ is the correlation length scale. The exact value of the correlation length scale is somewhat arbitrary. In this study, it is taken to be the separation distance at which an e^{-1} reduction in the magnitude of the covariance occurs.

To determine λ requires establishing the functional relationship between the covariance and the separation distance.

This can be accomplished by estimating the semi-variogram and using equation 4.11 to determine R(h).

$$R(h) = \sigma^2 - \gamma(h) \qquad (5.1)$$

It should be noted that the form of the one-dimensional covariance relationship assumed in this study is not the same as that derived by Bakr et al. (1978). Bakr showed that to obtain a finite variance the one-dimensional covariance relationship of the natural logarithm of hydraulic conductivity would become negative after a certain separation distance was exceeded. Covariances determined from equation 5.1 and the assumed form of the semi-variogram cannot become negative. Bakr's three-dimensional covariance relationship is, however, similar in form to the covariance relationship used in this study. Gutjahr et al. (1978) showed similar results when the hydraulic conductivity rather than its natural logarithm was considered.

Estimating the Hydraulic Conductivity of an Aquitard from its Thermal Profile

To simulate groundwater flow with a quasi-three-dimensional groundwater flow model requires values for the vertical hydraulic conductivity of the aquitards. In this study, an estimate of the magnitude of the aquitard hydraulic conductivity was obtained by using thermal logs. The steady state one-dimensional heat flow equation can be written as

$$\frac{\partial^2 T}{\partial Z^2} - C_o P_o V_z / k \frac{\partial T}{\partial Z} = 0 \qquad (6.1)$$

where T is temperature, C_o is the specific heat of the fluid, P_o is the fluid density, V_z is the vertical fluid velocity, and k is thermal conductivity of the solid-fluid complex. Bredehoft and Papadopulos (1965) solved equation 6.1 and obtained

$$(T_Z - t_o)/(T_L - T_o) = f(\beta, Z/L) \qquad (6.2)$$

where T_o is the temperature at $Z = 0$, T_L is the temperature at $Z = L$, and T_Z is the temperature at any point $0 < Z < L$. The function $f(\beta, Z/L)$ is expressed

$$f(\beta, Z/L) = [\exp(\beta Z/L) - 1] / [\exp(\beta) - 1] \qquad (6.3)$$

The parameter β is dimensionless and is expressed by

$$\beta = C_o P_o V_Z L/k \qquad \textbf{(6.4)}$$

Bredehoft and Papoldapulos (1965) suggested a curve matching procedure to determine β. This method requires matching plots of the left-hand side of equation 6.2 versus Z/L to type curves to obtain a value for β. Assuming appropriate values for the parameters in equation 6.4 are known, the groundwater flow rate in the aquitard, V_Z, can be calculated.

Mansure and Reiter (1979) developed a modification to the Bredehoft technique. They noted the total energy flux, E, can be written as the sum of the conductive and convective fluxes.

$$E = -k\frac{dT}{dZ} + C_o P_o V_Z (T - T') \qquad \textbf{(6.5)}$$

where dT/dZ is the thermal gradient and T' is the temperature at which the internal heat energy is taken to be zero. The first term is the conductive heat flow and second term is the convective heat flow. Solving equation 6.5 for the thermal gradient and using the definition of β yields

$$\frac{dT}{dZ} = \frac{\beta}{L}(T - T') - \frac{E}{k} \qquad \textbf{(6.6)}$$

At steady state, the internal energy and flow velocity are constant. Since the value of T' is arbitrary, a plot of dT/dZ versus T has a slope of β/L. If no convective flow occurs, V_Z and consequently β are zero and the graph of dT/dZ versus T will have a horizontal slope. If flow is vertically downward, β/L will be positive and greater than zero. Its magnitude will be proportional to the seepage velocity.

Once β/L has been determined by either of the methods, the groundwater flow velocity is readily calculated.

$$V_Z = \left(\frac{\beta}{L}\right)\frac{kn'}{C_o P_o} \qquad \textbf{(6.7)}$$

If the hydraulic gradient, J, and the porosity of the aquitard (n') are known, the hydraulic conductivity of the aquitard, K', can be calculated by

$$K' = \left(\frac{\beta}{L} \right) \frac{kn'}{C_o P_o J} \qquad (6.8)$$

DISCUSSION OF METHODS AND RESULTS

Field Sampling

The procedure necessary to obtain a groundwater sample for carbon-14 analysis requires that re-equilibration with atmospheric carbon dioxide be minimized. The specific techniques employed in this study are similar to those developed by the Australian Atomic Energy Commission. This procedure is detailed in Appendix II. The groundwater sample is collected in a 50-liter carboy. The pH of the sample is adjusted to at least 10 units by the addition of NaOH. A saturated solution of $BaCl_2$ is added. A floculant, Percol 156, is used to promote the coagulation of the $BaCO_3$ precipitate. The carboys are tightly sealed and the $BaCO_3$ is allowed to settle. The supernatant solution is carefully decanted. The barium carbonate slurry is transferred to 1 liter polethylene containers, tightly sealed, and coated with paraffin prior to shipment to the laboratory for analysis.

All samples collected in this study were analyzed at the Isotope Geochemistry Laboratory of the University of Arizona. The laboratory procedure employed on most of the samples was gas proportional counting. Samples 13, 14, and 15 were analyzed by tandem-accelerator mass spectroscopy. Table 3 presents the results of these laboratory analyses.

Geostatistical Estimation of Aquifer Properties

Hydraulic head values used in the numerical flow model were estimated at each node center by kriging. The theory of this method has already been discussed. Prior to kriging a variogram must be estimated. In this study, the computer program VGRAM, was used to calculate values of the variogram function. This code is essentially equivalent to equation 4.13. In addition, the program has an algorithm that permits the examination of possible directional dependence of variogram values. Figures

Table 3. Carbon-14 Activity and Carbon-13 Enrichment Per Mille.

Sample No.	Name	A (pmc)	$\delta^{13}C$ (PDB)
SJB-01-0A	Lybrook	6.88 ± 0.74	-14.5
SJB-02-0A	B of C Mission	28.66 ± 0.85	-14.1
SJB-03-0A	Pete Spring	76.66 ± 1.44	-8.6
SJB-04-0A	Powerline WM	51.22 ± 1.14	-14.0
SJB-05-0A	Kimbeto WM	5.52 ± 0.85	-14.5
SJB-06-0A	Ojo Socorro	59.34 ± 1.96	-6.7
SJB-08-0A	Dzilth	8.99 ± 0.90	-16.6
SJB-09-0A	Ojo Encino	99.94 ± 2.19	-8.1
SJB-10-0A	Johnsons TP	51.92 ± 1.00	-14.3
SJB-11-0A	Huerfano #2	4.70 ± 0.6	-15.5
SJB-12-0A	Huerfano #1	4.40 ± 1.5	-13.8
SJB-13-0A	Nageezi CH	10.16 ± 0.56	***
SJB-14-0A	Chaco Camp #9	13.30 ± 0.63	***
SJB-15-0A	Hilltop	10.25 ± 0.75	***
SJB-16-0A	Kah-Des-Pah	3.50 ± 0.7	-15.1
SJB-17-0A	Tsah Tah	40.30 ± 0.9	-13.1
SJB-18-N	Largo School	2.2 ± 0.5	-26.0
SJB-19-CM	Pat Montoya	8.8 ± 0.4	-13.8
SJB-21-N	Tenneco	1.73	-15.3
SJB-22-N	Huerfano TP	12.3 ± 0.5	-13.5
SJB-23-N	19T-342	55.0 ± 0.6	-11.4
SJB-24-N	19T-349	51.2 ± 0.6	-13.2
SJB-25-N	29T-298	66.4 ± 0.5	-11.4
SJB-27-CM	NW Pipeline #11	31.4 ± 0.4	-16.8
SJB-28-CM	NW Pipeline #13	2.8	-18.6
SJB-29-CM	EPNG Gonzales	2.0 ± 0.6	-13.2
SJB-30-CM	EPNG 27-5	2.0 ± 0.6	-16.9
SJB-31-N	EPNG Ridge	31.8 ± 0.8	-13.0
SJB-32-CM	EPNG Gould	10.6 ± 1.8	-14.7
SJB-33-CM	EPNG Largo	3.0 ± 0.5	-15.0
SJB-34-CM	EPNG Lindrith	1.1 ± 0.4	-13.9
SJB-35-N	EPNG Ballard #1	9.2 ± 0.4	-14.6

14, 15, and 16 are the data points used to estimate the variograms of the Ojo Alamo, Nacimiento, and San Jose Formation hydraulic heads. Prior to calculating the variogram, a multiple linear regression surface was fit to each of these hydraulic head fields. The variogram analysis was subsequently performed on the detrended residual values. Figures 17, 18, and 19 are variograms of detrended hydraulic heads in the Ojo Alamo, Nacimiento, and San Jose respectively. In each figure, semi-variogram functional values are calculated using several different step sizes. The separation distance value, h, plotted on the figures is the arithmetic mean of all the separation distances included within the specified step size. A problem encountered throughout this study is the lack of a sufficient number of data points. In the case of variogram estimation, this is reflected in the variations of the semi-variogram functional values. The important point to note on the variograms is, however, that in all cases the semi-variogram values decrease at smaller separation distances. As discussed in the section on kriging theory, this reduction implies a spatial correlation in the hydraulic head field. The solid line on the figures is an approximate fit to the data points assuming an exponential variogram function.

The variograms of Ojo Alamo and Nacimiento hydraulic heads are both isotropic variograms. Anisotropic variogram analyses were performed but no directional dependence was noted. The variogram of hydraulic head in the San Jose Formation is an anisotropic variogram. The directional angle is 90° north of east. Inspection of figure 16 reveals that the alignment of the hydraulic head data points is approximately on a north-south transect. There is very little east-west spread in the data. The directional orientation of the hydraulic head data appears to be reflected in the variogram's anisotropy.

The fitted exponential variograms were subsequently used to perform kriging. This kriging was performed using the detrended residuals from the regression analyses as the observed values.

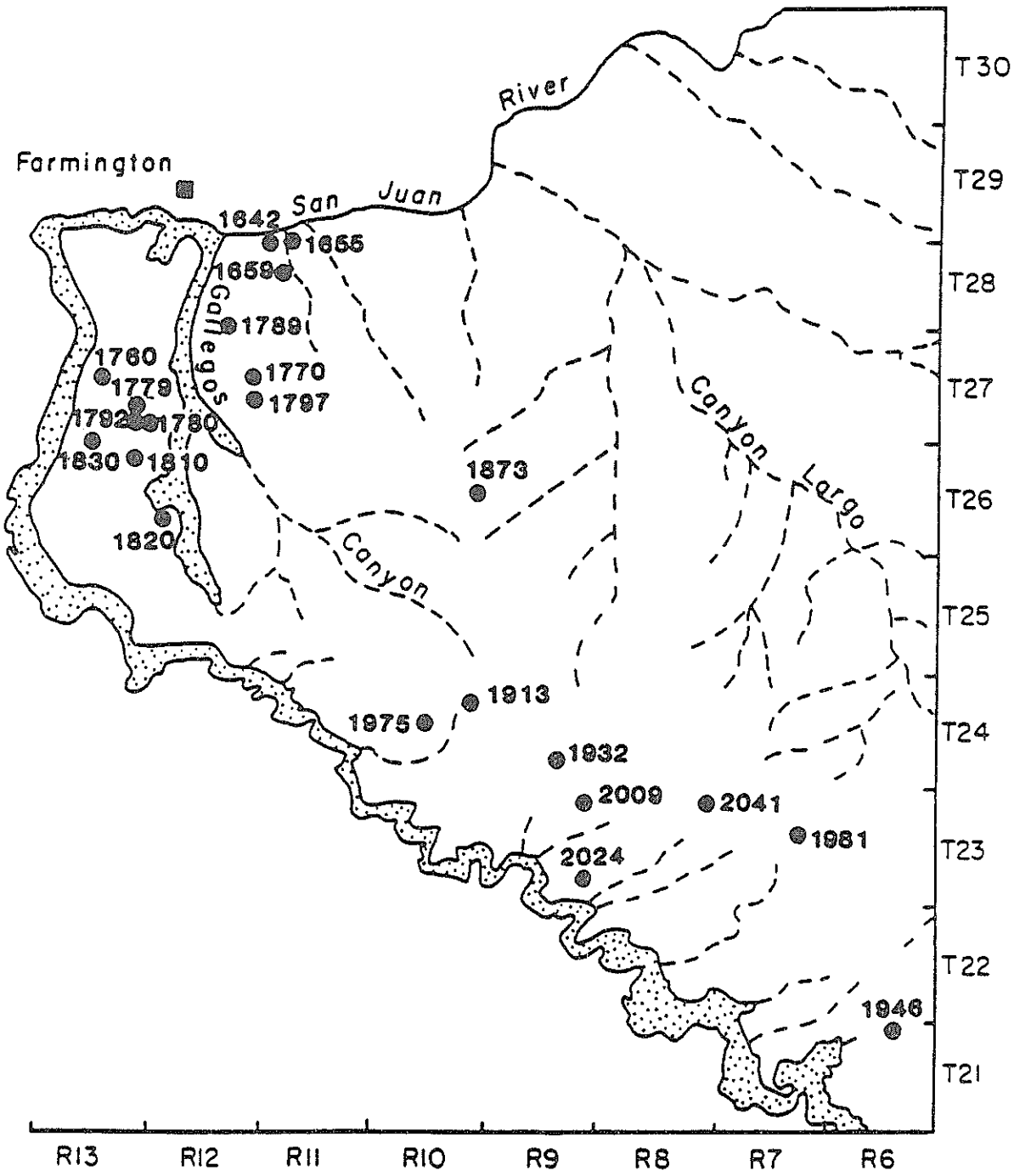

Figure 14. Observations of Hydraulic Head (m) in the Ojo Alamo Sandstone.

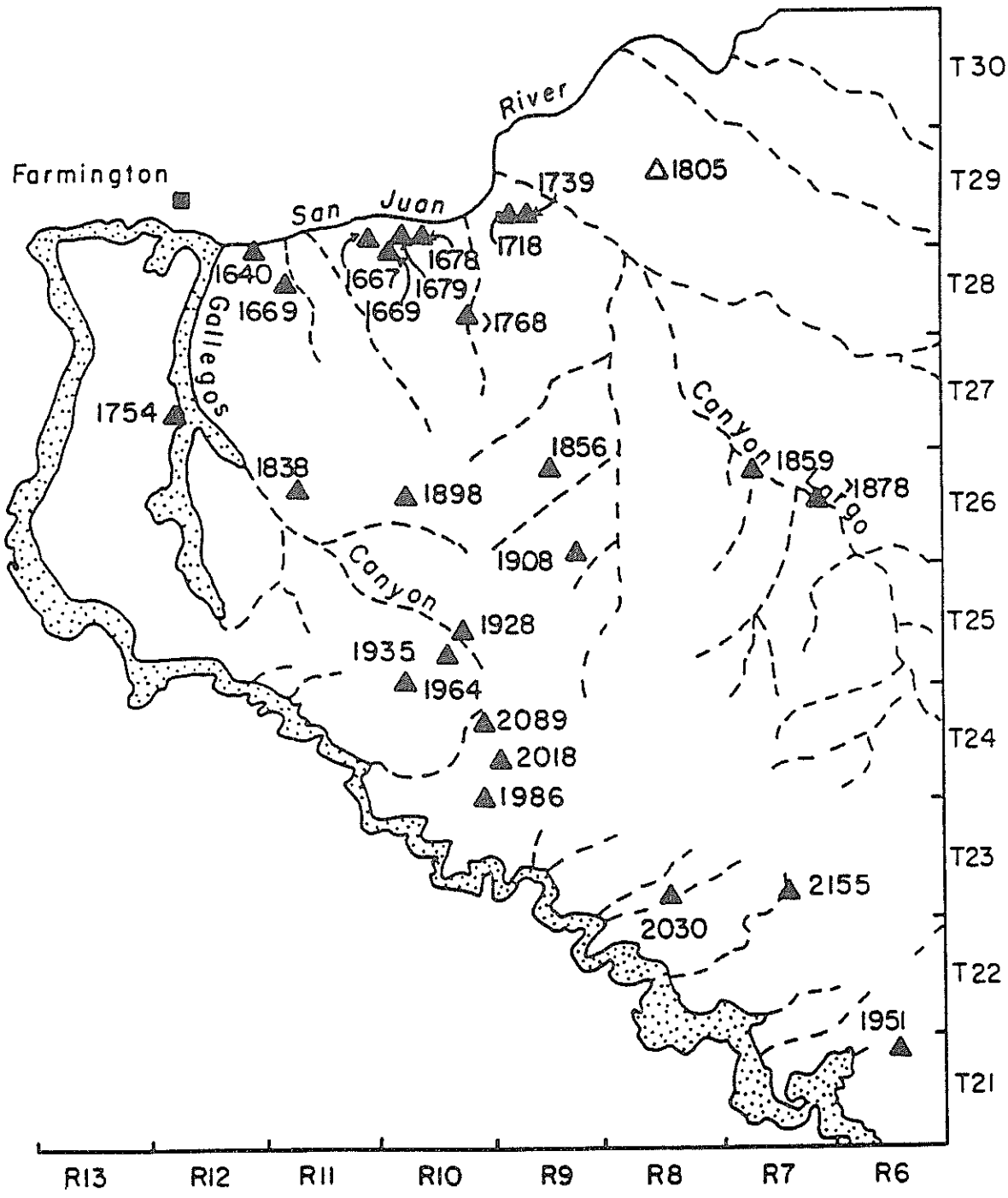

Figure 15. Observations of Hydraulic Head (m) in the Nacimiento Formation.

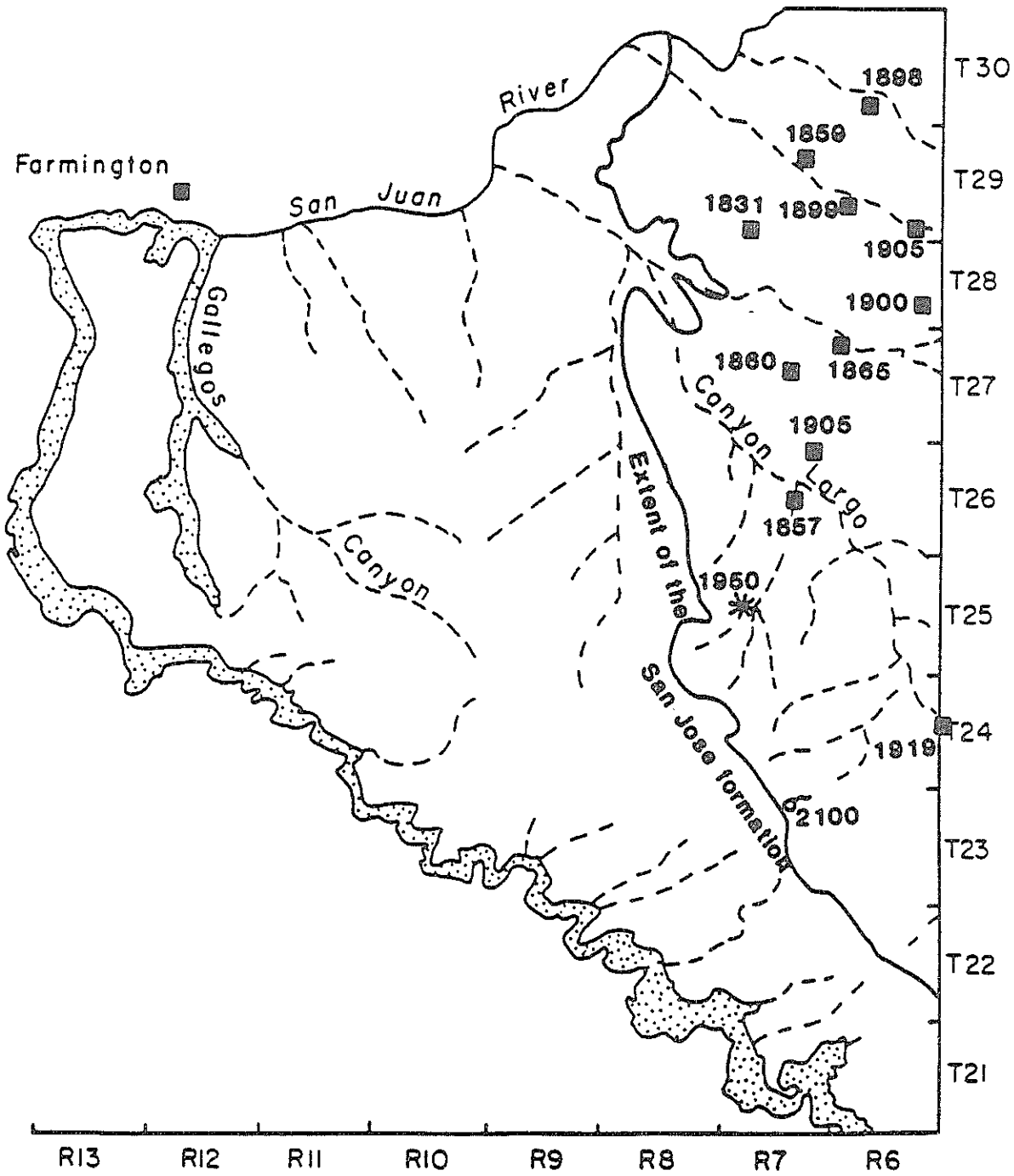

Figure 16. Observations of Hydraulic Head (m) in the San Jose Formation.

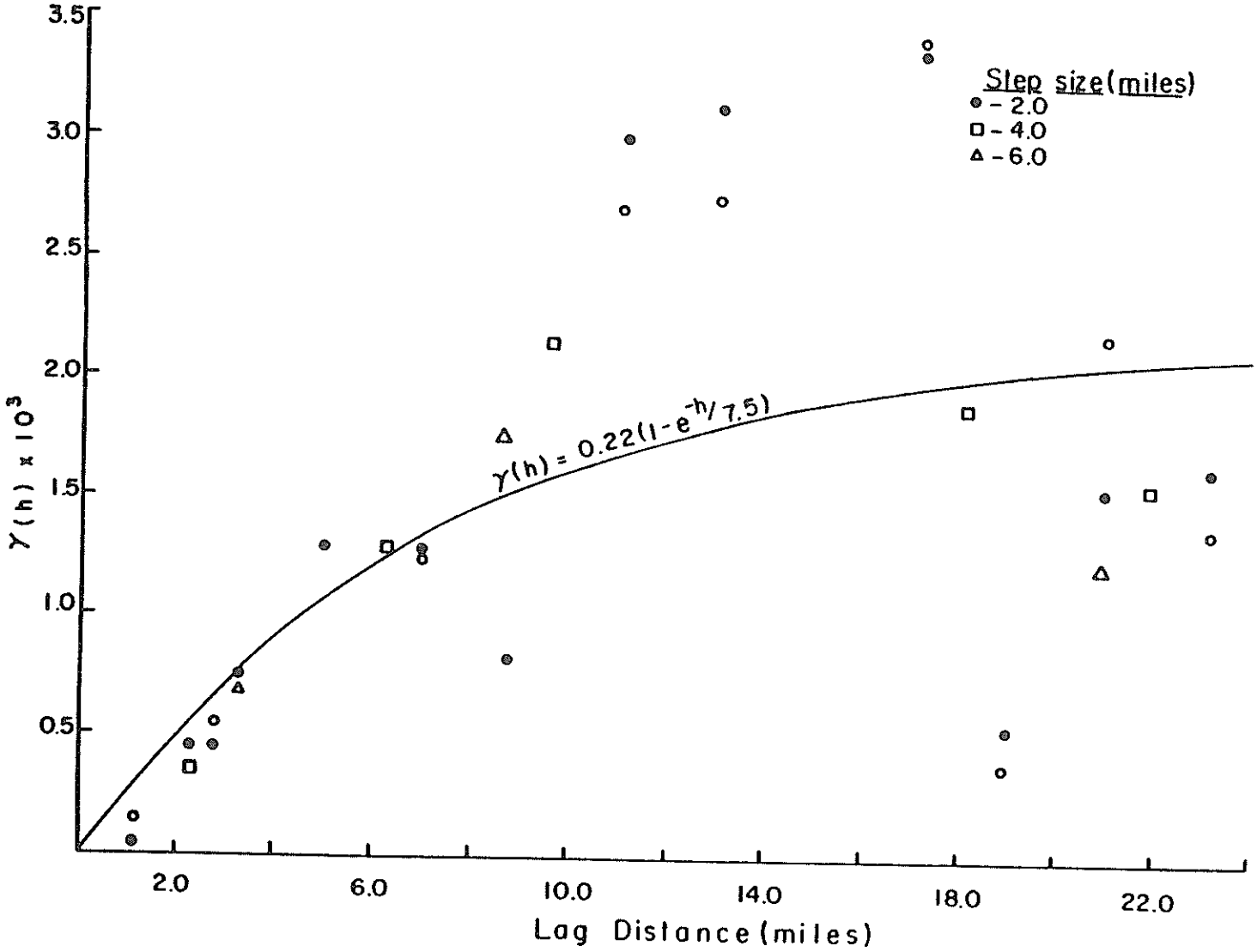

Figure 17. Variogram of Hydraulic Head in the Ojo Alamo Sandstone.

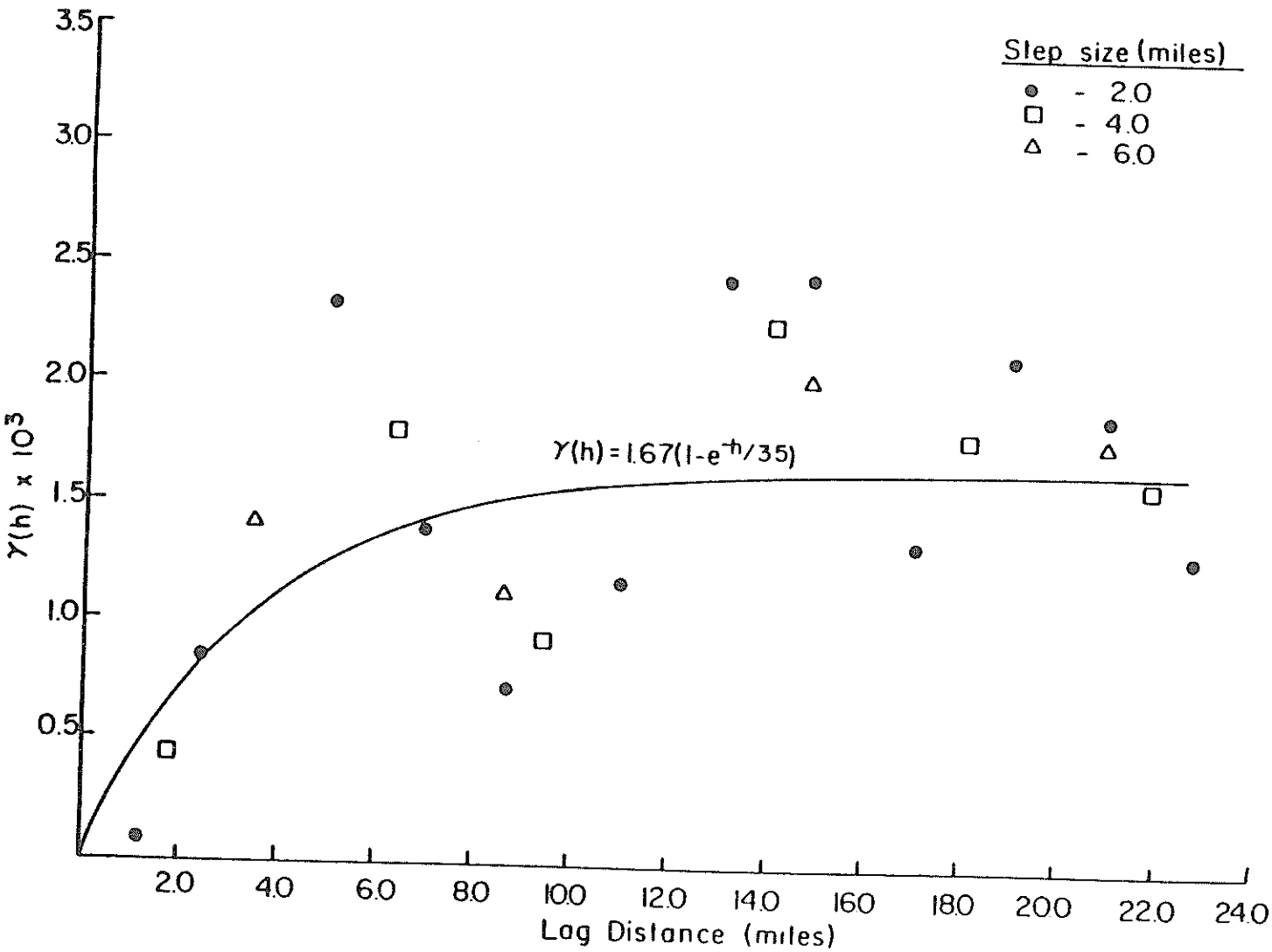

Figure 18. Variogram of Hydraulic Head in the Nacimiento Formation.

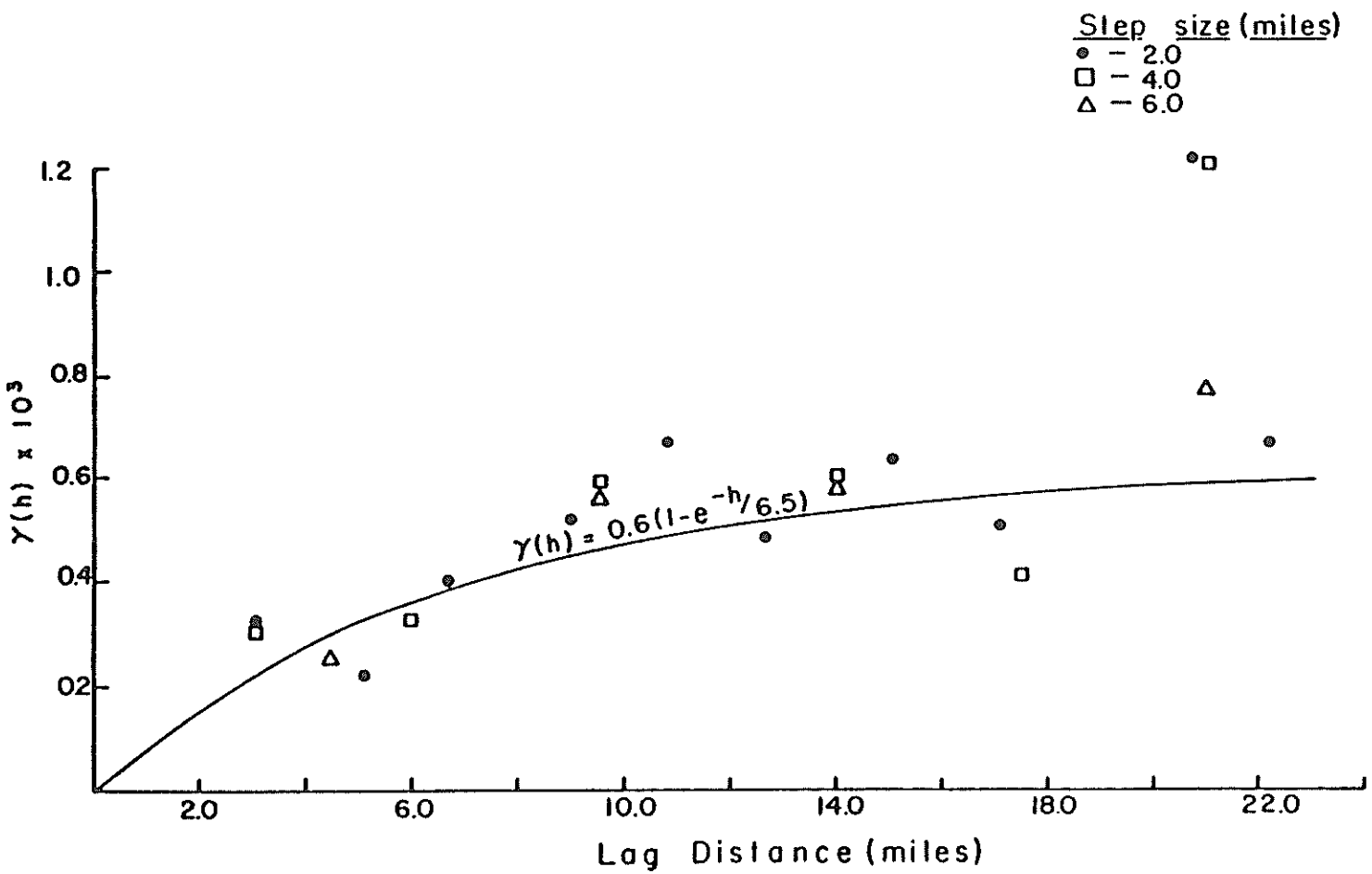

Figure 19. Variogram of Hydraulic Head in the San Jose Formation.

The points of kriging estimation were the node points of the numerical model. Since the kriging was performed on the hydraulic head residuals, the actual kriged estimates of hydraulic head were calculated by adding multiple linear regression estimates of hydraulic head with the kriged residual estimates. Contours of these values for the Ojo Alamo, Nacimiento, and San Jose formations are presented in figures 9, 10, and 11 respectively. The computer program KRIG was used to perform the calculations. In addition, this program calculates the kriging variance.

Groundwater dating by the solute-transport method requires estimates of the dispersivity. Stochastic solute-transport theory provides a means of determining the magnitude of the dispersivity but the statistical properties of the hydraulic conductivity distribution must be known. In the theory section, a technique was developed to estimate hydraulic conductivity from electrical resistivity and aquifer pump test data. A multi-purpose fortran computer program, LOGANS, was written to estimate the spatial distribution of the hydraulic conductivity field from electrical resistivity data. Essentially, the algorithm calculates the hydraulic conductivity of each sandstone zone by equation 3.4. An effective hydraulic conductivity is determined by calculating the weighted average hydraulic conductivity. The weighting factor is the relative thickness of the sandstone zones. The strata included in the calculations were determined by visual examination of each electric log. Most of these sandstone zones belong to the Ojo Alamo Sandstone stratigraphic unit. In total, 79 electric logs were examined. These logs were located in the vicinity of the flow path shown on figure 20. The aquifer pump tests used to calibrate equation 3.4 were also conducted in wells located on this flow path. These wells are both located in 25.09.10.111. Each of the wells was completed in both the Ojo Alamo and the Nacimiento. Completion in both formations was not desirable but no alternative wells were available for calibration purposes.

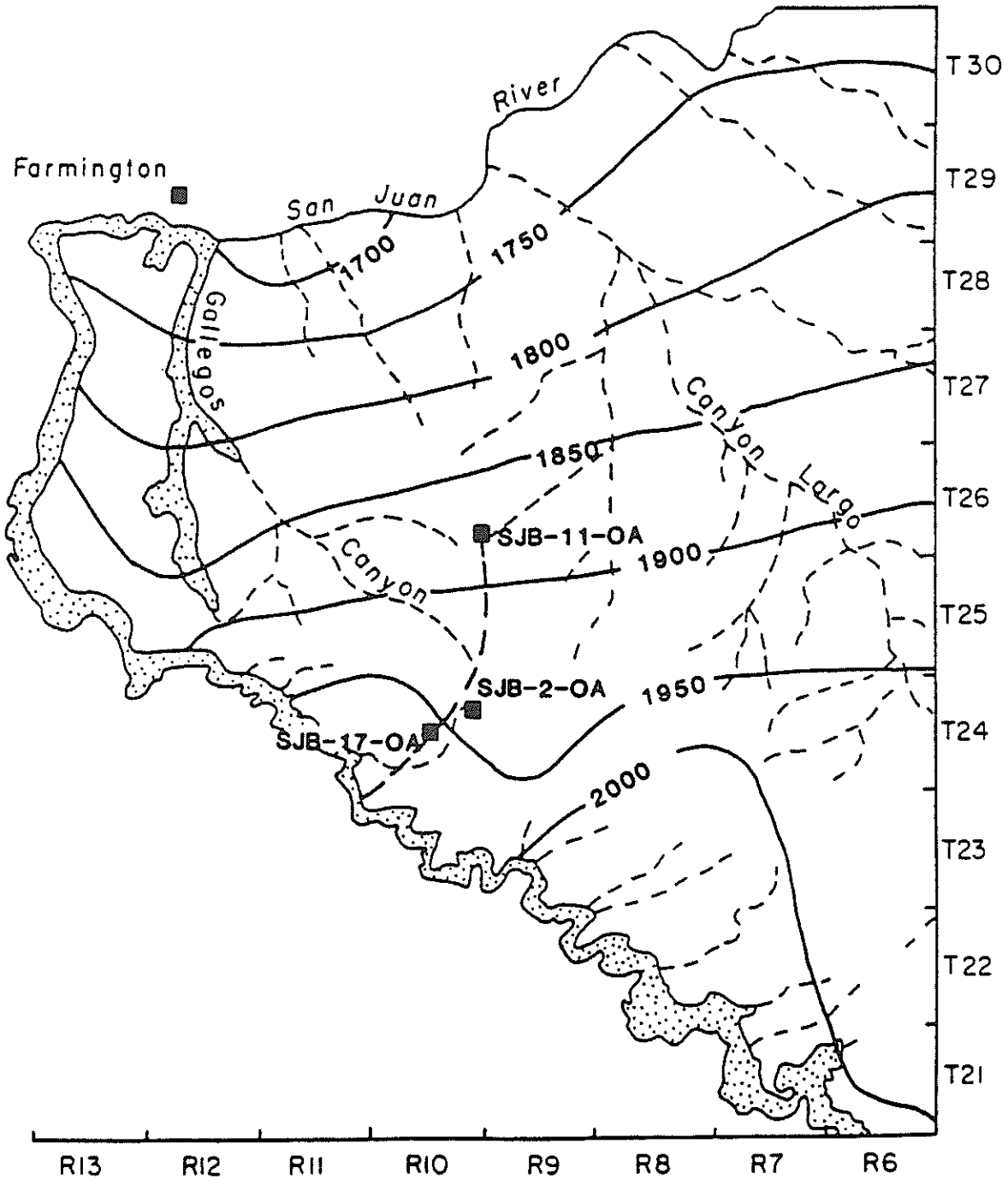

Figure 20. Groundwater Flowpath in the Ojo Alamo Aquifer.

The program LOGANS was used to calculate the effective hydraulic conductivity at each of the 79 electric log locations. Linear surface fitting to the estimated hydraulic conductivities showed no significant directional trends along the flow path. The statistical properties of the hydraulic conductivity field were subsequently analyzed using the computer program VGRAM. The orientation of the hydraulic conductivity data points required an anisotropic variogram to provide the best fit. The correlation length scale was estimated by inverting the variogram (equation 5.1) as discussed previously in the theory section. Figures 21 and 22 are the variograms and covariance relations of the estimated hydraulic conductivity distribution. The variance and correlation length scale properties are listed below.

$$\sigma_k^2 = 779 \text{ m}^2/\text{yr}^2$$
$$\lambda = 2253 \text{ m}$$

It should be noted the hydraulic conductivity values estimated from the electrical resistivity logs were not used in the numerical model. The variance and the correlation length scale were the only properties of the hydraulic conductivity distribution employed. These valves were used in the calculation of aquifer dispersivity.

Groundwater Dating

As discussed in the theory section, several groundwater dating models of varying degrees of complexity can be proposed. The simplest model is an ideal tracer traveling in a non-dispersed fashion. More sophisticated models include dispersion, diffusion, chemical reactions, and groundwater mixing. In this section, chemical reactions and groundwater mixing models will not be treated. In the discussion, these factors will be briefly examined.

For this study, a Fortran computer program, MACDAT, was developed to calculate groundwater ages. It incorporates information about initial carbon-14 activity, the effects of dispersion and aquitard diffusion on final carbon-14 activities,

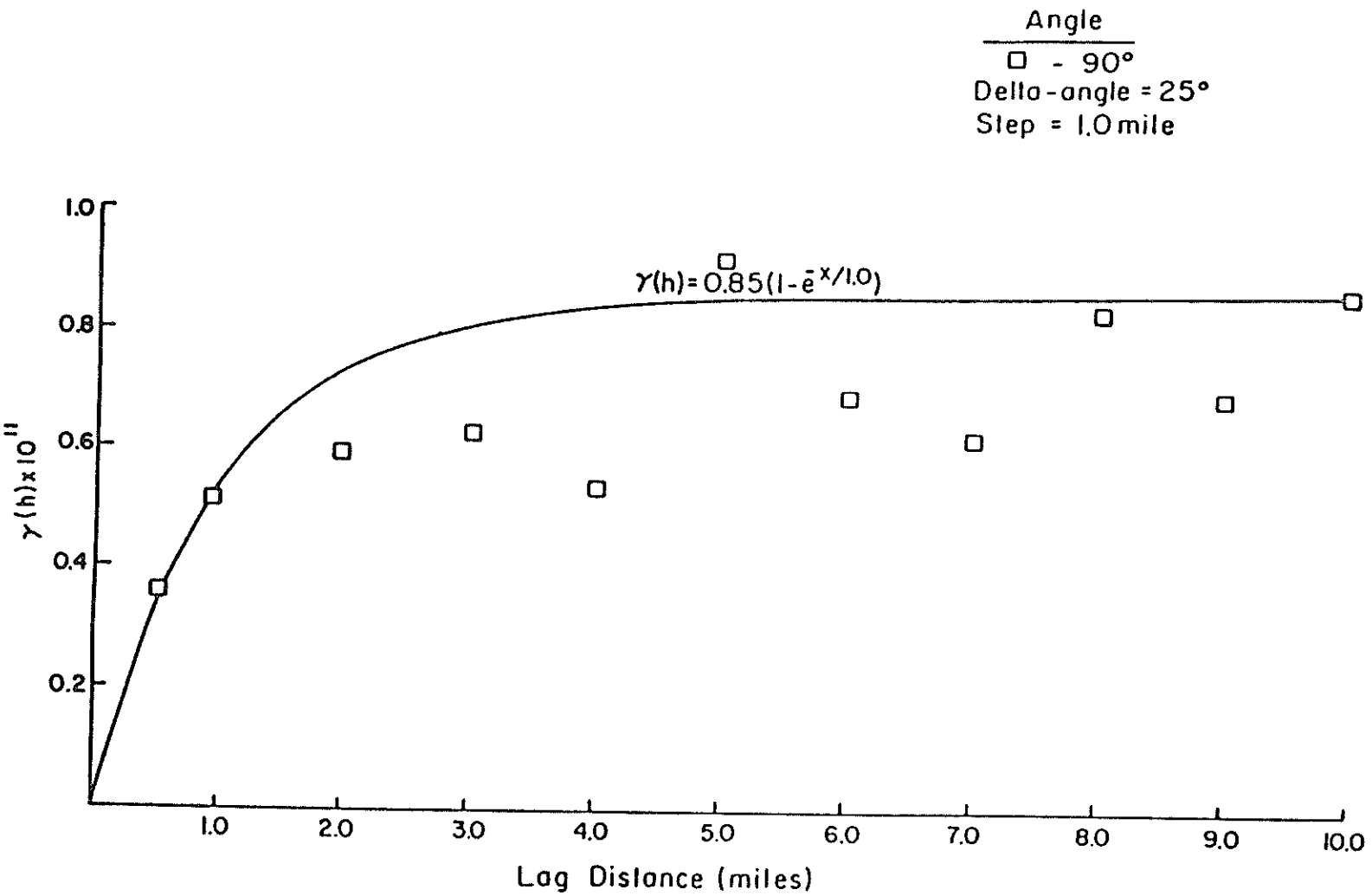

Figure 21. Variogram of Estimated Hydraulic Conductivity.

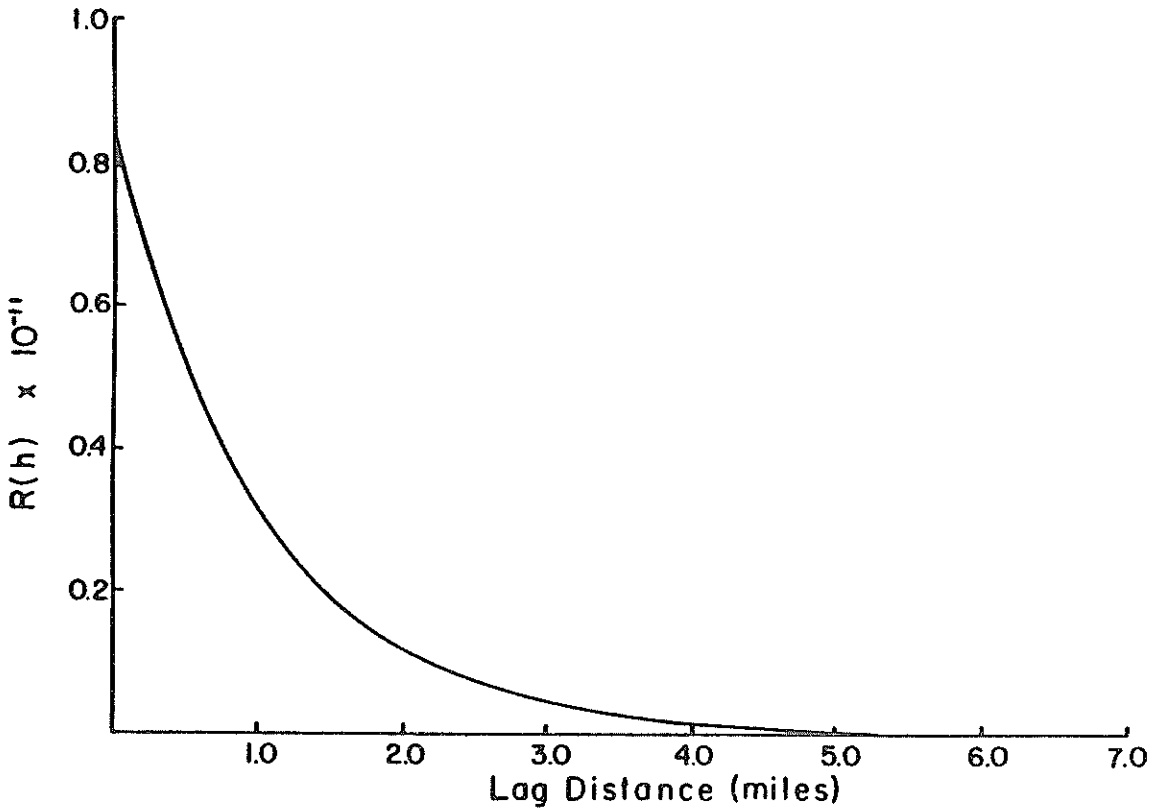

Figure 22. Covariance of Estimated Hydraulic Conductivity.

hydraulic gradients, and flow path length. The initial carbon-14 activities used in MACDAT were calculated by Fontes' method. The main reason for selecting this method is that it accounts for changes in carbon-14 activities after groundwater recharge. Table 4 contains the carbonate water chemistry data used for the calculation of the initial carbon-14 activities of samples SJB-18 through SJB-35. Table 5 presents the results of the calculations of initial activity by the various methods.

The program algorithm determines groundwater age by successive approximations. First, a piston-flow estimate is calculated using equation 1.5. Given the model assumptions (ideal tracer), this age represents the maximum likely groundwater age. From this age and a known value for the flow path length, a corresponding groundwater velocity can be determined:

$$U = \frac{l}{t} \qquad \textbf{(7.1)}$$

where l and t are the flow path length and groundwater age respectively. The hydraulic conductivity associated with this mean velocity is given by

$$K = \frac{Un}{J} \qquad \textbf{(7.2)}$$

The coefficient of variation of the hydraulic conductivity can be calculated by

$$C_k^2 = \frac{\sigma k^2}{K^2} \qquad \textbf{(7.3)}$$

MACDAT proceeds to calculate all the parameters required for the solution of equation 2.20 using equations 7.1, 7.3, and the estimated correlation length scale. It also contains an option to include diffusion of carbon-14 into the surrounding aquitards.

The solution of equation 2.20 with these parameters results in a calculated value for the activity ratio (A/Ao). Inasmuch as the observed activity ratio (A/Ao) is known, the difference

Table 4. Chemical Analyses of Selected Water Samples.

Sample No.	Bicarbonate (HCO_3^- mg/l)	Carbonate (CO_3^{2-} mg/l)	pH (Standard Unit)
SJB-18-N	335.5	180.0	7.9
SJB-19-CM	52.5	0	8.7
SJB-21-N	146.4	0	7.7
SJB-22-N	359.9	84.0	9.3
SJB-23-N	561.2	36.6	9.1
SJB-24-N	658.8	24.0	8.7
SJB-25-N	536.8	0	7.6
SJB-27-CM	847.9	0	7.2
SJB-28-CM	207.4	0	7.6
SJB-29-CM	268.4	24.0	8.9
SJB-30-CM	164.7	0	8.1
SJB-31-N	341.6	0	7.6
SJB-32-CM	170.8	0	7.7
SJB-33-CM	347.7	0	8.4
SJB-34-CM	469.7	36.0	9.1
SJB-35-N	366.0	180.0	9.9

Table 5. Initial Carbon-14 Activities Calculated by the Five Models.

Sample No.	Name	Tamers	Mook	Vogel	Pearson	Fontes
SJB-01-0A	Lybrook	43.5	80.1	85.0	84.6	68.5
SJB-02-0A	B of C Mission	41.4	92.7	85.0	81.9	69.5
SJB-03-0A	Pete Spring	51.6	-15.6	85.0	44.5	22.5
SJB-04-0A	Powerline WM	48.0	79.8	85.0	81.2	65.4
SJB-05-0A	Kimbeto WM	49.6	91.7	85.0	84.6	70.2
SJB-06-0A	Ojo Socorro	50.3	-43.1	85.0	31.6	10.5
SJB-08-0A	Dzilth	49.1	118.9	85.0	98.9	89.2
SJB-09-0A	Ojo Encino	55.4	-274.1	85.0	41.1	12.6
SJB-10-0A	Johnsons TP	45.9	95.4	85.0	83.2	70.3
SJB-11-0A	Huerfano #2	49.7	90.9	85.0	91.4	73.9
SJB-12-0A	Huerfano #1	46.2	92.5	85.0	79.8	69.3
SJB-13-0A	Nageezi CH	45.3	106.8	85.0	89.4	77.8
SJB-14-0A	Chaco Camp #9	50.5	84.5	85.0	89.4	71.7
SJB-15-0A	Hilltop	50.1	88.9	85.0	89.4	73.2
SJB-16-0A	Kah-Des-Pah	45.8	111.0	85.0	88.7	77.8
SJB-17-0A	Tsah Tah	47.1	82.2	85.0	75.1	63.2
SJB-18-N	Largo School	52.6	150	85.0	163	147
SJB-19-CM	Pat Montoya	49.2	71.2	85.0	79.8	59.9
SJB-21-N	Tenneco	52.6	118	85.0	90.0	67.7
SJB-22-N	Huerfano TP	45.4	63.5	85.0	77.8	64.8
SJB-23-N	19T-342	47.1	56.8	85.0	63.5	44.5
SJB-24-N	19T-349	49.1	69.2	85.0	75.8	56.0
SJB-25-N	29T-298	53.3	108	85.0	63.5	39.6
SJB-27-CM	NW Pipeline #11	57.5	147	85.0	100	75.4
SJB-28-CM	NW Pipeline #13	53.6	138	85.0	112	90.6
SJB-29-CM	EPNG Gonzales	48.1	86.6	85.0	75.8	61.7
SJB-30-CM	EPNG 27-5	50.7	101	85.0	101	81.0
SJB-31-N	EPNG Ridge	52.9	112	85.0	74.4	52.2
SJB-32-CM	EPNG Gould	52.7	116	85.0	86.0	66.0
SJB-33-CM	EPNG Largo	49.8	83.0	85.0	88.7	68.9
SJB-34-CM	EPNG Lindrith	47.1	66.6	85.0	80.5	62.7
SJB-35-N	EPNG Ballard #1	34.1	66.0	85.0	85.3	78.7

between the known and the calculated activity ratios represents the error in the flow-field parameters. Refinement of these parameters can be achieved by making a new estimate of the mean velocity. Using this revised value, equations 7.2 and 7.3 are recalculated. A new age is computed by resolving equation 7.1 for t. Using the revised parameter estimates, equation 2.20 is also resolved to determine a new activity ratio. The entire estimation process can be repeated until some arbitrary acceptance criteria is achieved. For this study, the criteria was a difference between the observed and calculated activity ratios of less than 10^{-4}. Table 6 presents the values of the aquifer and aquitard parameters used in the analyses. Table 7 reports the carbon-14 activities and flow-path characteristics used for the dispersion and aquitard diffusion analysis. Figure 20 shows the locations of the samples along the flow path.

Table 6. Parameters Used in Groundwater Dating Analysis.

Property	Aquifer	Aquitard
Correlation Length Scale (λ)	2,253 m	-
Diffusion (D') m^2/yr	-	2.21×10^{-2}
Porosity (n & n')	0.20	0.10 or 0.20
Carbon-14 Decay Constant (β)	1.21×10^{-4} yr^{-1}	Same
Hydraulic Conductivity Variance (σ_k^2)	779 m^2/yr^2	-
Thickness (b)	50 m	(assumed)

The value for aquitard diffusion was obtained from Neretnicks (1980). It was reported to be an average value for shales. No site-specific data were available.

Table 7. Carbon-14 Activities and Flow Path Characteristics.

Sample No.	A_o pmc	A pmc	dh m	l m
SJB-17-0A	63	40	25	11,600
SJB-02-0A	70	29	40	16,200
SJB-11-0A	74	5	90	36,700

h is change in the hydraulic head from the recharge area to the observation point. The sample SJB-08-0A was not included in these calculations because the well from which this sample was taken is completed primarily in the Nacimiento formation and not in the Ojo Alamo Sandstone as are the other three wells. Examination of table 5 also reveals the initial activity of SJB-08-0A is quite different from the other wells found along the flow path.

Several groundwater dating models were examined at sample locations along the flow path shown on figure 20. The assumptions and methods used to determine groundwater ages have been discussed in previous sections. Table 8 shows groundwater ages calculated by three different models.

Table 8. Groundwater Ages in Years.

Sample No.	Type of Model			
	Pure Convective	Dispersive	Dispersive with Aquitard Diffusion n' = 0.1	n' = 0.2
SJB-17-0A	3,754 ± 185	3,754	3,343	3,014
SJB-02-0A	7,283 ± 250	7,285	6,487	5,847
SJB-11-0A	22,270 ± 1,100	22,290	19,850	17,890

The difference between the piston flow (pure convective) and the dispersive ages is less than 1 percent. The effect of diffusion is, however, more significant. In this case, the differences range from 11 to 20 percent. It can be seen that a doubling of aquitard porosity from 0.1 to 0.2 increases the discrepancy between the piston flow and the dispersive/diffusive ages by 9 percent. The effect on the piston flow age due to the uncertainty in the laboratory determination of the carbon-14

activity is indicated on table 8. It can be noted that in all cases the piston flow and dispersive models differ by much less than the uncertainty in the groundwater age due to analytical methodology. The same is not true for the dispersive/diffusive ages. For an effective aquitard porosity of 10 percent, the calculated age is 2 to 3 times smaller than can be accounted for by the magnitude of the analytical uncertainty. A doubling of the porosity proportionately increases this discrepancy.

The piston flow and dispersive model ages are essentially the same. This is because the coefficients of dispersion determined by the one-dimensional stochastic transport method are relatively small. Table 9 presents dispersivity values determined by the solute transport calibration process previously described.

Table 9. Dispersivity Values in Meters.

Sample No.	Type of Model		
	Dispersive	Dispersive/Diffusive n' = 0.1	Dispersive/Diffusive n' = 0.2
SJB-17-0A	1.56	1.13	0.85
SJB-02-0A	4.94	3.61	2.72
SJB-11-0A	10.78	7.99	6.08

Considering the regional scale, these values are quite small. Using a geochemical calibration method, Wood (1981) reported coefficients of dispersion in a regional flow system approximately 100 to 1,000 times greater than reported here. In part, the explanation for this discrepancy is probably related to the insensitivity of the activity ratio to the magnitude of the dispersivity. Sudicky and Frind (1981) have remarked on this characteristic. Another part of the explanation concerns the process by which the statistical properties of the hydraulic conductivity distribution were estimated. This was done by assuming a mathematical model relating the electrical resistivity to the hydraulic conductivity. Although the coefficients of the model were calibrated to aquifer pumping tests, the form of the functional relationship probably does not sufficiently

reduce the hydraulic conductivity of sandstones containing significant amounts of shale. Inasmuch as the magnitude of dispersion is proportional to the variance of the hydraulic conductivity distribution, this characteristic of the assumed functional relationship reduces the coefficient of dispersion.

It should be noted, however, that from a groundwater dating perspective exact knowledge of the coefficient of dispersion is not critical. This is because of the insensitivity of the solution of the solute transport equation to the dispersion parameter. The magnitude of the error due to neglecting the effect of diffusion into the aquitards is likely to be larger than the error due to the uncertainty in the dispersivity.

Another interesting observation can be made from table 9. Neglecting the diffusion of carbon-14 into the surrounding aquitards results in an overestimation of the magnitude of dispersivity. This is due to the diffusive reduction in tracer concentration accounting for part of the lowered activity. As diffusion becomes more important, the magnitude of error associated with estimating dispersivity by a solute transport calibration without accounting for diffusion grows proportionately. This overestimation ranges from approximately 1.3 to 1.8 times too large for the values given in Table 10.

Without doubt, one of the major contributions of stochastic hydrology has been to provide a physically based explanation and mathematical description of dispersion. Part of this success is the prediction of the scale dependence of dispersivity. The asymptotic form of the increase in dispersivity has been discussed previously. Figure 23 is a graph of dispersivity at various distances along the flow path on figure 20. The general form of the dispersivity-distance relationship is approximately correct inasmuch as the rate of increase in the dispersivity is declining as the distance increases. A complete curve from the origin through all the points cannot be readily drawn. Most probably, this is because the mean value of the hydraulic conductivity along the flow path is not constant.

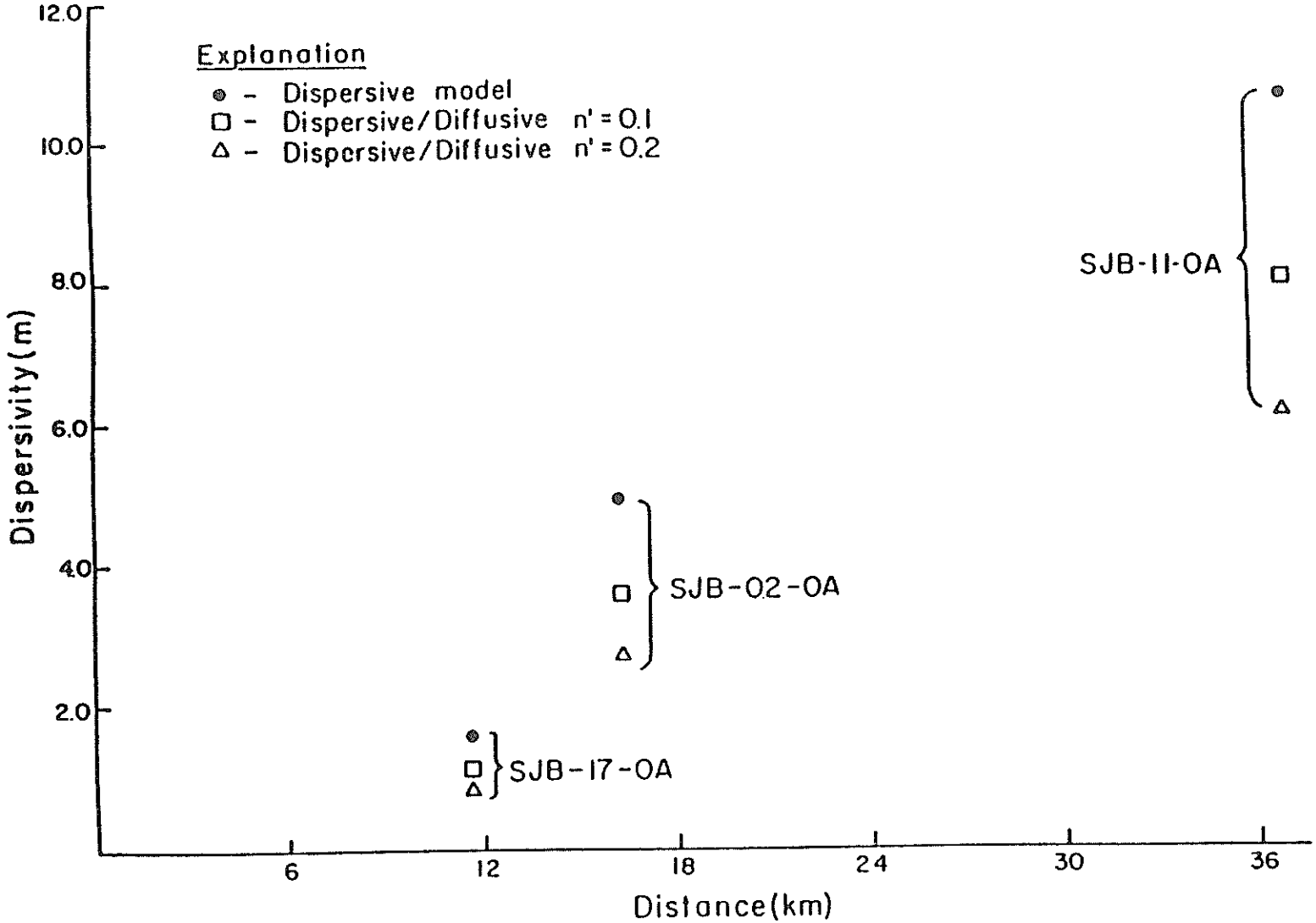

Figure 23. Relationship of Dispersivity to Distance.

This is indicated by examining the hydraulic conductivities shown on figure 31. In the area contained in Township 24 North, Range 10 West, the hydraulic conductivity decreases significantly. This reduction occurs at a distance of approximately 12 km down the flow path and continues for about another 8 km. This interval contains the middle point (SJB-02-0A) shown on figure 23.

Leakage and/or recharge of groundwater in the Ojo Alamo aquifer could also have a significant effect on the calcuation of groundwater ages. As the magnitude of the leakage/recharge becomes greater so does the potential for incorrect ages. A rigorous correction of reported groundwater ages is beyond the scope of this study. However, some indication of the magnitude of potential errors can be obtained by examining the proportion of leakage relative to the total horizontal flow volume. Table 10 presents vertical fluxes along the Ojo Alamo flow path shown on figure 20.

Table 10. Vertical Fluxes along Ojo Alamo Flow Path.

Grid Element		Vertical Fluxes (cfs/mi^2)		
Row	Column	Recharge	Discharge	Net
13	7	2.4×10^{-2}	1.6×10^{-2} 1/	0.8×10^{-2}
12	8	3.1×10^{-4}	1.7×10^{-2}	-1.7×10^{-2}
11	9	1.9×10^{-3}	6.2×10^{-3}	-4.3×10^{-3}
10	9	8.8×10^{-5}	7.9×10^{-4}	-7.0×10^{-4}
9	9	3.8×10^{-2}	5.6×10^{-3}	3.2×10^{-2}

1/ This flux was estimated from an adjacent node.

The groundwater flow model code was modified to calculate vertical fluxes on a grid basis. These values were converted to a square mile basis for purposes of comparison with horizontal fluxes. Over most of the flow path, the net vertical discharge is greater than the recharge. The notable exceptions are at the outcrop node (13, 7) and node (9, 9) (figure 33). To obtain an estimate of the possible effects of vertical recharge, a comparison of the vertical and horizontal fluxes was made. The data and results are presented in Table 11.

Table 11. Comparison of Vertical and Horizontal Fluxes.

Grid Element Row	Grid Element Column	Transmissivity (ft^2/s)	Hydraulic Gradient (ft/ft)	Horizontal Flux (cfs/mi width)	Ratio of Vertical to Horizontal Flux
13	7	5.4×10^{-3}	2.8×10^{-3}	0.8×10^{-2}	3.00
12	8	6.1×10^{-4}	2.2×10^{-3}	7.3×10^{-3}	0.04
11	9	2.1×10^{-3}	1.6×10^{-3}	1.8×10^{-2}	0.10
10	9	2.8×10^{-3}	1.4×10^{-3}	2.1×10^{-2}	0.01
9	9	8.1×10^{-3}	1.8×10^{-3}	7.9×10^{-2}	0.48

The horizontal fluxes were calculated using the nodal transmissivities and estimates of the hydraulic gradient. The ratio of the recharge to the horizontal flux was computed using the data in tables 10 and 11. Except for nodes (13, 7) and (9, 9), the recharge component is less than 10 percent of the horizontal flux. Node (13, 7) is an outcrop boundary node which explains why it has such a large component of recharge flux. The ratio of recharge flux to horizontal flux is greater than 1 because vertical discharge is also occurring at the boundary node. Node (9, 9) appears to have an anomalously high recharge flux. This could imply a potential for an incorrect age estimate. It should be noted, however, that the aquitard hydraulic conductivities, which were adjusted only as minimally as possible from the thermally estimated values, are quite high compared to the usual range of shale values. This probably results in an overestimation of the vertical fluxes.

In general, this limited evaluation of the potential effect of vertical recharge indicates that the computed groundwater ages should not be greatly affected by leakage.

Figures 24, 25, and 26 show groundwater ages calculated at various points in the study area for the Ojo Alamo, Nacimiento, and San Jose Formation, respectively. These dates are all based on the piston-flow model. Examination of groundwater ages on figure 26 reveals that vertical flow in the San Jose may be influencing the groundwater age distribution.

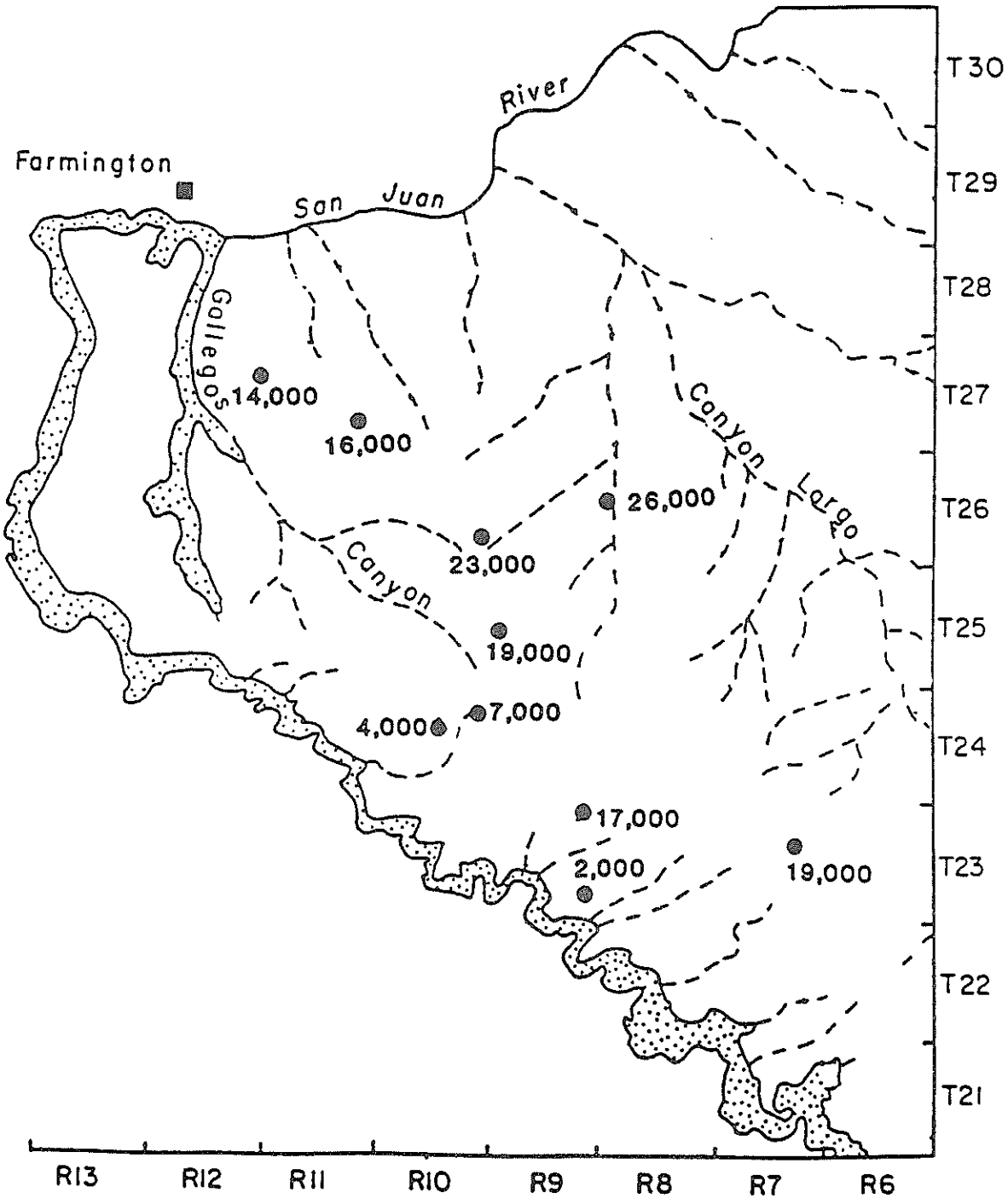

Figure 24. Groundwater Ages (Years) in the Ojo Alamo Sandstone.

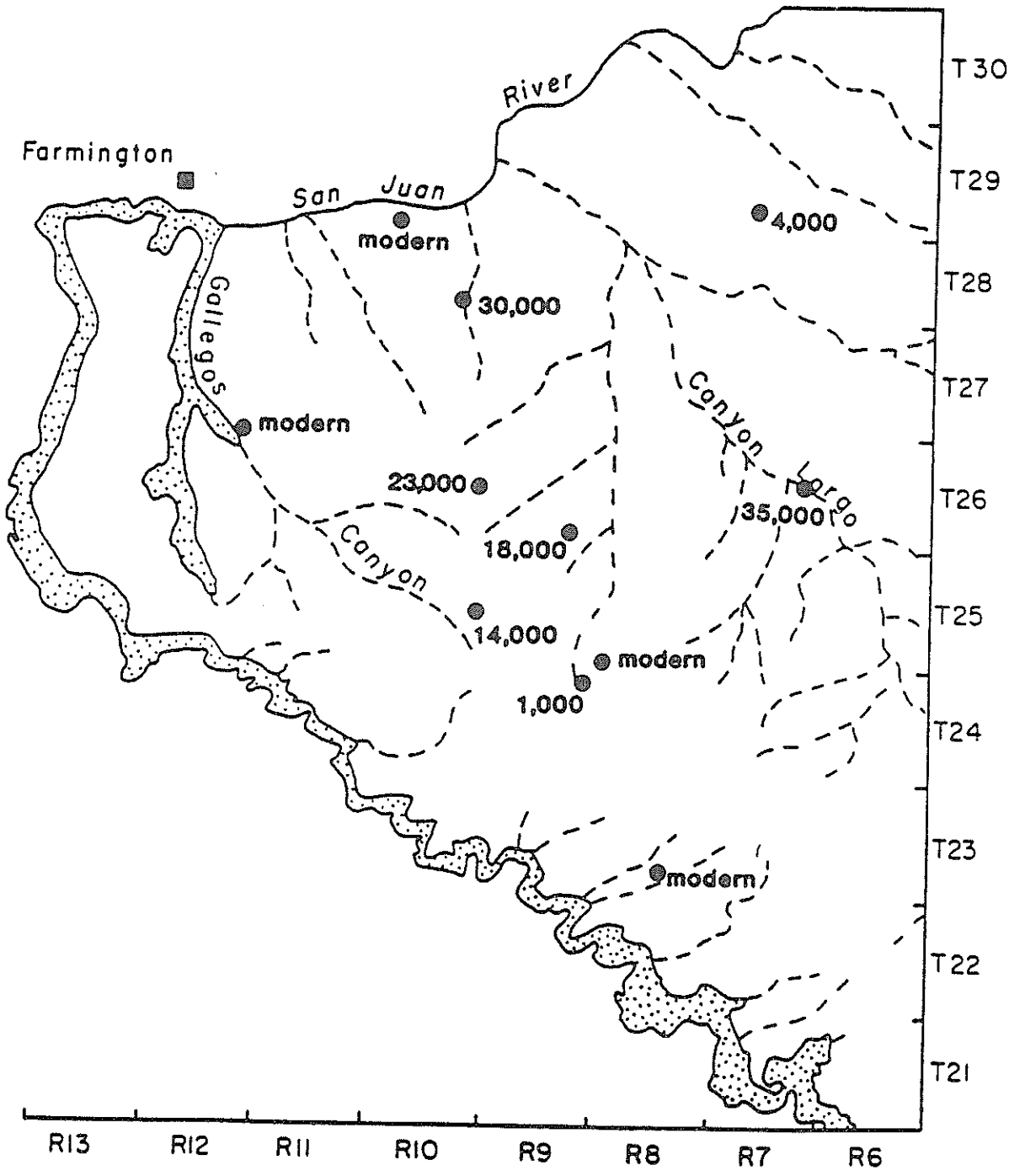

Figure 25. Groundwater Ages (Years) in the Nacimiento Formation.

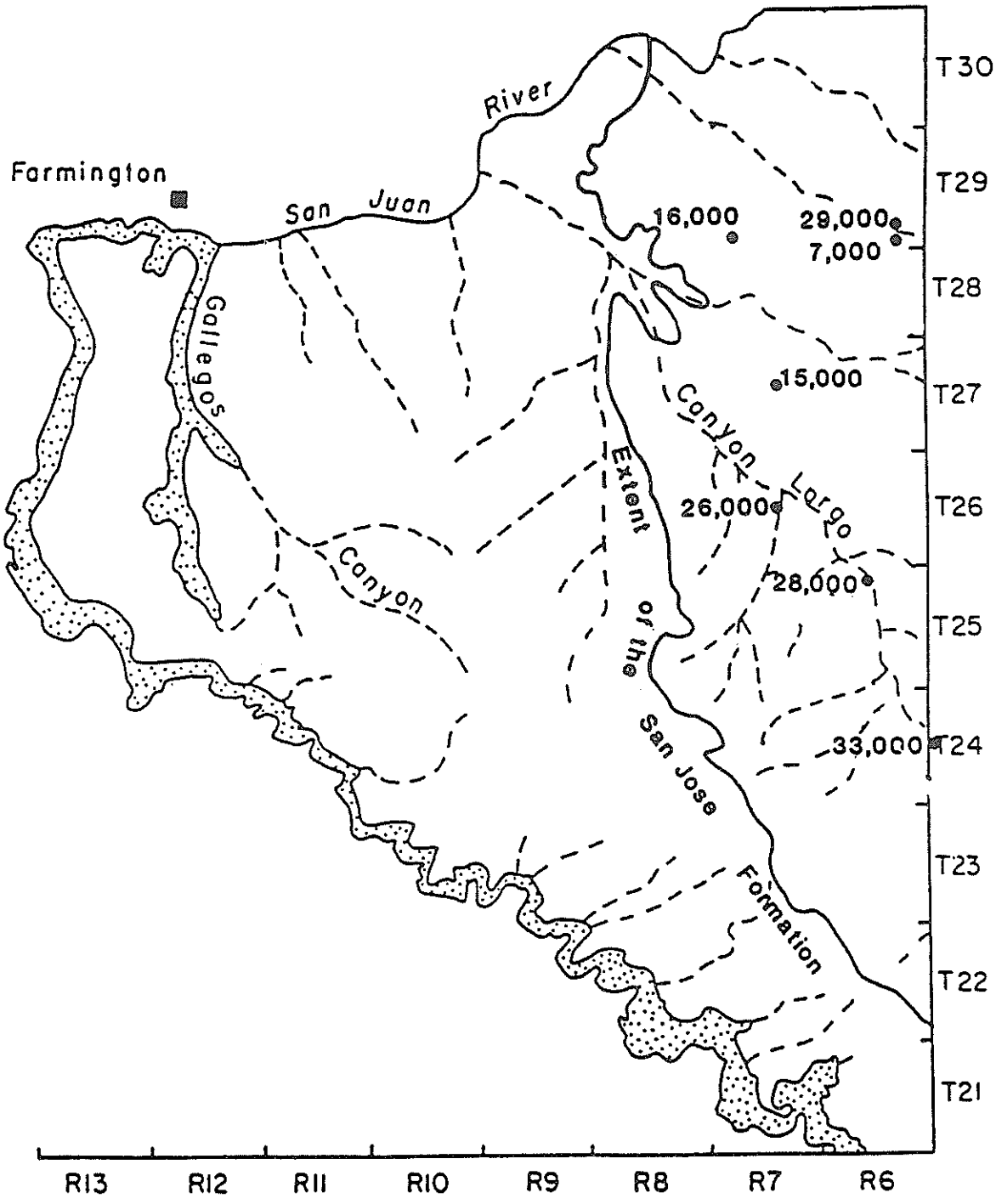

Figure 26. Groundwater Ages (Years) in the San Jose Formation.

A change in the chemical composition of the groundwater may also complicate the carbon-14 dating. The major potential problem is carbonate dissolution in the aquifer. Dissolved carbonates lower the measured activity of water and cause the age to be overestimated. Precipitation of carbonates is not nearly as serious a source of error. In this case, isotopic fractionation during precipitation causes a larger reduction in the concentration of carbon-14 in solution than it does for the other carbon species. The magnitude of the effect depends on the extent of precipitation. It is possible to correct for both dissolution and precipitation of carbonates by using an appropriate reaction path model.

To gain some insight into the chemical processes, carbonate concentrations along the flow path on figure 20 can be examined. From table 2, it can be seen that the total dissolved carbon (TDC) changes from 408 to 309 mg/l between SJB-17-0A and SJB-02-0A. Over this same section, all the major cations (calcium, magnesium, and sodium) also decrease. On the basis of charge balance, the sulfate concentration may also be estimated to decrease. These observations indicate that the most likely chemical reactions occurring are precipitation of various carbonate and sulfate minerals and ion exchange with clay minerals. This latter reaction is suggested because the potentiometric surface, groundwater ages, and the electric logs all indicate this area to have a high clay content. If the previously discussed geologic interpretation of a swampy depositional environment for the Ojo Alamo Sandstone in this area is correct, it might be reasonable to expect this part of the flow path to have been leached of carbonates and sulfates. The possibility then exists for precipitation of these minerals to occur. As discussed, the effect of the precipitation of carbonates should not greatly affect the groundwater ages.

Further along the flow path, between SJB-02-0A and SJB-11-0A, the carbonates continue to decrease to 271 mg/l. The major cations and sulfate, however, both increase. The implica-

tion here seems to be that gypsum is dissolving and carbonates are precipitating. Given the greater solubility of gypsum relative to calcite, this incongruent solution seems reasonable.

The entire reaction path may be envisioned in three parts. Recharge through the vadose zone dissolves carbonate and sulfate minerals. Between SJB-17-0A and SJB-02-0A, the reaction path mechanism is uncertain. If the analytical data is correct, the observed chemical composition of the groundwater requires the precipitation of sulfate and carbonate minerals. The water is, however, undersaturated with respect to mirabilite ($Na_2SO_4 \cdot 10H_2O$) and trona ($NaHCO_3 \cdot Na_2CO_3 \cdot 2H_2O$). Down the flow path, the resulting calcium-depleted groundwater dissolves gypsum which in turn promotes calcite precipitation resulting in the lowered carbonate concentration. The gypsum dissolution combined with ion exchange with clay minerals creates the observed increases in the concentrations of calcium, sodium, and sulfate.

This proposed reaction path has not been examined in any quantitative way during this study. If it is reasonably correct, actual groundwater ages should be relatively close to the values presented because calcite dissolution, except in the vadose zone, does not play a role.

In the proceeding discussion, the effects of dispersion, diffusion into aquitards, vertical recharge, and chemical reactions have all been evaluated with respect to part of the Ojo Alamo aquifer flow system. Each of these processes has the potential to alter the calculated groundwater age. In this study, the greatest deviation from the piston flow ages appears to result from neglecting diffusion into the surrounding aquitards. In this case, however, the magnitude of the difference is estimated to be only about 15 percent. This discrepancy is well within the uncertainty inherent in constructing the isochrons. It was, therefore, decided that the hydraulic conductivity of the Ojo Alamo and Nacimiento aquifers could be reasonably estimated from the piston flow ages.

Determining Hydraulic Conductivity from Groundwater Ages

The groundwater dating process produces only point-specific determinations of ages. Estimation of aquifer hydraulic conductivity requires these ages to be interpreted throughout the flow domain by constructing a series of isochrons. The hydraulic conductivity can then be determined. A point worth discussing is the meaning of this calculated hydraulic conductivity. It is a mean value which does not reflect the variability of the hydraulic conductivity along the flow path. To determine variations in the hydraulic conductivity, smaller segments along the flow path must be examined. If an assumption of steady-state flow is valid and leakage into and out of the aquifer are equal, the hydraulic gradient can be used to determine the hydraulic conductivity. Areal changes in the mean conductivity will be reflected by changes in the hydraulic gradient. Unless actual volumetric fluxes are known, the use of Darcy's law to calculate hydraulic conductivity requires that travel time, flow path length, hydraulic gradient, and aquifer porosity be known.

$$K = \frac{dl*n}{dt*J} \qquad (8.1)$$

where dl and dt are the elapsed distance and time, respectively, along the section of flow path for which K is being determined.

The travel time is obtained by constructing lines of equal age (isochrons) throughout the flow domain. This process requires interpolating the point-specific age estimates made by the groundwater-dating methods into a hydrologically reasonable series of isochrons. By examining flow paths, hydraulic gradients, and point-specific groundwater ages, a plausible series of isochrons can be drawn. Figures 27 and 28 show isochrons estimated for the Ojo Alamo and Nacimiento Formations. Figures 29 and 30 show, in addition, presumed flow paths in both of the formations. These figures also reveal an interesting aspect of groundwater dating. It is commonly assumed that isochrons

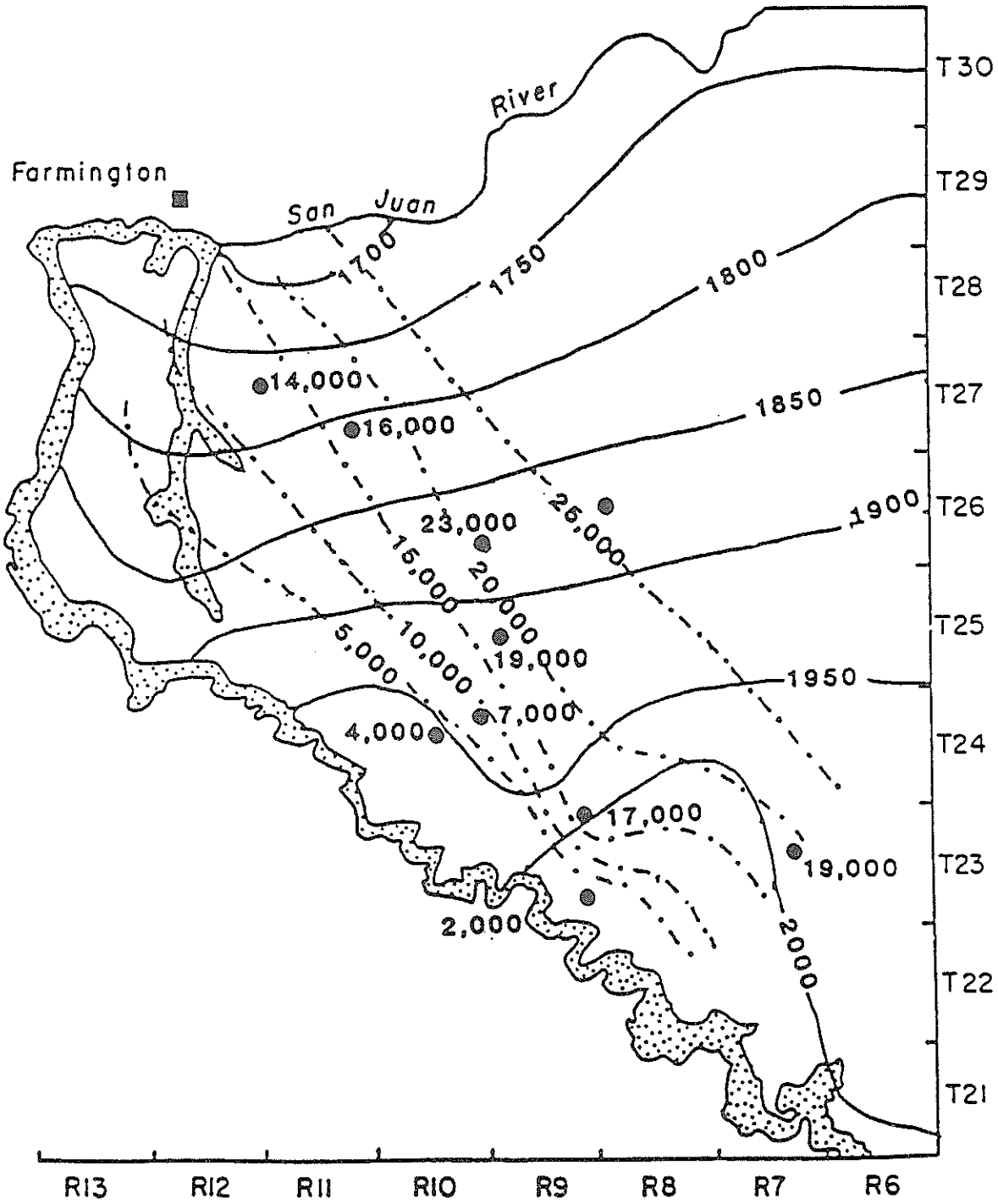

Figure 27. Isochrons in the Ojo Alamo Sandstone.

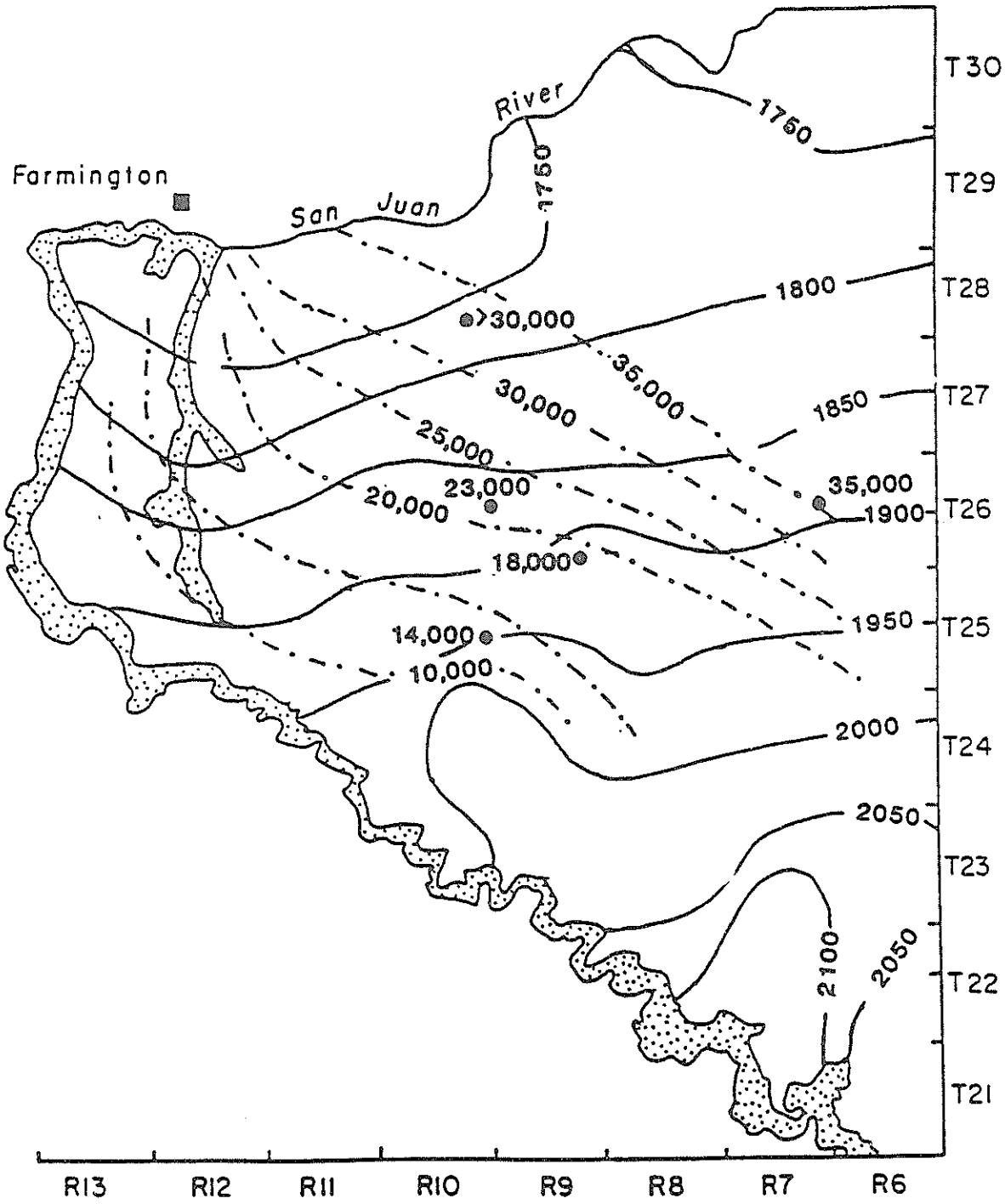

Figure 28. Isochrons in the Nacimiento Formation.

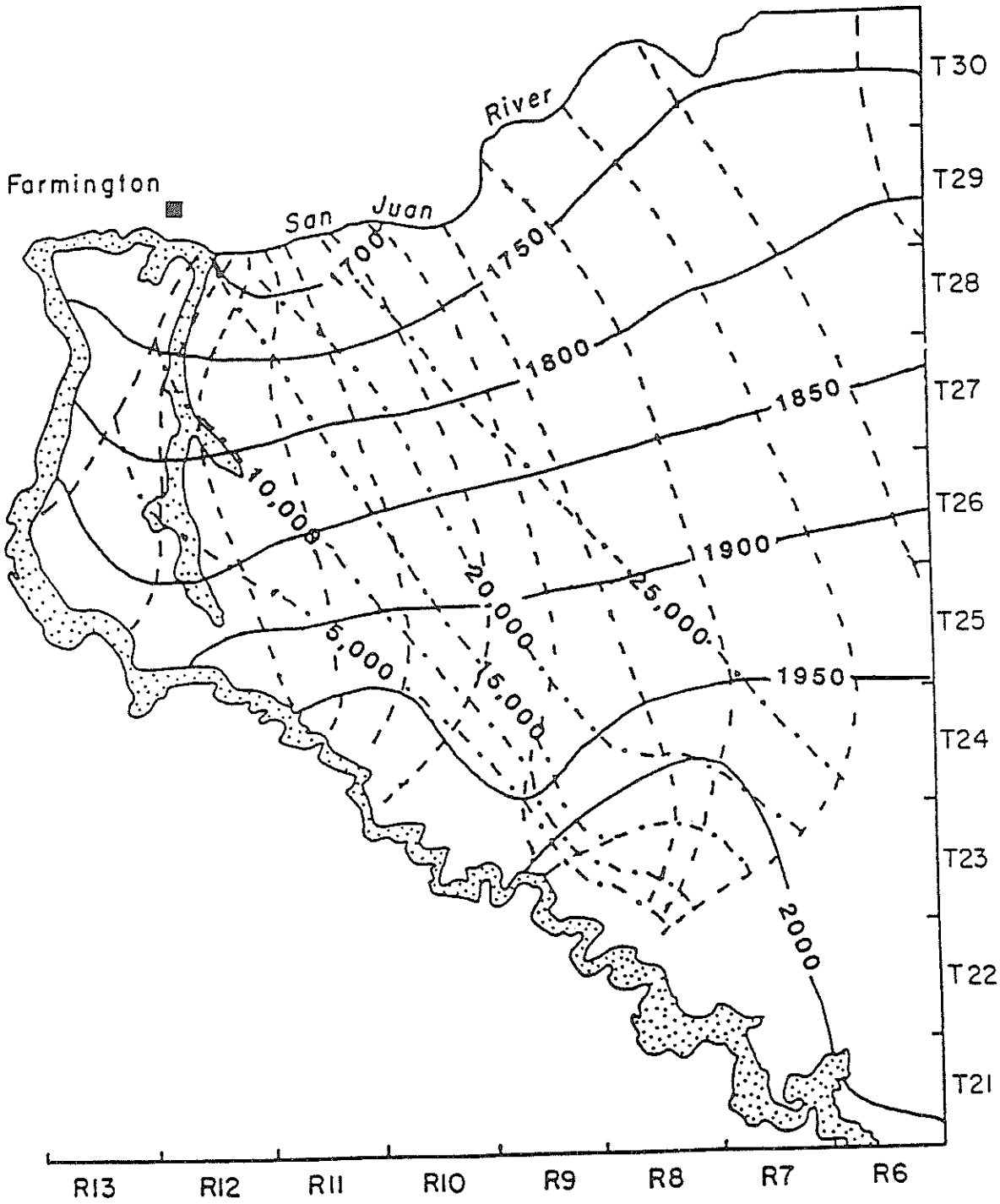

Figure 29. Flow Paths and Isochrons in the Ojo Alamo Sandstone.

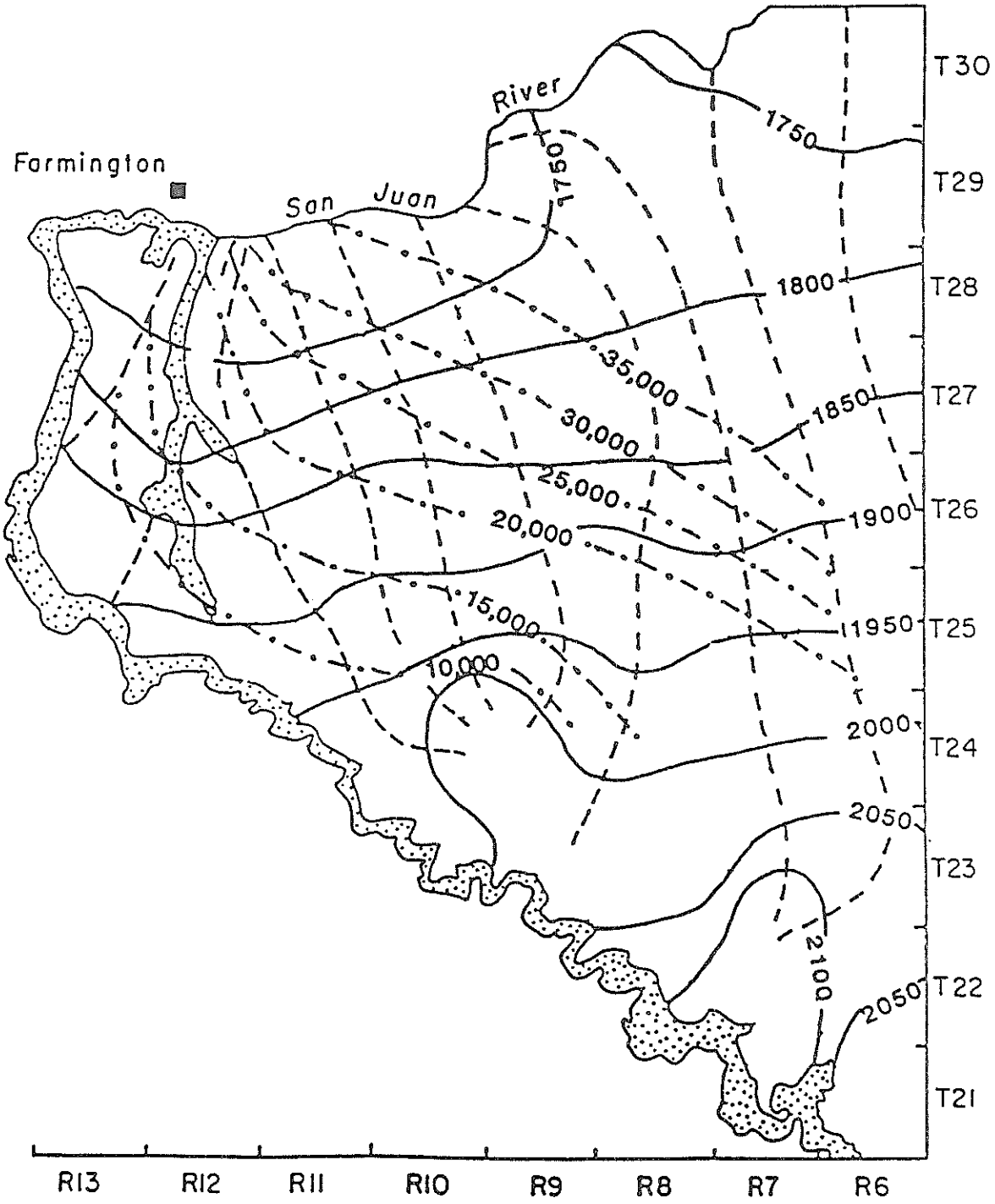

Figure 30. Flow Paths and Isochrons in the Nacimiento Formation.

should be parallel to the hydraulic head contours. This would be strictly true in a rectangular flow domain where groundwater movement was parallel to lateral no-flow boundaries. As the boundaries and boundary conditions become more complex, the isochrons are not so simply oriented. Examination of Figures 29 and 30 reveal that the connection between the flow paths, hydraulic gradients, and isochrons is hydrologically reasonable. This is important if valid estimates of the hydraulic-conductivity distribution are to be obtained.

The calculation of hydraulic conductivity is straightforward once Figures 29 and 30 have been constructed. Figures 31 and 32 present the results of these calculations for the Ojo Alamo and Nacimiento formations. The values shown are plotted midway along the flow path segment from which they were calculated. They represent the mean hydraulic conductivity of the aquifer over a specific oriented interval. They are not point values as might be measured by a laboratory or aquifer pump test. These hydraulic conductivities should, however, be reasonably similar to values determined by other methods.

Numerical Model and Aquifer Parameters

Numerical modeling of the study area was performed using a finite difference, quasi-three-dimensional code which was developed at New Mexico Institute of Mining and Technology by David Peterson. The model uses a strongly implicit procedure (SIP) to solve both transient and steady state groundwater flow equations. Leakage between layers is calculated by solving Darcy's law for flow across the aquitards. The node points are located at the centers of the grids shown on Figure 33.

Initially, a steady state calibration was performed. A total of four layers with intervening aquitards were included in the simulation. The top and bottom layers were used to simulate recharge/discharge conditions. These layers, referred to as layers 0 and 3, were treated as constant head boundaries. The Nacimiento and Ojo Alamo aquifers, respectively, comprised layers 1 and 2.

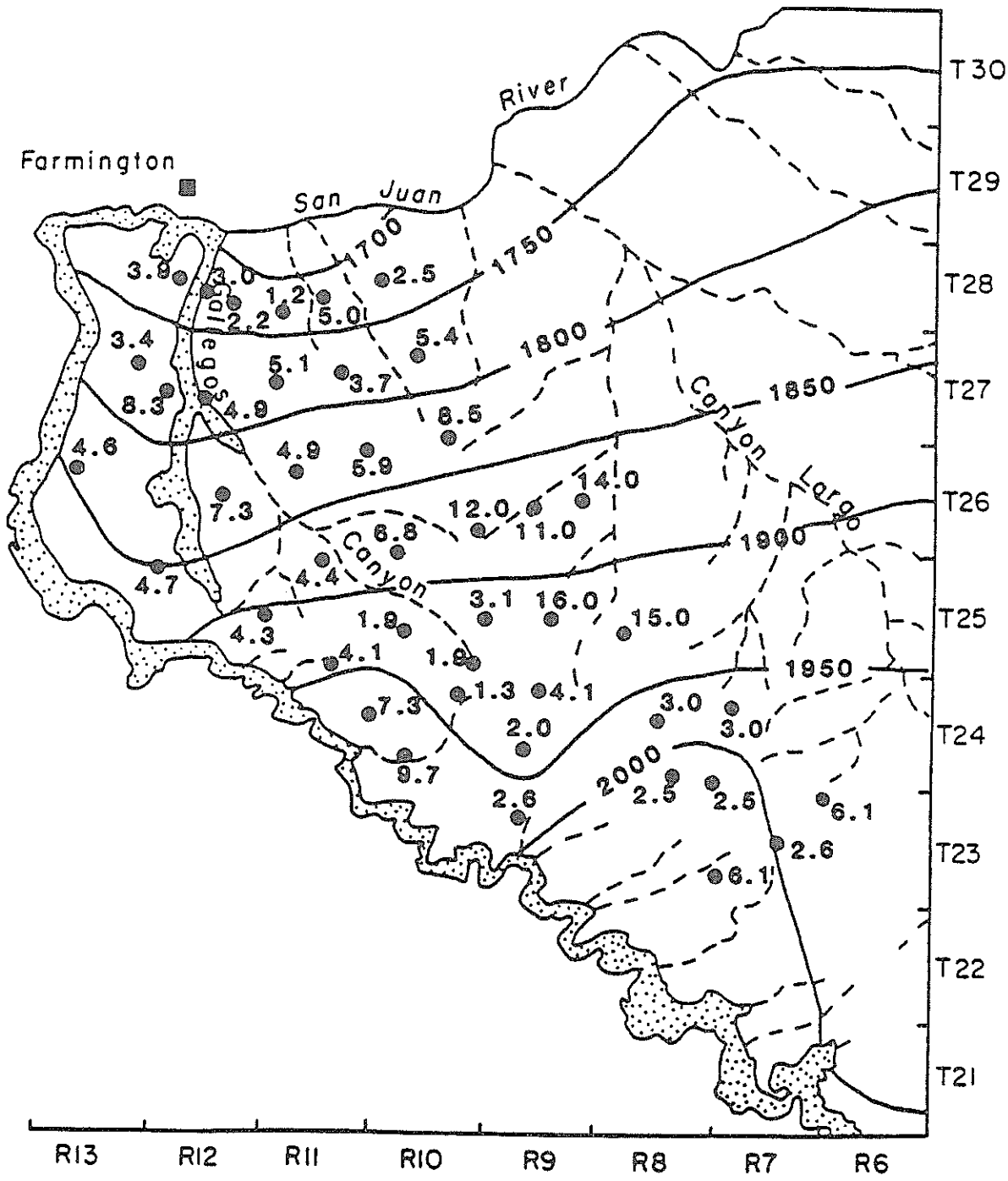

Figure 31. Ojo Alamo Hydraulic Conductivity X 10^6(m/s).

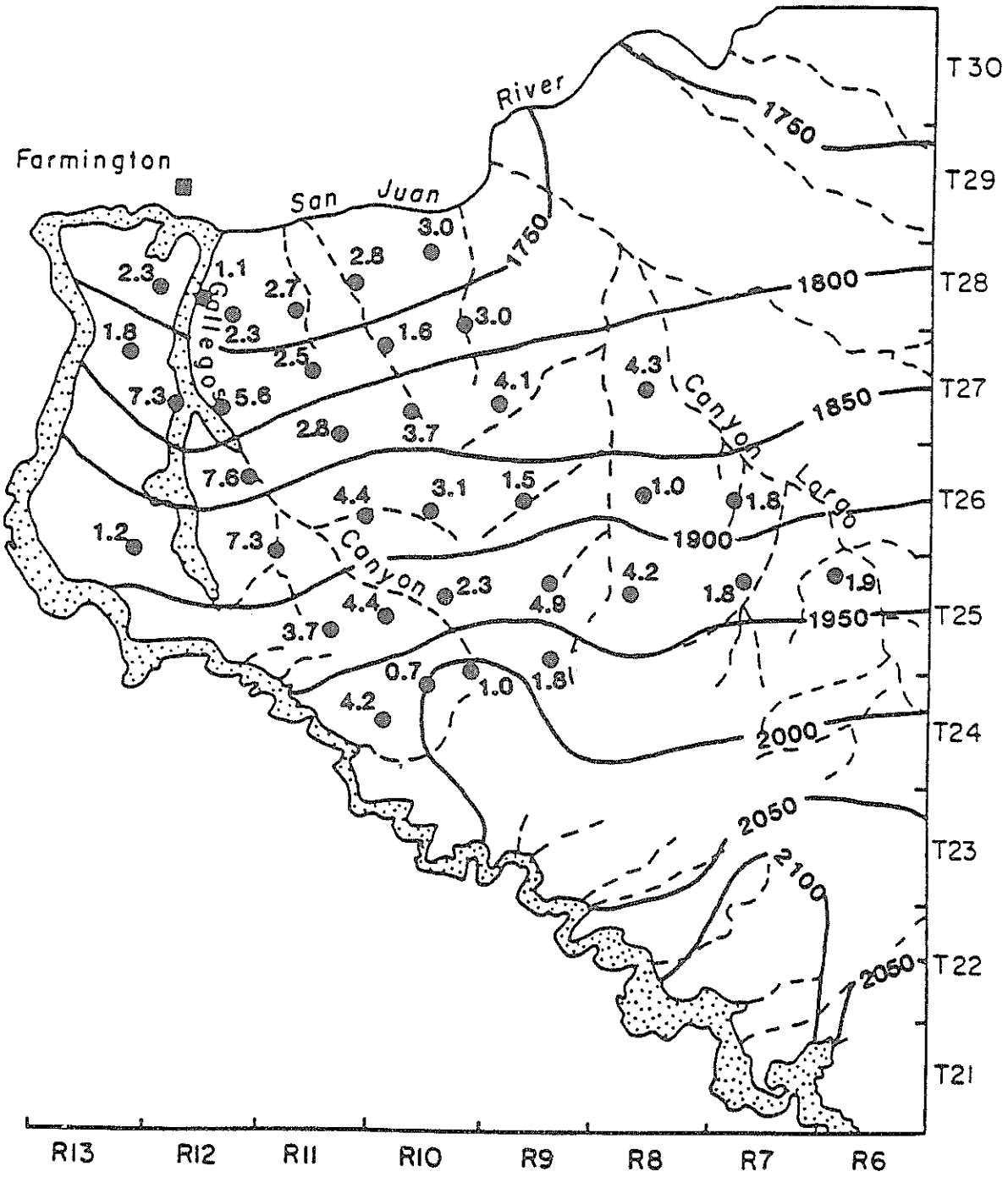

Figure 32. Nacimiento Hydraulic Conductivity X 10^6(m/s).

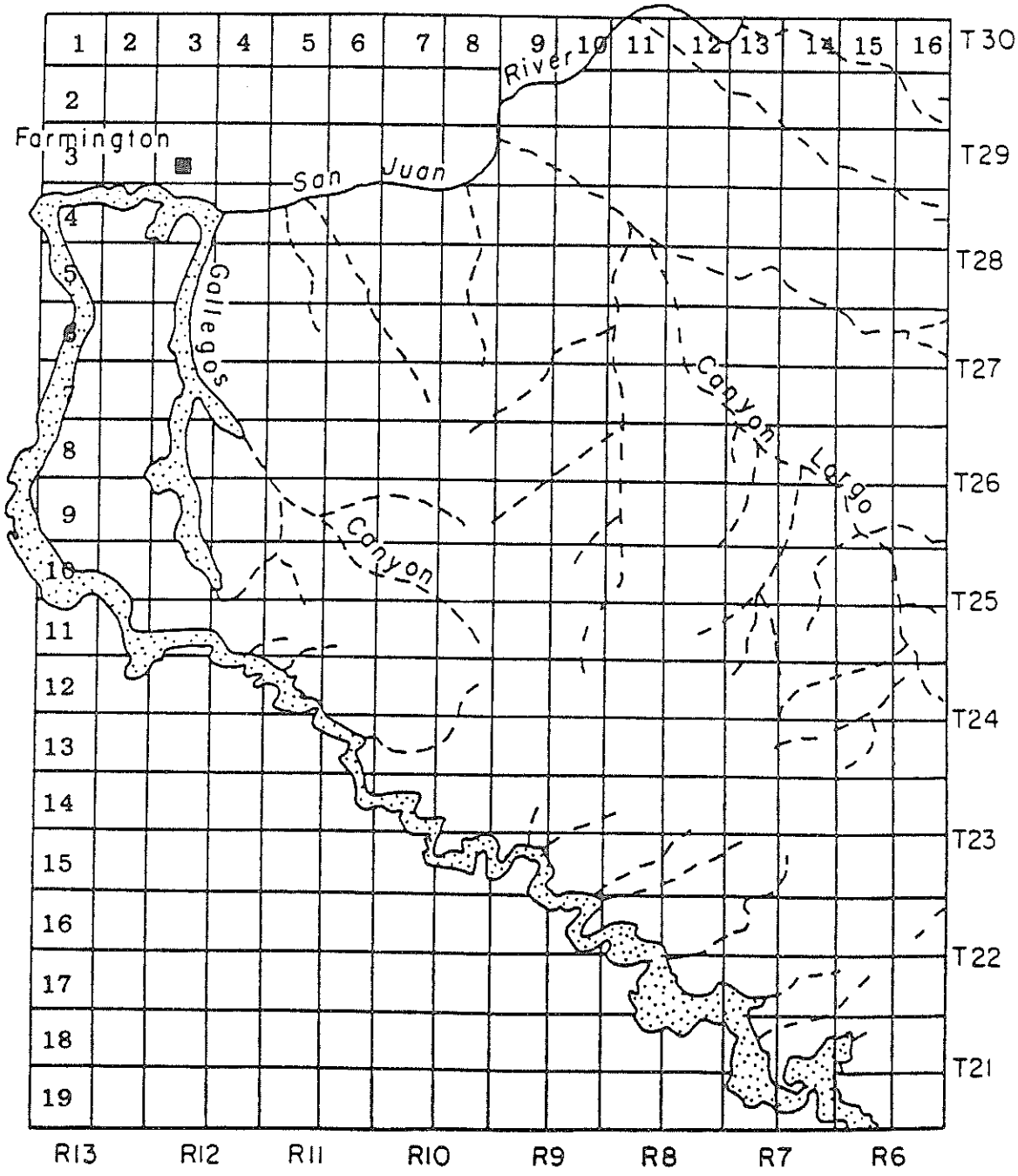

Figure 33. Location of Numerical Model Grids.

For each of the aquifers, the hydraulic conductivity at the node points was estimated from the values presented on figures 30 and 31 and the relative configuration of the potentiometric surface. To calculate the corresponding transmissivity, the thickness of the aquifers must be known. The highly stratified nature of the Nacimiento Formation complicates the determination of suitable aquifer thicknesses. Basically, there are two problems. In some areas, the basal Nacimiento sandstone zones are scarcely separated from the Ojo Alamo. From the point of view of groundwater flow, these strata should be included with the Ojo Alamo Sandstone. To resolve this problem, it was decided that basal sections of Nacimiento would be included with the Ojo Alamo when the addition did not reduce the resultant transmissivity of the underlying aquifer by greater than 50 percent. The LOGANS program was used to perform the analysis. Using the electric logs and the calibrated hydraulic conductivity estimation model, successively higher Nacimiento shale/sandstone zones were evaluated to determine their effect on the transmissivity. When the addition of a shale/sandstone zone resulted in a transmissivity reduction of greater than 50 percent, the contact of the uppermost sandstone layer with the shale/sandstone zone was considered to be the top of the Ojo Alamo aquifer. Figure 34 presents the locations and thicknesses calculated for the Ojo Alamo aquifer by this procedure. The technique proved to be only partially successful. Part of the reason is that the Ojo Alamo Sandstone is composed of two sandstone layers separated by a shale of variable thickness. In some of the cases, the addition of the upper Ojo Alamo shale/sandstone to the basal sandstone layer reduced the transmissivity below the reduction cutoff criteria. Representative values of the thickness at the numerical model node points were obtained by variogram analysis and kriging. Contours of the kriged thickness of the Ojo Alamo aquifer are shown on figure 35.

Once the thickness of the basal aquifer was established, the remaining sandstones and shales of Nacimiento had to be

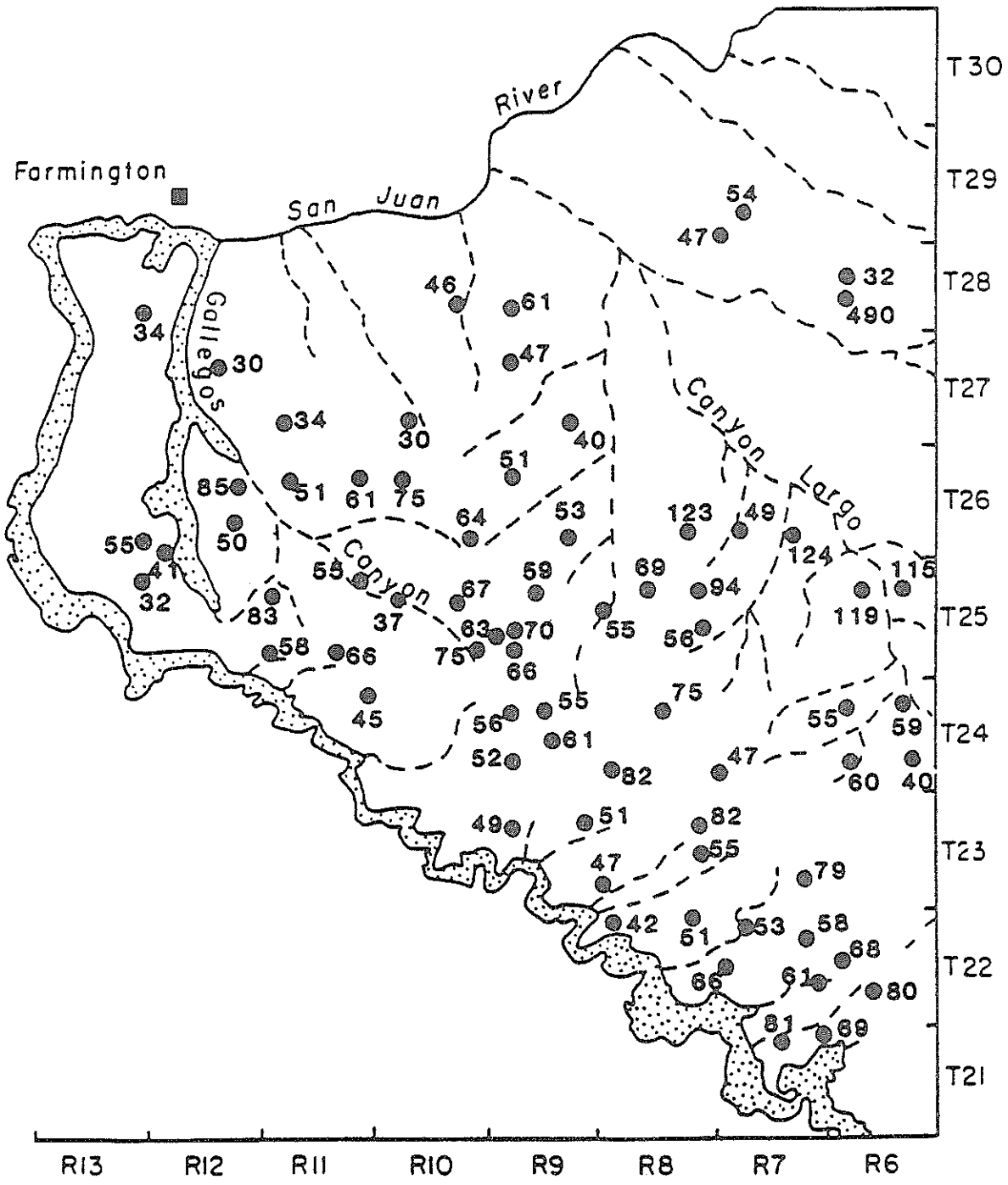

Figure 34. Thickness (m) of the Ojo Alamo Aquifer at Selected Locations.

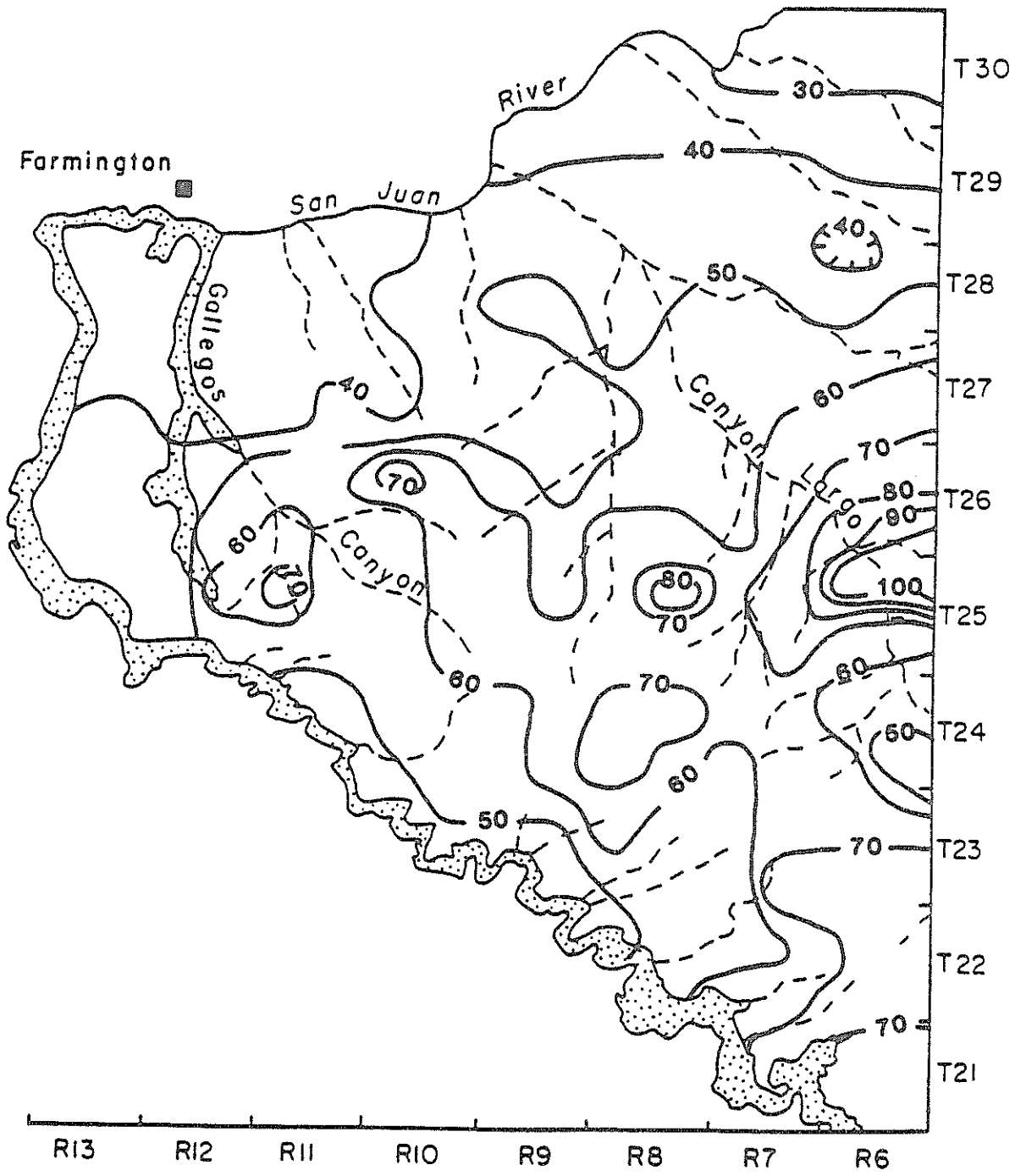

Figure 35. Isopachs of Kriged Thickness (m) in the Ojo Alamo Aquifer.

evaluated from a hydrologic perspective. For simplicity, it was decided that all the remaining Nacimiento sandstone zones would be considered as one unit located midway between the top of the Ojo Alamo aquifer and the ground surface or, when it was present, the base of the San Jose Formation. The intervening shale layers were totaled and one-half were assumed above and the other half below the Nacimiento aquifer. The LOGANS program was coded to perform these calculations. The results are presented on figures 36 and 37.

Values of the thickness of these units at the model nodes were obtained by multiple regression analysis. The Nacimiento aquifer thicknesses were calculated by performing a second order multiple regression of the thickness values. The resultant multiple regression coefficient was 0.87. Isopachs of the estimated thicknesses are presented on figure 38. The thicknesses of the Nacimiento aquitards were also estimated by a second order regression fit. The multiple regression coefficient was 0.89. Isopachs of the individual aquitard units are presented on figure 39.

Transmissivities associated with the hydraulic conductivities determined by the groundwater dating methods are shown on figures 40 and 41 for the Ojo Alamo and Nacimiento formations respectively. The thicknesses used to calculate these values were estimated from the regression analyses of thicknesses at the nodal points. For the numerical model, estimates of hydraulic conductivity and regression thicknesses at the node points were used to calculate the transmissivity.

The determination of the Kirtland-Fruitland aquitard thicknesses has already been described in the introductory geology section. Isopachs drawn from these thicknesses at the node points are presented on figure 6.

One of the main problems in quasi-three-dimensional modeling is the general lack of representative values for the hydraulic conductivity of the aquitards. The customary procedure to overcome this difficulty is to select values which result in a

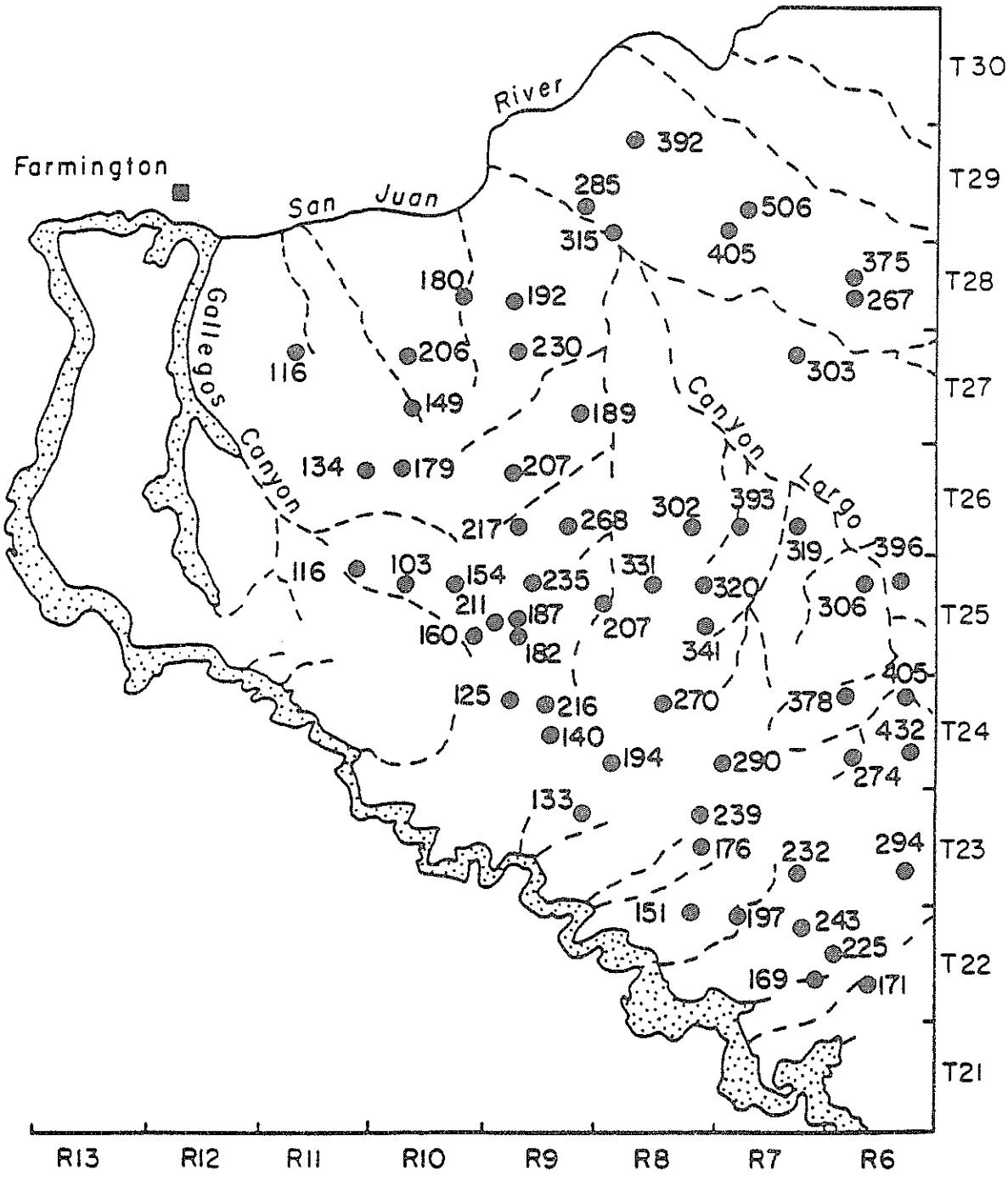

Figure 36. Thickness (m) of the Nacimiento Aquifer at Selected Locations.

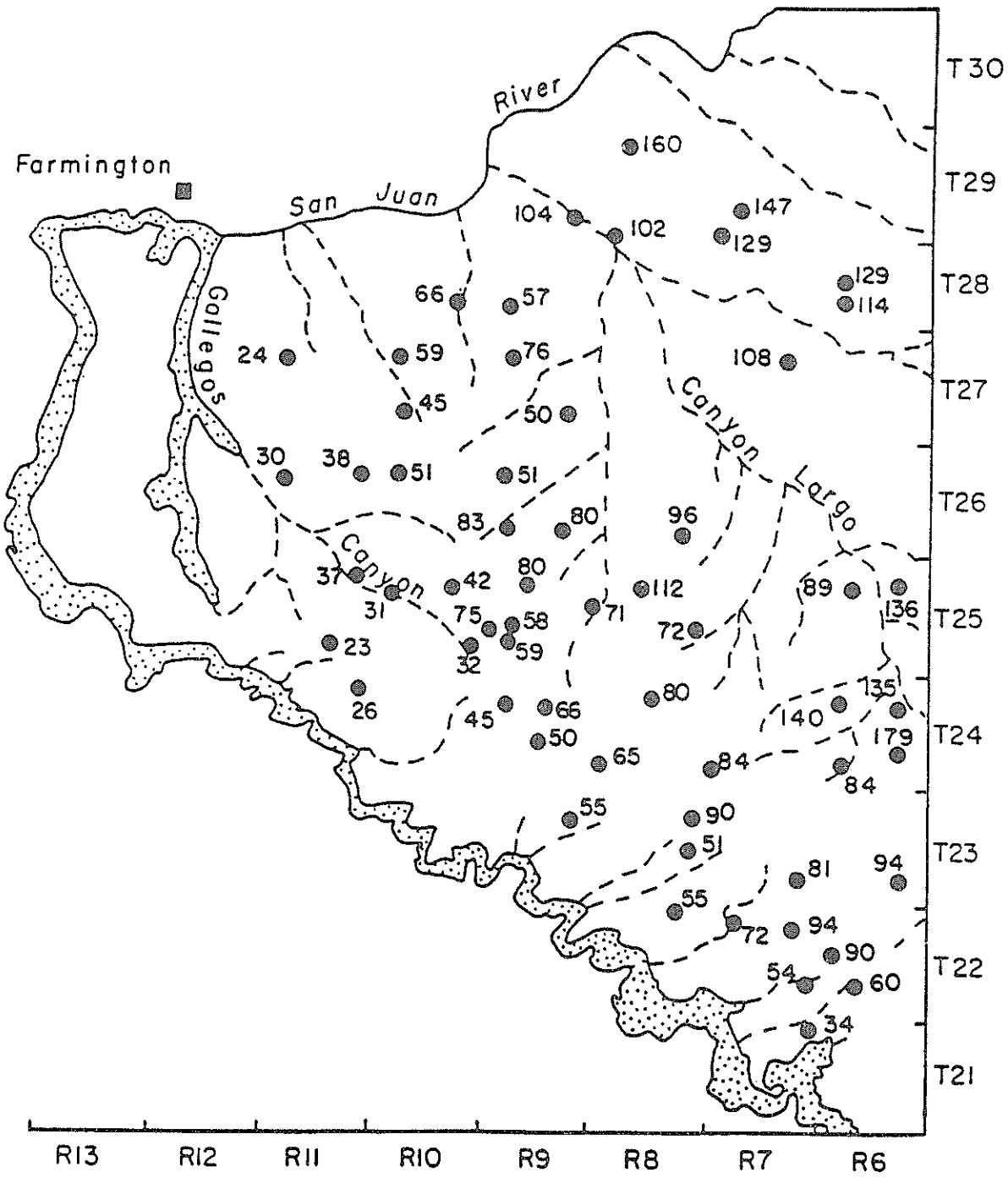

Figure 37. Thickness (m) of the Nacimiento Aquitards at Selected Location.

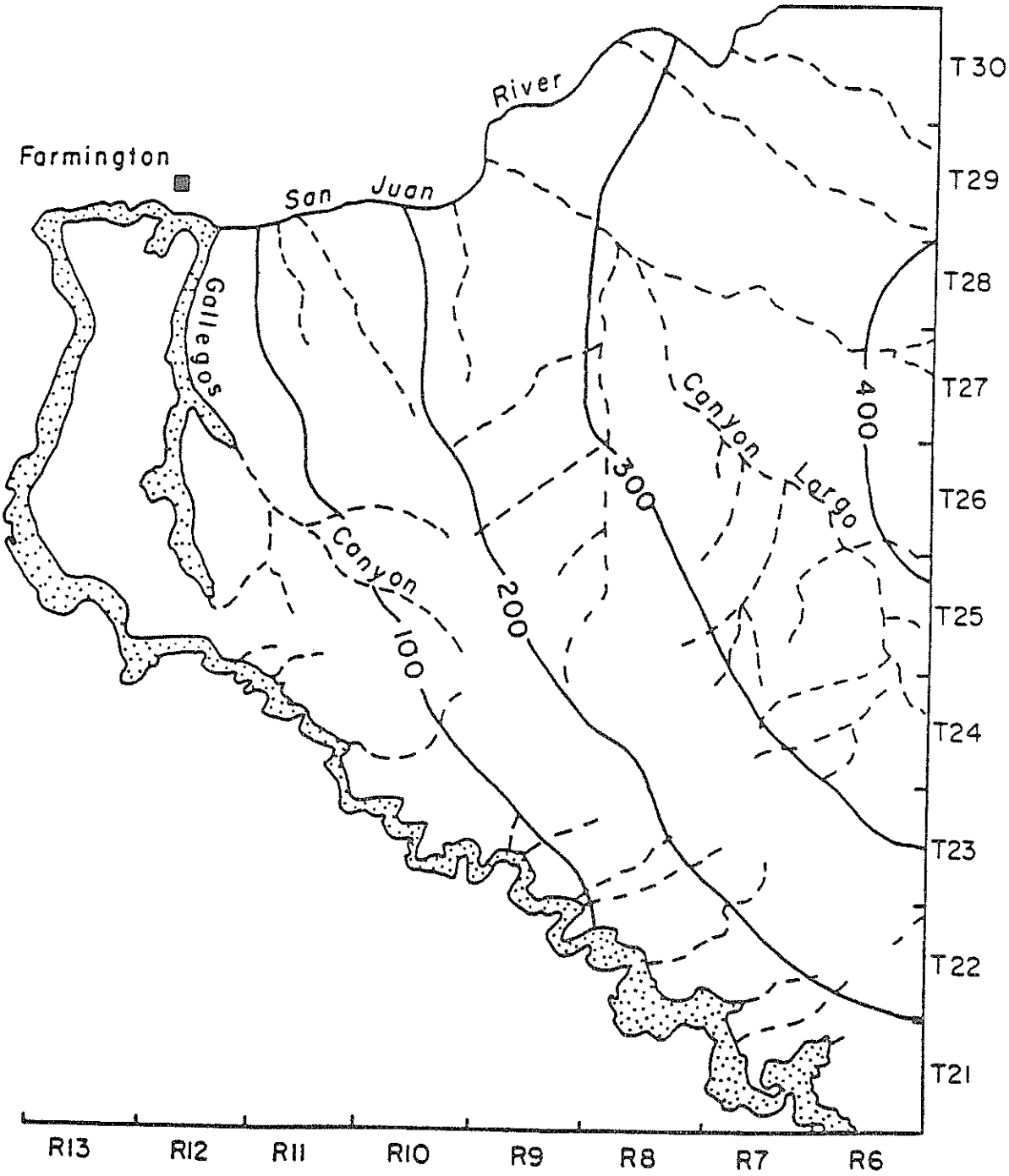

Figure 38. Isopachs (m) of the Nacimiento Aquifer.

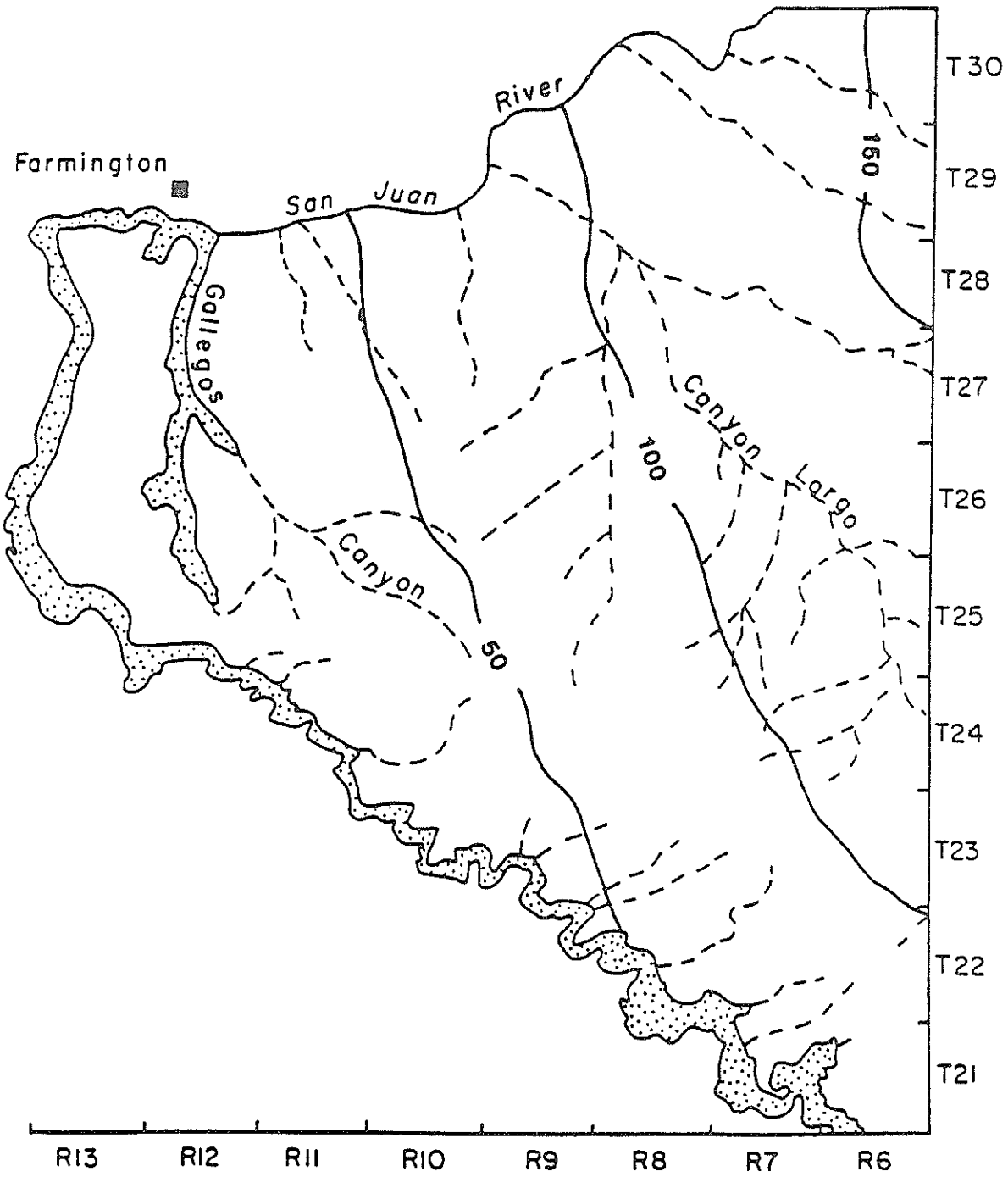

Figure 39. Isopachs (m) of the Nacimiento Aquitards.

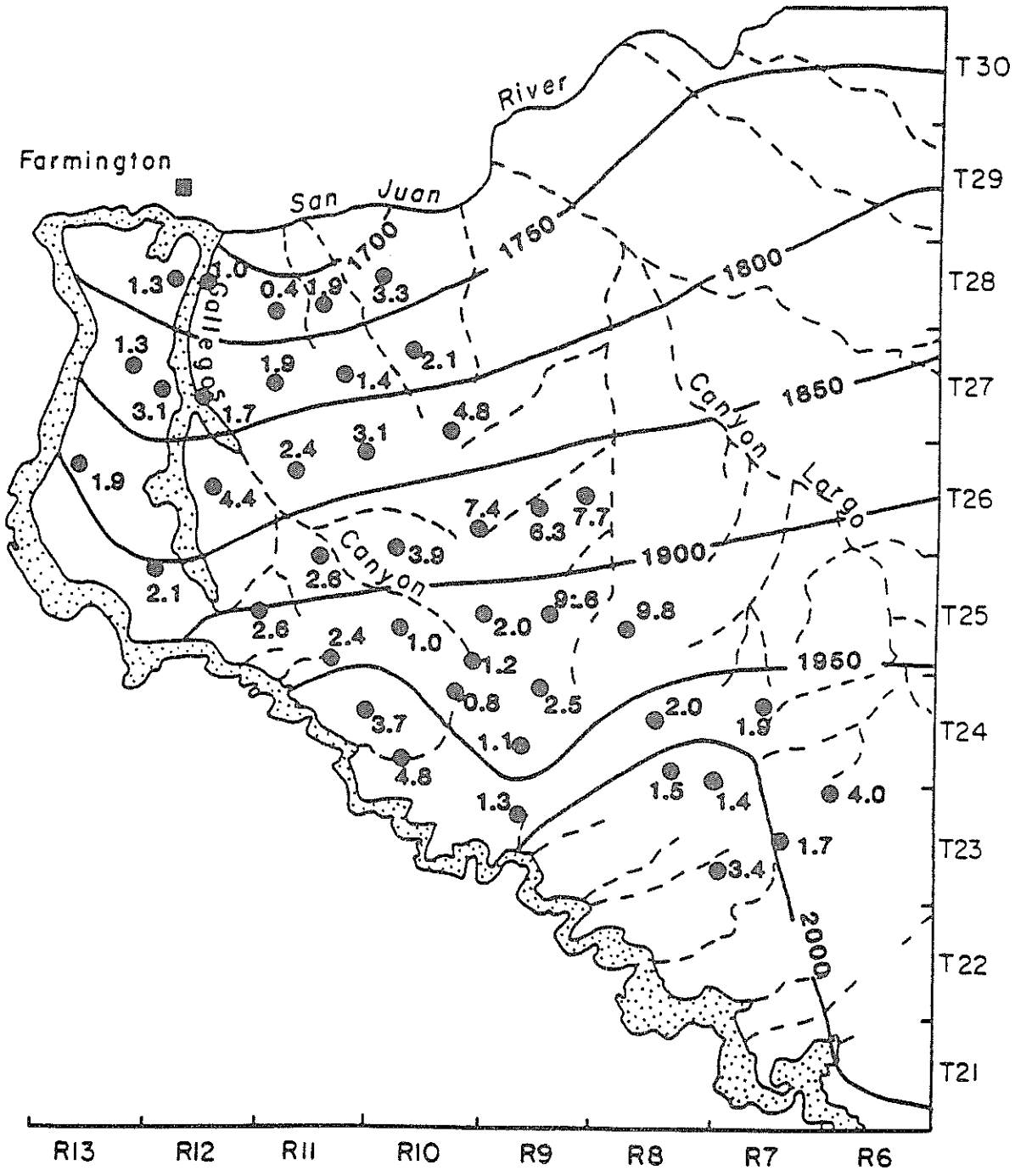

Figure 40. Transmissivity of Ojo Alamo Aquifer X $10^4(m^2/s)$.

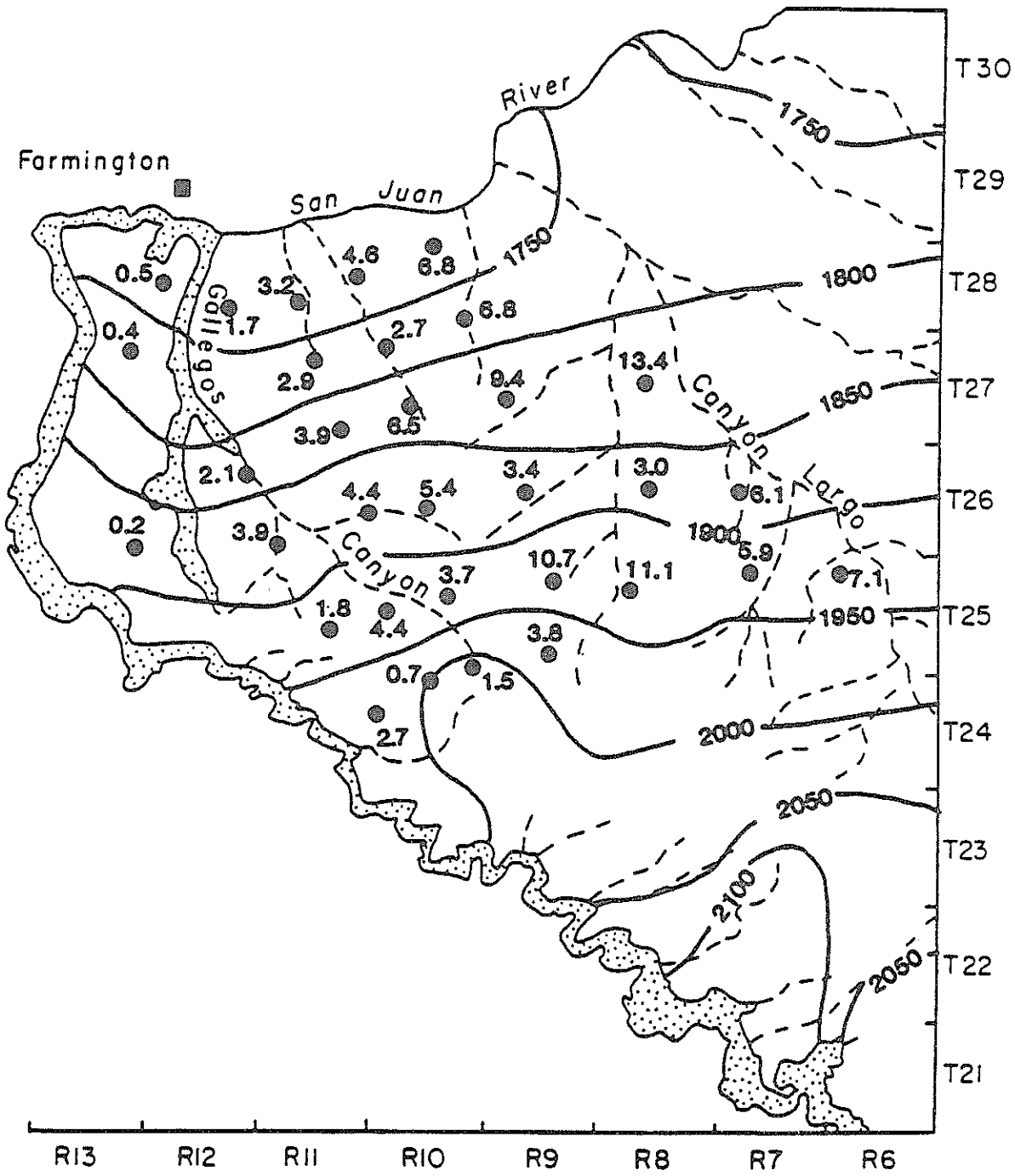

Figure 41. Transmissivity of the Nacimiento Aquifer X $10^4(m^2/s)$.

good agreement between the initial and final model-computed hydraulic heads. In this study, temperature logs, provided by Dr. Marshall Reiter of the New Mexico Bureau of Mines and Mineral Resources, were analyzed by the methods previously discussed in the theory section. This part of the study was done by Julie Maddox, a graduate research assistant at New Mexico Tech. Only seven logs were available in the study area. The results are presented in table 12.

Table 12. Aquitard Hydraulic Conductivity as Estimated from Thermal Gradients.

Profile Name	Location T	R	S	Formation Abbv.	Method: Mansure-Reiter (m/s)	Method: Bredehoeft-Papadopulos (m/s)
Angel Peak #3	27	11	20	KKF	4.6×10^{-9}	1.6×10^{-8}
Blanco #2	29	8	8	Tn	7.5×10^{-9}	2.2×10^{-9}
Gasbuggy	29	4	36	KKF	10^{-11} 1/	--
Gobernador	27	5	3	Tn	2.5×10^{-9}	8.4×10^{-9}
Jones A #9	28	8	14	Tn	3.7×10^{-8}	1.0×10^{-7}
Jones A #9	28	8	14	KKF	1.4×10^{-8}	7.2×10^{-9}
San Juan 27-4	27	4	17	KKF	1.6×10^{-8}	4.2×10^{-8}

1/ This value was determined by permeameter tests on core samples (Sokol 1970).

During the steady state calibration, the geometric mean of the thermally estimated formation conductivities was used initially in the numerical model. For the Nacimiento and Kirtland/Fruitland aquitards, these mean values were 2×10^{-8} m/s and 5×10^{-10} m/s respectively.

The hydraulic head values used in the steady state model were determined by kriging. Contours of hydraulic head at the node points are presented in Figures 9, 10, and 11 for the Ojo Alamo, Nacimiento, and the San Jose Formation respectively. Estimates of the hydraulic head in the Pictured Cliffs Sandstone were made from data presented by Berry (1959). Contours of these values are shown on figure 4.

In the steady state calibration, layer 0 was treated as a constant head boundary. This layer was used to simulate recharge/discharge of groundwater at the top of the Nacimiento Formation. In most of the modeled area, this interface was the land surface. Layer 0 was also used to simulate groundwater leakage from the aquifers to the San Juan River. This flow was modeled by using average San Juan River water levels at the appropriate nodes.

Inasmuch as determinations of groundwater recharge were not available for the study area, it was decided that simulating a small amount of recharge would be appropriate. This was accomplished by using hydraulic head values in layer 0 which were 10 feet greater than the corresponding Nacimiento values in layer 1. In those areas where the San Jose Formation overlies the Nacimiento, the kriged estimates of hydraulic head in the San Jose were used in layer 0. Along the western and southern boundaries of the study area, at the nodes representing the outcrop of the Ojo Alamo and Nacimiento, the hydraulic head in layer 0 was set to zero to preclude leakage calculations. At these nodes, recharge was simulated by the constant head boundary condition.

In the model, layers 1 and 2 represent the Nacimiento and Ojo Alamo respectively. In the steady-state calibration, the majority of boundary nodes of these formations were simulated as constant head nodes. The exceptions were those nodes below the San Juan River. As discussed previously in the introductory geology, the San Juan River drains a large semi-circular basin. Groundwater flow is, therefore, directed toward the river from both sides. This means a groundwater flow path directly under the river will be vertically upward. Such a situation implies that no flow is occurring horizontally underneath the river. By setting the transmissivity of the formations to zero in the nodes on the north side of the river, the model simulates this type of a no-flow situation. The location and types of boundary nodes used in the steady-state calibration are presented in figure 42.

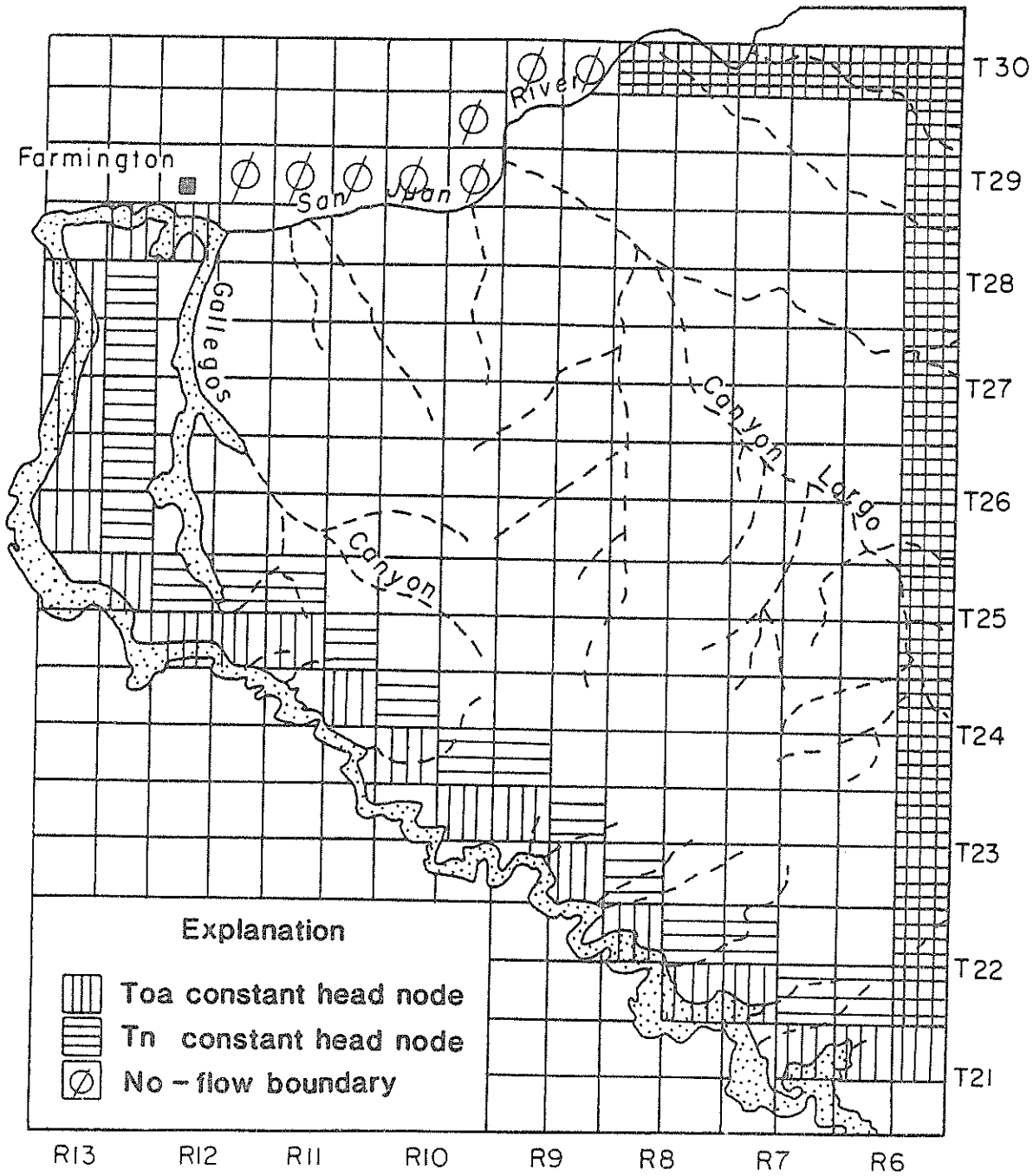

Figure 42. Location and Type of Boundary Nodes.

The Pictured Cliffs Sandstone was represented by layer 3. As stated previously, this formation was included to quantify discharge/recharge between it and the Ojo Alamo. It was, therefore, employed in the model as a constant head boundary.

Model Calibration

The steady-state calibration began with the aquifer parameters obtained by the methods described above. As expected, the computed hydraulic-head fields were not in exact agreement with the initial head fields. The specific differences will be discussed in a subsequent section. To reduce these discrepancies, adjustment of one or more of the input parameters, i.e., calibration, is required. To achieve as reliable a calibration as possible, the adjustment of parameter values should be performed by changing those parameters which are deemed the least well known. In every model, the parameter(s) to vary will be different. In this study, the hydraulic conductivity of the aquitards was the least reliably known parameter and its adjustment was used to reduce the discrepancies between the initial and computed heads. All other aquifer parameters were left as described in the text. The extent of the adjustments in the aquitard hydraulic conductivity will be discussed more fully in a subsequent section.

The purpose of calibrating a numerical groundwater flow model is to obtain agreement between the computed and the observed hydraulic heads. Attaining this goal, however, does not guar antee that the resultant model is an accurate representation of flow regime. An assessment of the validity of the parameters developed during model calibration is complex. From a fundamental perspective, knowledge of the hydraulic conductivity and thickness of the aquifers and aquitards and the correct initial and boundary conditions should generate the observed hydraulic head field. In practice, these parameters are only partly known. Also, some of the necessary hydraulic head observations may be lacking or not located at model node points. This requires that suitable estimates of the dependent variable

(hydraulic head) must be employed as substitutes for actual observed values. All of these factors result in the final calibrated groundwater model having some degree of uncertainty no matter how precisely the computed and observed hydraulic heads agree.

To obtain as realistic a model as possible, the hydrologist attempts to develop reasonable values for the parameters and boundary conditions in areas lacking such data. As the knowledge of the independent variables, boundary, and initial conditions increases, the degree of confidence in the validity of the groundwater flow model increases. In this study, transmissivities from groundwater dating and thicknesses from electric logs were considered to be the most reliable parameters. The flow regime was assumed to be at steady state due to the relatively small amount of current groundwater development. The boundary and initial conditions were not as well defined. Recharge rates were not known, so constant heads were assumed at the formation outcrops. In addition, the discharge rate of the groundwater flow system to the San Juan River has not been quantified. A possibility also exists that the flow regime is not at steady state but is responding to the transition from wetter Pleistocene to drier Holocene conditions.

Several statistical estimation techniques were used in this study to make the estimates of input parameters as reliable as possible. Kriging was used primarily to obtain estimates of hydraulic heads. Because of the sparsity and irregular spatial distribution of the available potentiometric surface data, the unbiasedness and minimized error characteristics of kriging were especially important for estimating hydraulic head values at numerical model node points. Formation thicknesses were generally determined by first or second order multiple regression techniques. Except for the Ojo Alamo aquifer, kriging was not deemed necessary because high multiple regression coefficients were obtained.

An additional benefit of kriging is that it allows one to develop some insight into the relative degree of confidence which may be associated with the flow model. As mentioned in the section on kriging theory, the kriging standard deviation (square root of the kriging variance) provides a quantitative measure of the potential error in the kriged estimates. Clearly, as the magnitude of the kriging standard deviation increases, the confidence in the flow model decreases. Figures 43, 44, and 45 present contours of the kriging standard deviation for the hydraulic head distribution in Ojo Alamo, Nacimiento, and San Jose formations. In general, the greatest uncertainty in the hydraulic heads of the Ojo Alamo and Nacimiento are in the northeastern part of the modeled area. For the San Jose, the kriging standard deviation is higher near the western edge of the formation and in the southeast. Considering the combined kriging standard deviations, confidence in the numerical model is highest to the west of Range 8 West.

The kriging standard deviation can also be used to assess the confidence to be placed in the hydrologic interpretation of inter-aquifer leakage. Based on the kriged potentiometric surfaces, figure 46 presents contours of the differences in hydraulic head between the Nacimiento and Ojo Alamo aquifers. These differences indicate that leakage is generally from the Nacimiento to the Ojo Alamo. In four areas, notable exceptions occur. In the northeastern quadrant, the hydraulic heads indicate that the Ojo Alamo is leaking vertically upward into the Nacimiento. Although this flow is hydrologically plausible, the uncertainty in the kriged hydraulic heads, as indicated by the kriging standard deviation, is so large that little confidence can be placed in this interpretation. Farther west along the San Juan River, the Ojo Alamo also appears to be discharging into the Nacimiento. From a hydrologic standpoint, this vertical leakage is quite reasonable but the kriging standard deviation is still significantly greater than the hydraulic head difference. In the northwest, Gallegos Canyon is another area

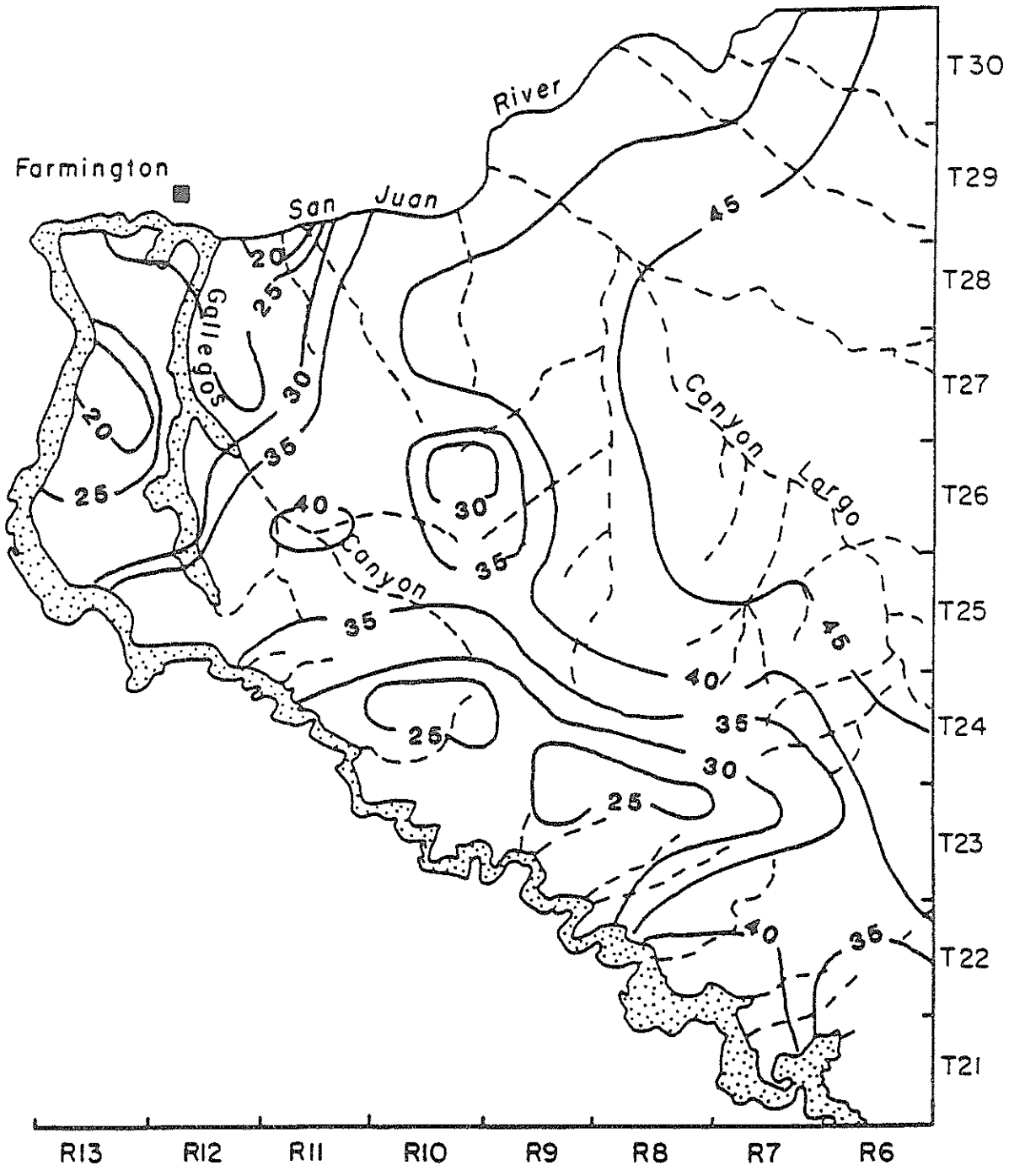

Figure 43. Contours of the Kriging Standard Deviation for the Ojo Alamo Sandstone.

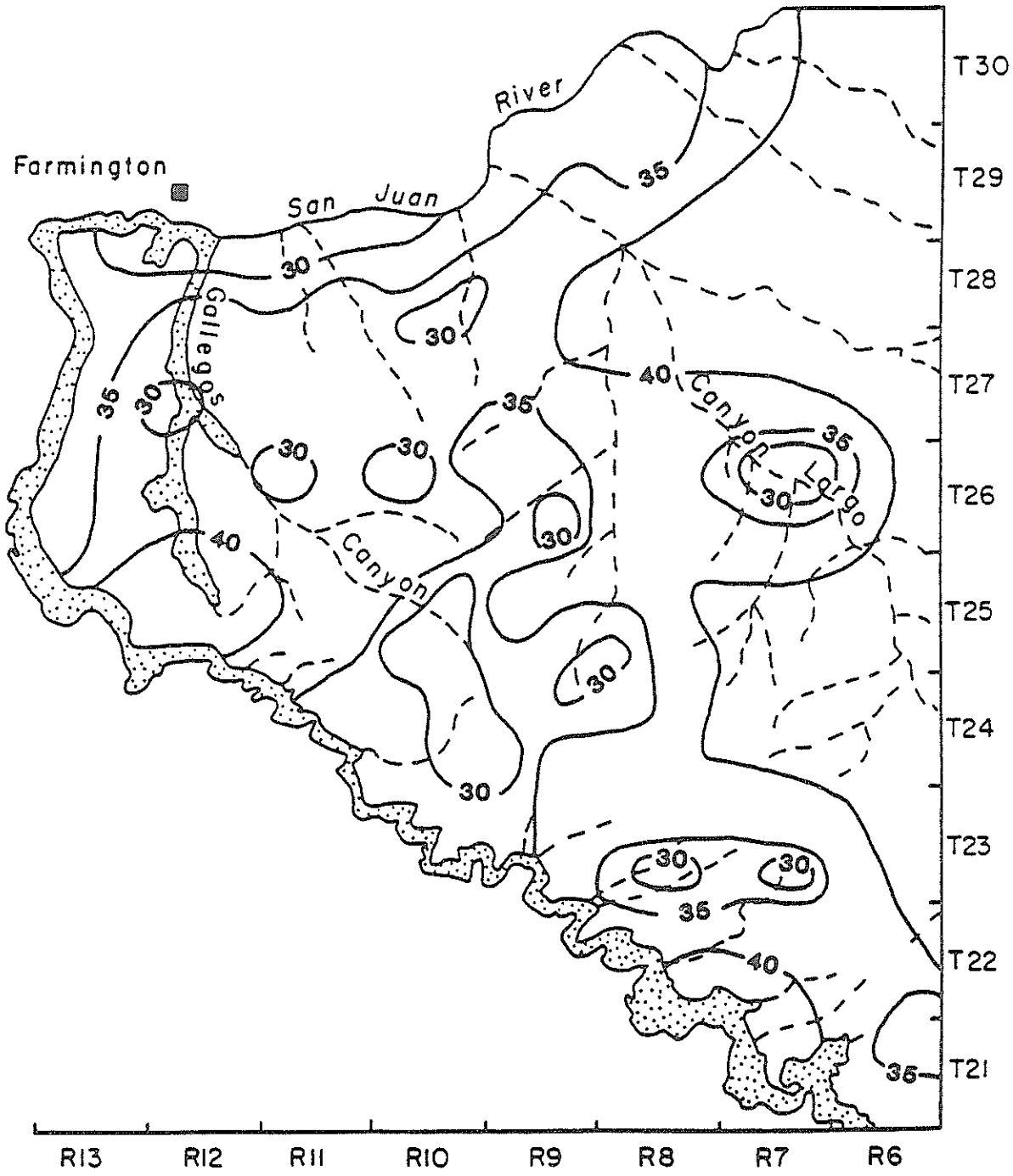

Figure 44. Contours of the Kriging Standard Deviation for the Nacimiento Formation.

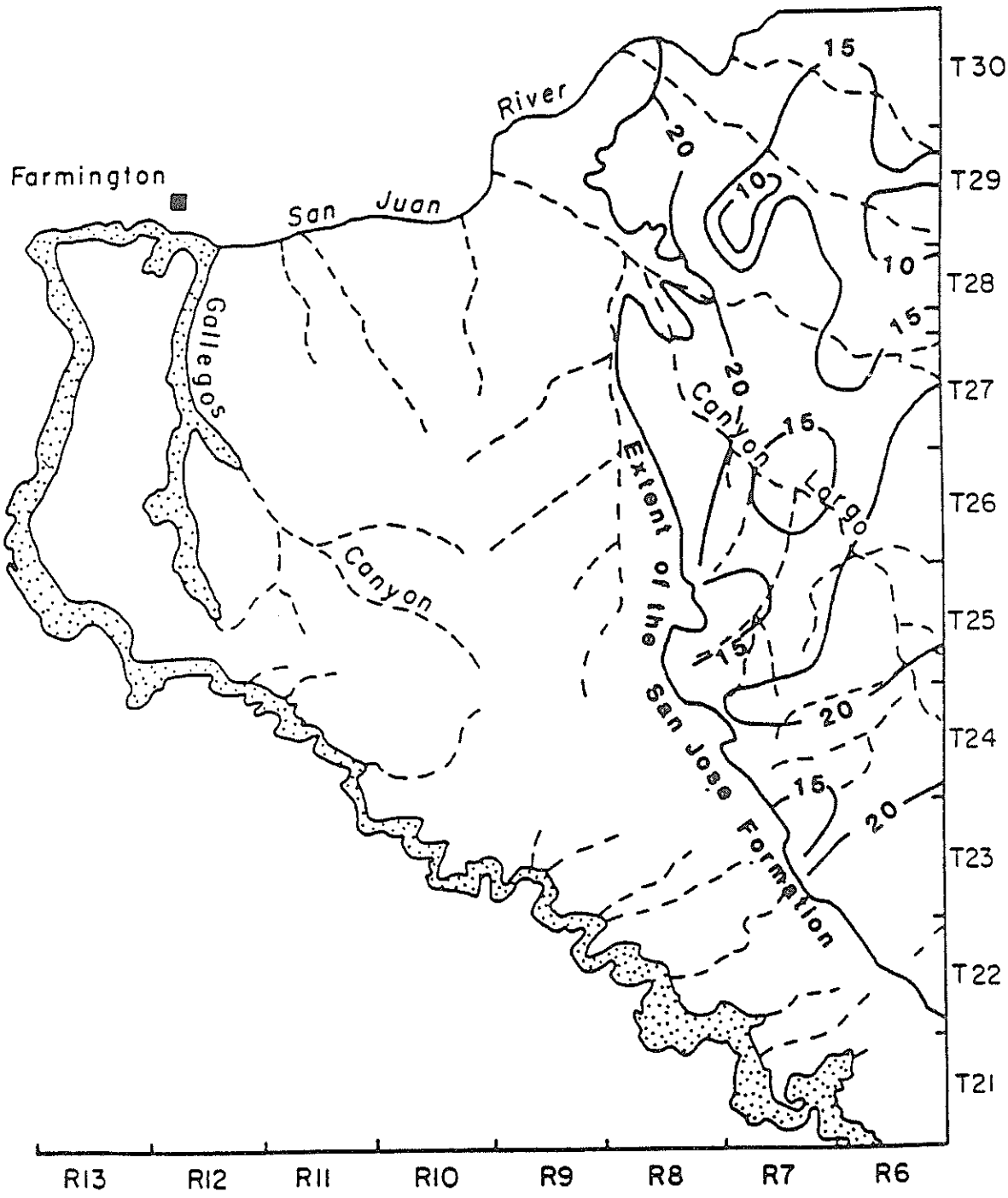

Figure 45. Contours of the Kriging Standard Deviation for the San Jose Formation.

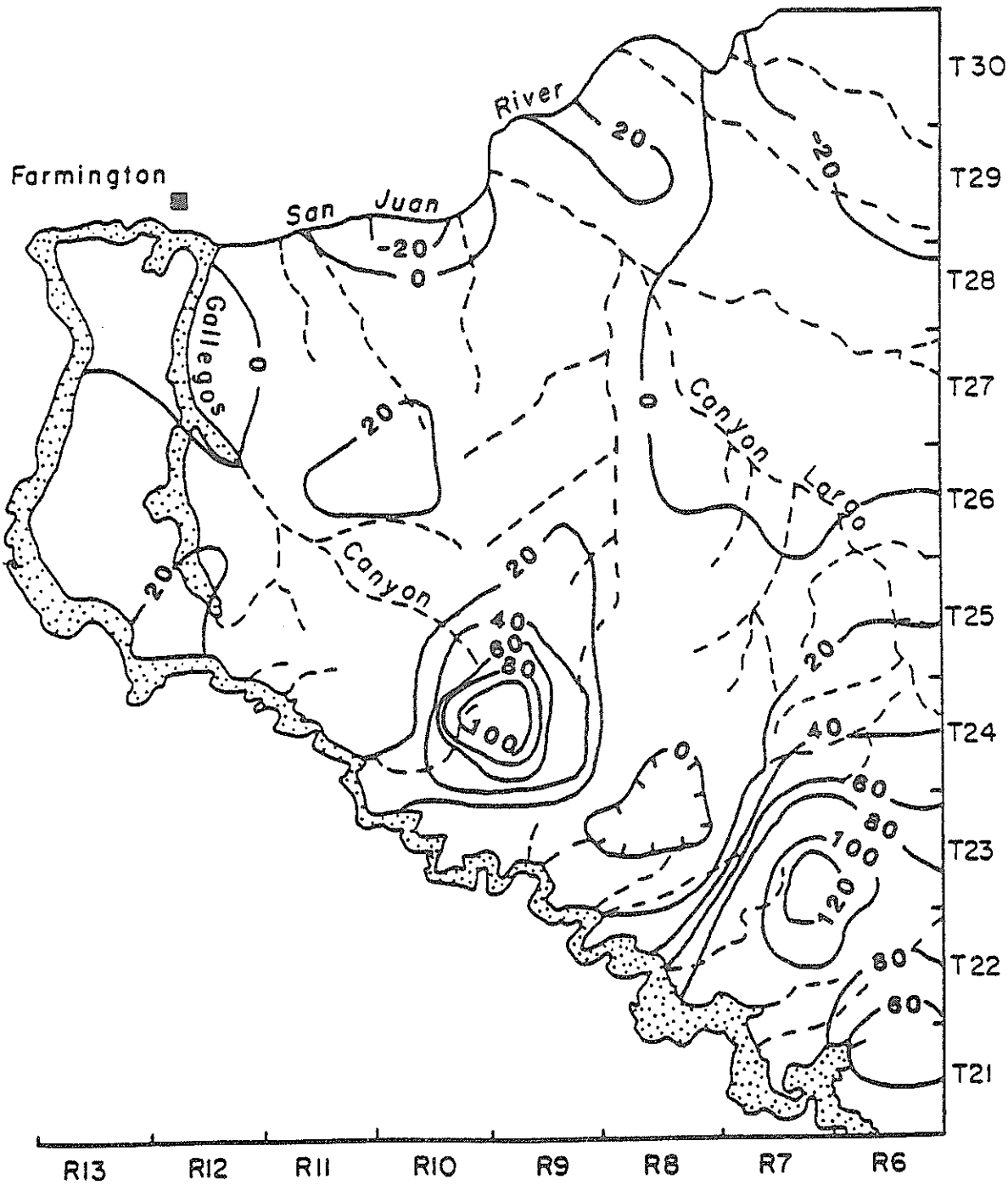

Figure 46. Hydraulic Head Differences Between the Nacimiento and Ojo Alamo Aquifers.

where the Ojo Alamo seems to be discharging upwards. In much of this area, the Nacimiento has been eroded away and replaced by more recent alluvial sediments. It is hydrologically quite likely that the Ojo Alamo discharges into these sediments. The kriging standard deviation is, however, larger than the difference between the hydraulic heads. In each of the areas discussed, the direction of groundwater flow is plausible but, due to the lack of adequate data, these hydrologic processes cannot be confirmed unequivocally.

In Townships 23 and 24 North, Range 8 West, there is a relatively small area in which the Ojo Alamo appears to be discharging into the Nacimiento. In this case, no reasonable hydrologic cause is apparent. The difference between the hydraulic heads is considerably smaller than the kriging standard deviations. It is possible that an incorrect hydraulic head observation could be responsible for the occurrence of this area of apparent upward leakage.

As stated above, this flow model was calibrated by assuming that the hydraulic conductivities calculated from the groundwater dating and the kriged potentiometric surfaces were reliable estimates. The formation thicknesses determined by multiple regression from electric log observations were also considered to be reasonably valid. Undoubtedly, both the hydraulic conductivities and thicknesses were not absolutely correct and these errors were carried over into the calculated transmissivities. In the San Juan Basin, aquifer pumping-test data is very limited. This was one of the prime reasons for using the groundwater dating technique. Figure 47 presents a comparison of several field-measured transmissivities of both the Ojo Alamo and Nacimiento formations with transmissivity values determined from groundwater dating and estimates aquifer thicknesses. Although only limited data is available, the agreement is excellent.

After the determination of values for aquifer transmissivities and formation thicknesses, the remaining parameter required

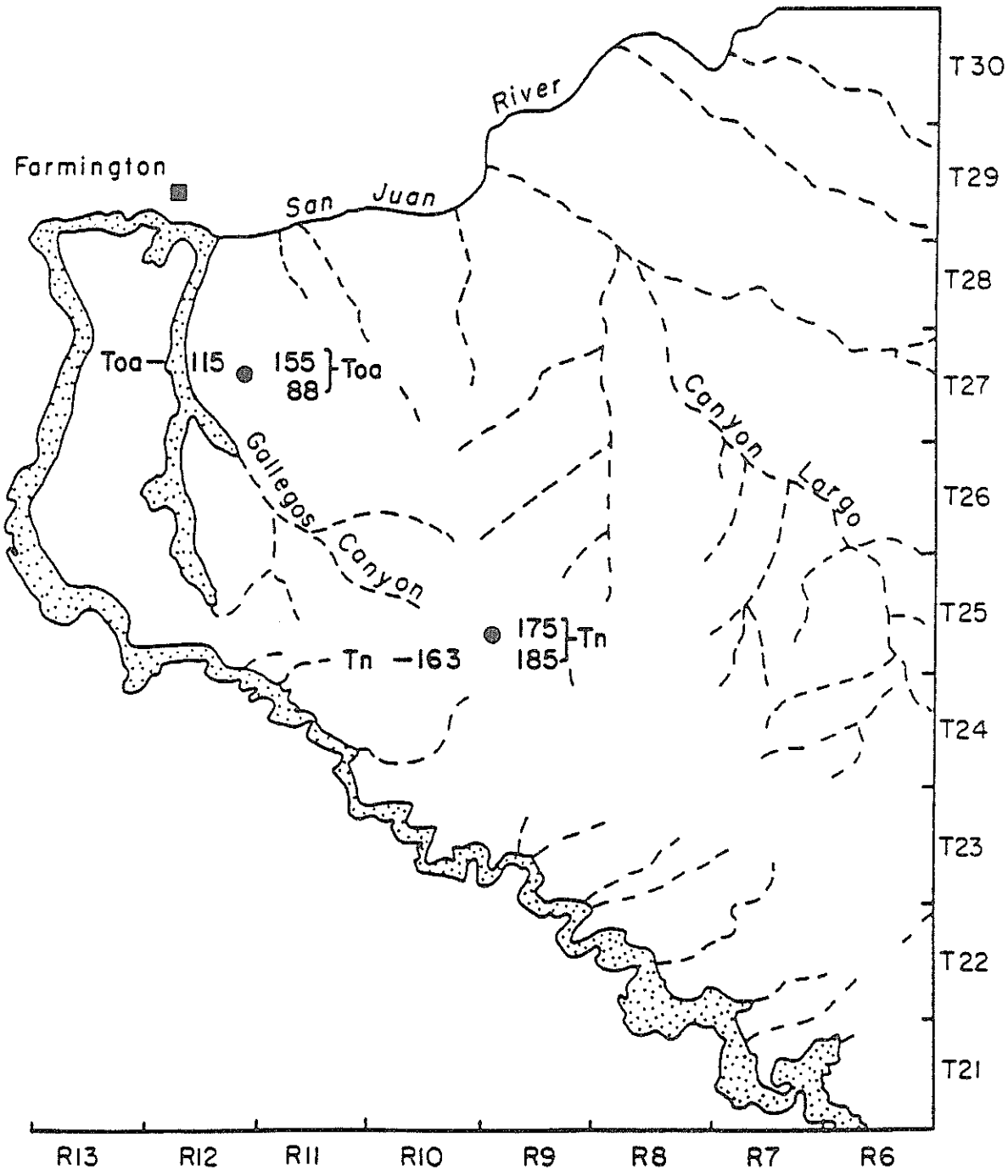

Figure 47. Comparison of Field Measured and Carbon-14 Determined Transmissivities (ft^2/day).

to define the flow field is the hydraulic conductivity of the aquitards. In this study, the previously discussed temperature gradient method of calculating aquitard hydraulic conductivity was employed. Although suitable temperature gradient data was scarce, it was hoped the values of hydraulic conductivity estimated from the available data would help to make the flow model more representative of actual field conditions. As has been mentioned previously, the aquitard hydraulic conductivities determined by the temperature gradient method turned out to be relatively high. Freeze and Cherry (1979) give values for the hydraulic conductivity of shales ranging from 1×10^{-13} to 1×10^{-9} m/s. This puts most of the values determined by the thermal technique slightly above the reported range for shales. In fact, the mean of the calculated values (1×10^{-9} m/s) is more representative of a low to medium permeability sandstone that it is of a shale. The reasons for these results are not obvious. In principle, the technique is sound. Some possible explanations are that the thermal conductivity is an experimentally difficult value to obtain; uncertainty regarding the proper values for the vertical hydraulic gradient and flow path length contribute further to errors; and finally uncertainty in the proper value for aquitard porosity compounds the problem even more.

Even though the limited number of calculated aquitard hydraulic conductivities tended to be on the high end of the shale range, the model was calibrated by altering these values as little as possible. Prior to any modification of the aquitard hydraulic conductivities, the flow model was tested at steady state. An indication of the precision of the calibration can be obtained by computing the total squared error. This is defined to be the sum of the squares of the difference between the initial (observed) and the computed hydraulic heads throughout the flow domain. Preliminary computer runs were made using uniform, mean values for the hydraulic conductivity of the

Nacimiento and Kirtland-Fruitland aquitards. For the Ojo Alamo and Nacimiento aquifers, these test runs resulted in total squared hydraulic head errors of 1.9×10^5 and 6.7×10^4 m^2, respectively. The maximum difference between the initial and computed heads that occurred during this simulation was 119 m. This value was approximately three times greater than the corresponding kriging standard deviation at the node where it occurred.

Subsequently, the aquitard hydraulic conductivities were altered at those nodes showing significant discrepancies. Since the Ojo Alamo had larger deviations, it was adjusted first. Generally, several runs with different uniform aquitard hydraulic conductivities were made. The insights gained from these runs were incorporated into a new combined data set. This was further refined until the resultant hydraulic head differences were generally less than 5 m. Figures 48 and 49 presents differences between the initial and computed hydraulic heads for the Ojo Alamo and Nacimiento aquifers, respectively. The mean square error also was computed for each of the units. For the Ojo Alamo, the resultant value was 1.4×10^3 m^2 and, for the Nacimiento, the value was 1.1×10^3 m^2. The maximum difference in hydraulic head in Ojo Alamo was 12 m. The corresponding kriging standard deviation for this node was three times larger. For the Nacimiento, the maximum head difference was also 12 m and this value was approximately three times less than its corresponding kriging standard deviation. The net result of altering the aquitard hydraulic conductivities was to reduce the sum of the squares of the errors by one and two orders of magnitude respectively for the Nacimiento and Ojo Alamo aquifers.

Another indicator of correct model performance is the mass balance. This is the net difference between the inflow and the outflow. For a flow system at steady state, this difference should be zero. Although the mass balance was excellent throughout the calibration process, a slight improvement was obtained after the adjustment of the aquitard hydraulic conduc-

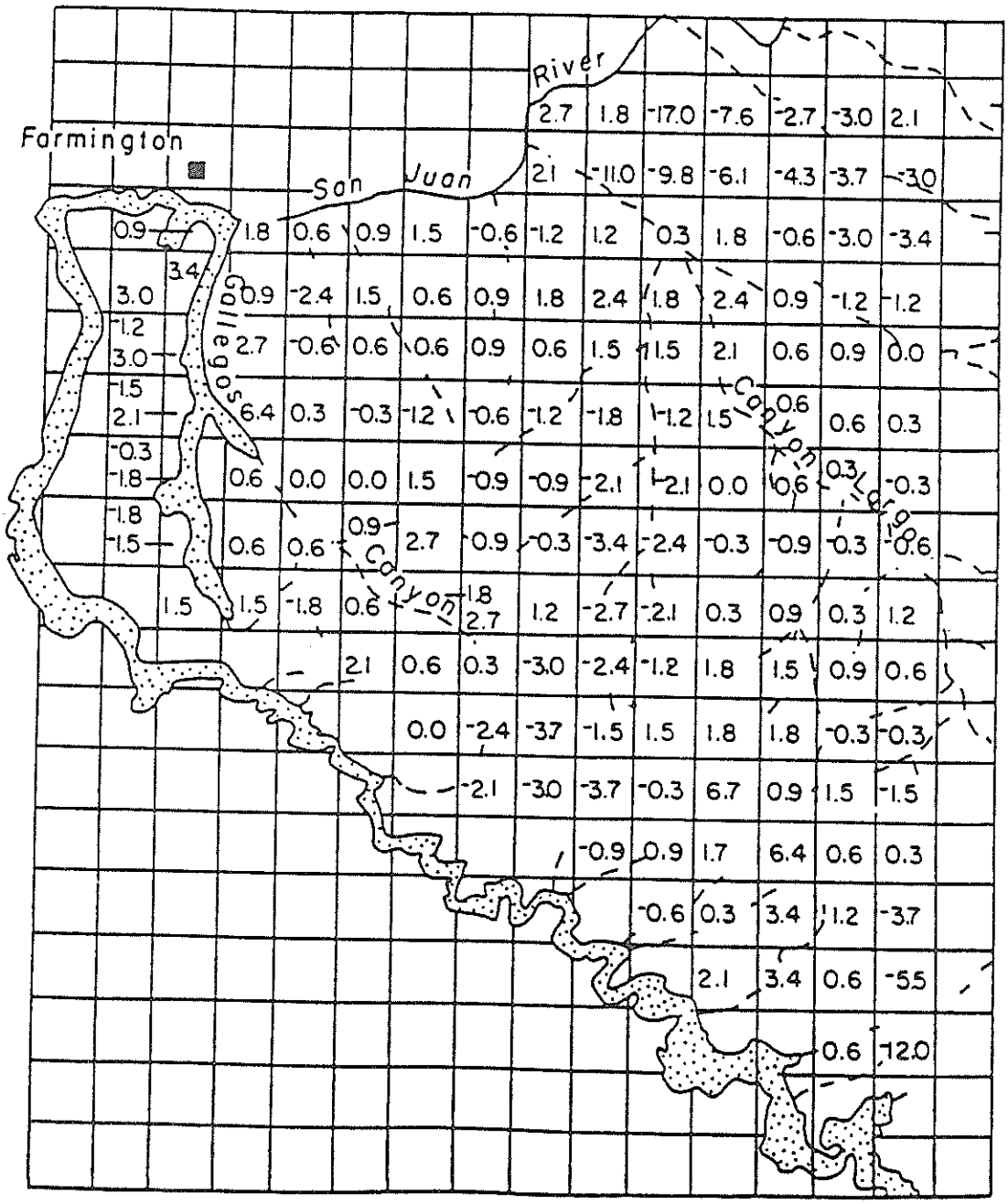

Figure 48. Differences Between Initial and Computed Heads (m) in the Ojo Alamo Aquifer.

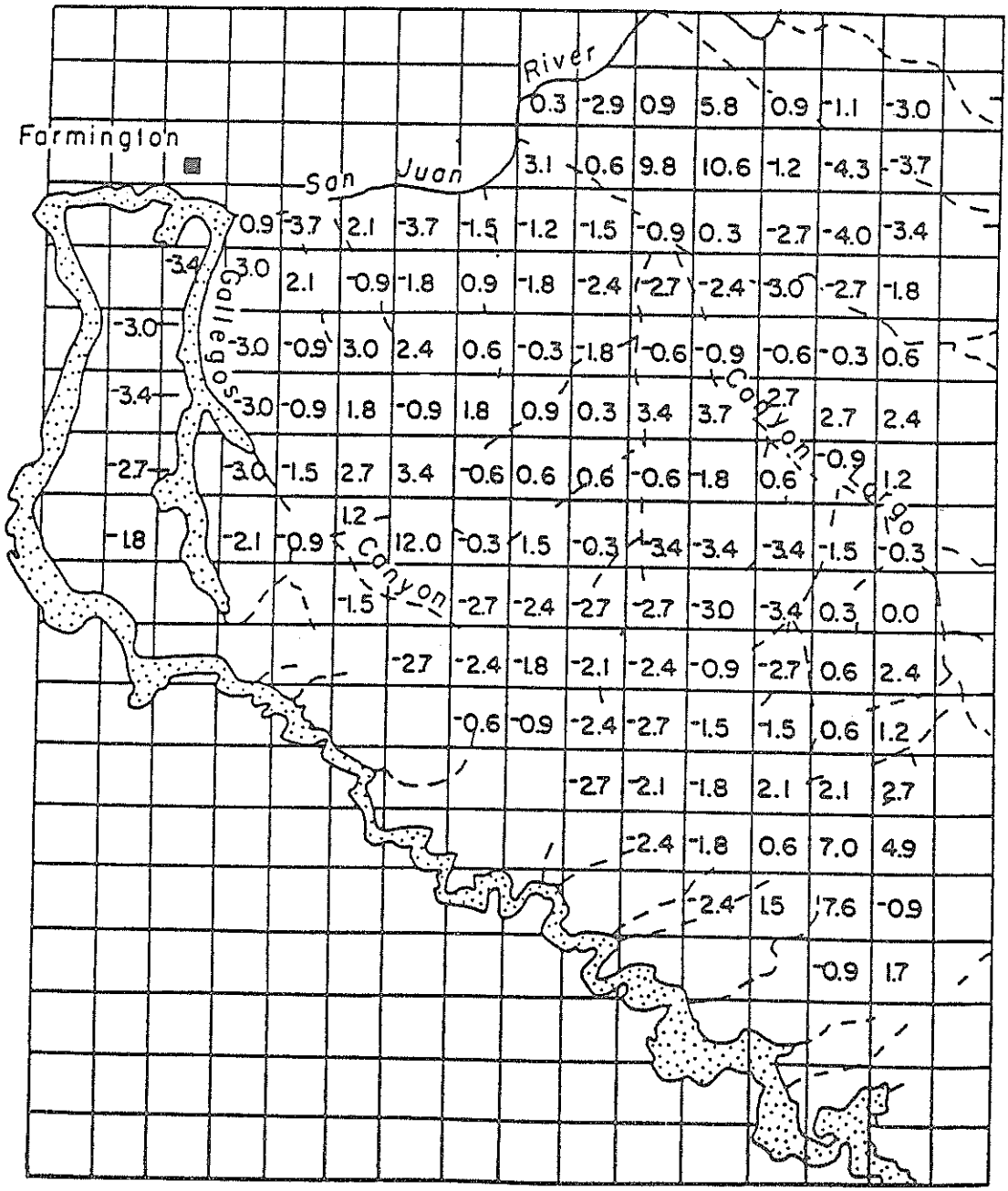

Figure 49. Differences Between the Initial and Computed Heads (m) in the Nacimiento Aquifer.

percent and is probably not statistically significant. The maximum steady state calibrated mass balance error was 0.002 percent difference in the Nacimiento. The Ojo Alamo mass balance error was even less than this amount.

Transient Simulation

After the completion of the steady state calibration, a transient simulation of a proposed well field was performed. In its application to the New Mexico State Engineer Office, Thermal Energy Resources requested the right to appropriate 24,000 acre-feet per year from 37 wells. The location of these wells is shown on figure 50. They are intended to supply water for a coal mining and gasification project to be developed in T21N, R8W, Sec. 33.

In order to perform the transient simulation, several issues had to be resolved. First, at the grid scale employed, the proposed wells could not be located exactly. Instead, they were assumed to be located at the nearest model node. Second, the rates of withdrawal from each of the formations had to be determined. This was accomplished by assuming a constant and proportionate discharge from each well so that the total annual well field discharge was correct. Since production wells are generally drilled to tap all zones, it was also assumed each well would withdraw water from both the Ojo Alamo and Nacimiento. In wells completed in more than one aquifer, it can be demonstrated that the fraction of the total discharge from each formation is approximately proportional to the ratio of their transmissivities. This ratio was employed in determining the discharge from each of the aquifers at a given well.

The transient modeling was accomplished in two phases. Prior to performing the transient simulation of the proposed well field, all of the constant head nodes, with the exception of one node in each aquifer, were converted to equivalent constant flux boundaries. The two remaining constant head nodes were located in Township 25 North, Range 12 West, at a distance sufficient to minimize their effect on the pumping wells. The

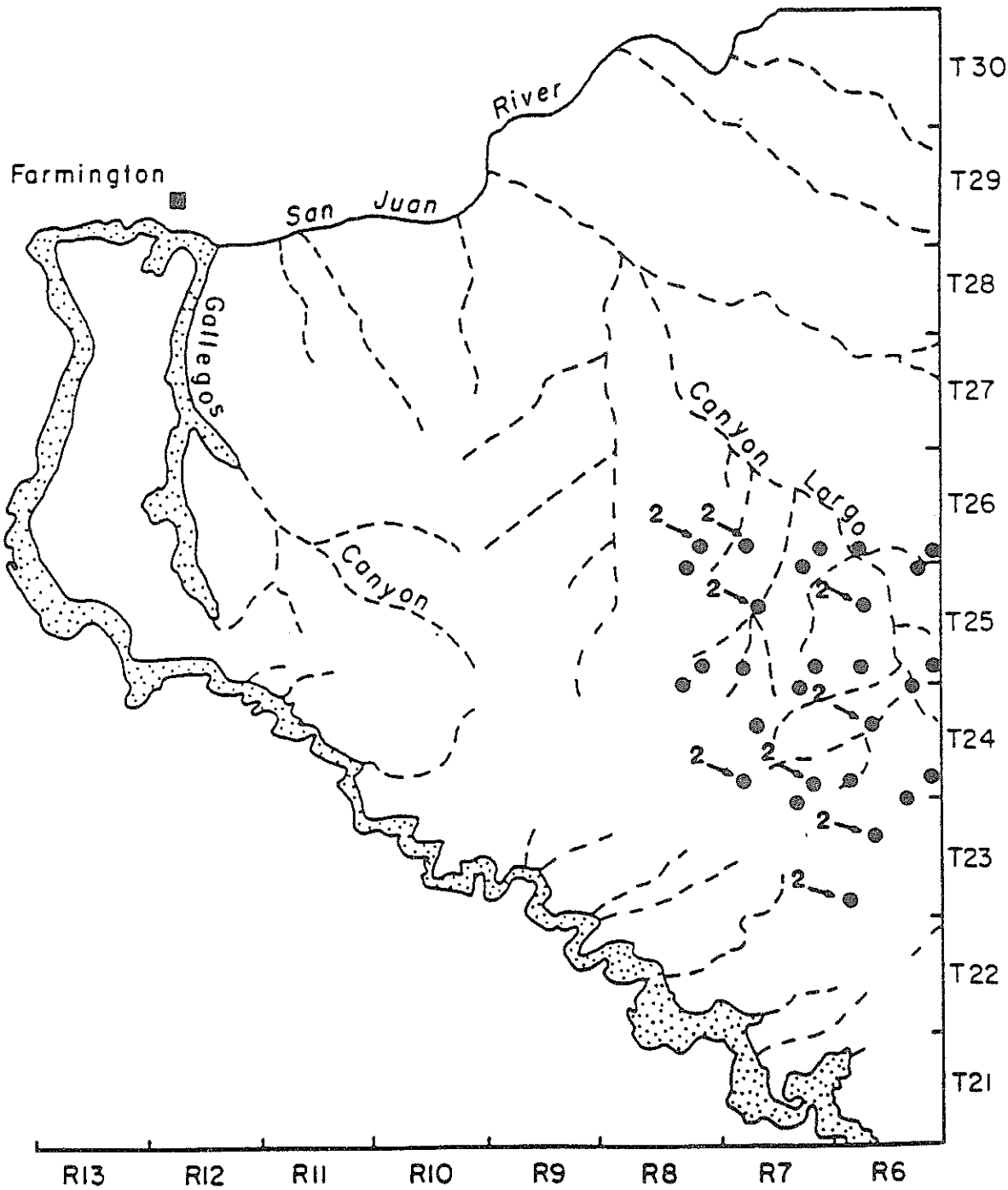

Figure 50. Location of the Proposed Well Field.

conversion from constant head to constant flux boundaries resulted in changes in the computed heads at some of the interior nodes. The majority of these altered nodes were located near the flow model boundaries. Some of the proposed wells were located in boundary nodes. This presented a special problem. The computer code was not designed to calculate interlayer leakages at constant head nodes and, therefore, the vertical fluxes at these boundary nodes were not actually accounted for in the steady state calibration. This discrepancy was overcome by a slight re-calibration of these nodes to improve the agreement between the initial and computed hydraulic head fields. In general, the amount of adjustment was not large. After re-calibration, the sum of squares of the errors was calculated for each of the aquifers. For the Ojo Alamo, the resultant value was 2.5×10^3 m^2 and, for the Nacimiento, the value was 1.4×10^3 m^2. Comparison of the constant head and flux calibrations indicates that, for the Nacimiento, the two calibrations are essentially the same. The constant flux calibration of Ojo Alamo is somewhat poorer than the constant head calibration. The maximum difference between the initial and computed hydraulic heads was 30 m. This occurred at a node located in the extreme northeastern corner of the study area. In the vicinity of the well field and, in fact, throughout most of the flow domain the deviations were less than 5 m.

A transient simulation without pumping was performed to determine if the computed hydraulic heads were constant over time. Although some slight variations (≤ 0.1 m) were observed, the values were found to be essentially invariant over the 20-year simulation time. This run was also used to obtain hydraulic-head values at various times which were unaffected by pumping for comparison with subsequent pumping results. With the constant flux-boundaries, the flow-model mass-balance errors also changed slightly. The mass balance of the Nacimiento improved very slightly. The Ojo Alamo mass balance error deteriorated slightly to approximately 1.3 percent difference.

The transient simulation also required that suitable values for aquifer storativity be employed. Only limited information concerning appropriate values was obtainable. Stone et al. (1983) reported several values. Since not enough data was available to represent spatial variations, it was decided to use a uniform storativity of 5×10^{-4}. This is the approximate mean of the reported values.

The second phase of transient modeling incorporated the effects of well field pumping at five-year intervals for the Ojo Alamo and the Nacimiento aquifers. Contours of drawdown in the Ojo Alamo and Nacimiento are presented in figures 51 to 56. The results of the 20-year simulation indicate that significant drawdowns would occur in both of these aquifers. The magnitude of the effects is greatest in the vicinity of the well field with the Ojo Alamo being slightly more affected by the pumping than is the Nacimiento. Although the cone of depression continues to enlarge over time, significant drawdown in the vicinity of the well field results after a pumping period of only five years. In general, the main area influenced by drawdown remains relatively constant throughout the entire 20-year simulation. This area of major drawdown ($\geq$ 20 m) is bounded by Township 29 to the north, Range 8 to the west, and the formation outcrops to the south. The location of the eastern edge of the 20 meter contour is outside the boundary of this study.

As the figures indicate, drawdowns ranging from 0.1 to 10 m occur throughout the majority of the remaining flow domain. After 20 years of pumping, the flow model predicts that drawdowns in both the Ojo Alamo and Nacimiento will reach 10 m in the vicinity of the Navajo Reservoir. Drawdowns in these formations decrease to the west along the San Juan River. Table 13 reports groundwater inflows to the San Juan River as predicted by the numerical flow model. At present, no independent estimates of groundwater inflow of sufficient accuracy are available for comparison. The table presents calculations of the possible groundwater fluxes between the San Juan River and the Nacimiento

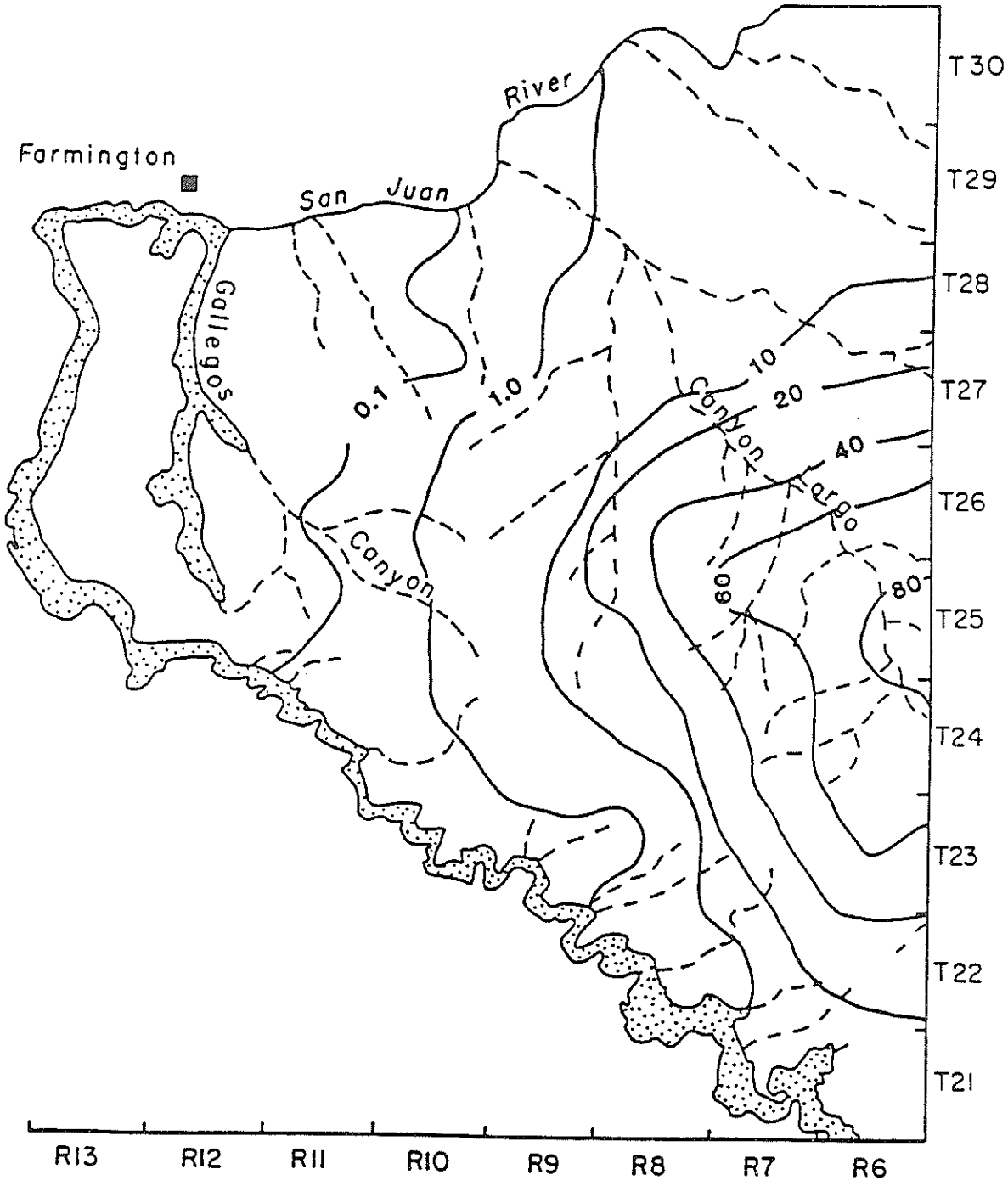

Figure 51. Drawdown (m) in the Ojo Alamo Aquifer After 5 Years of Pumping.

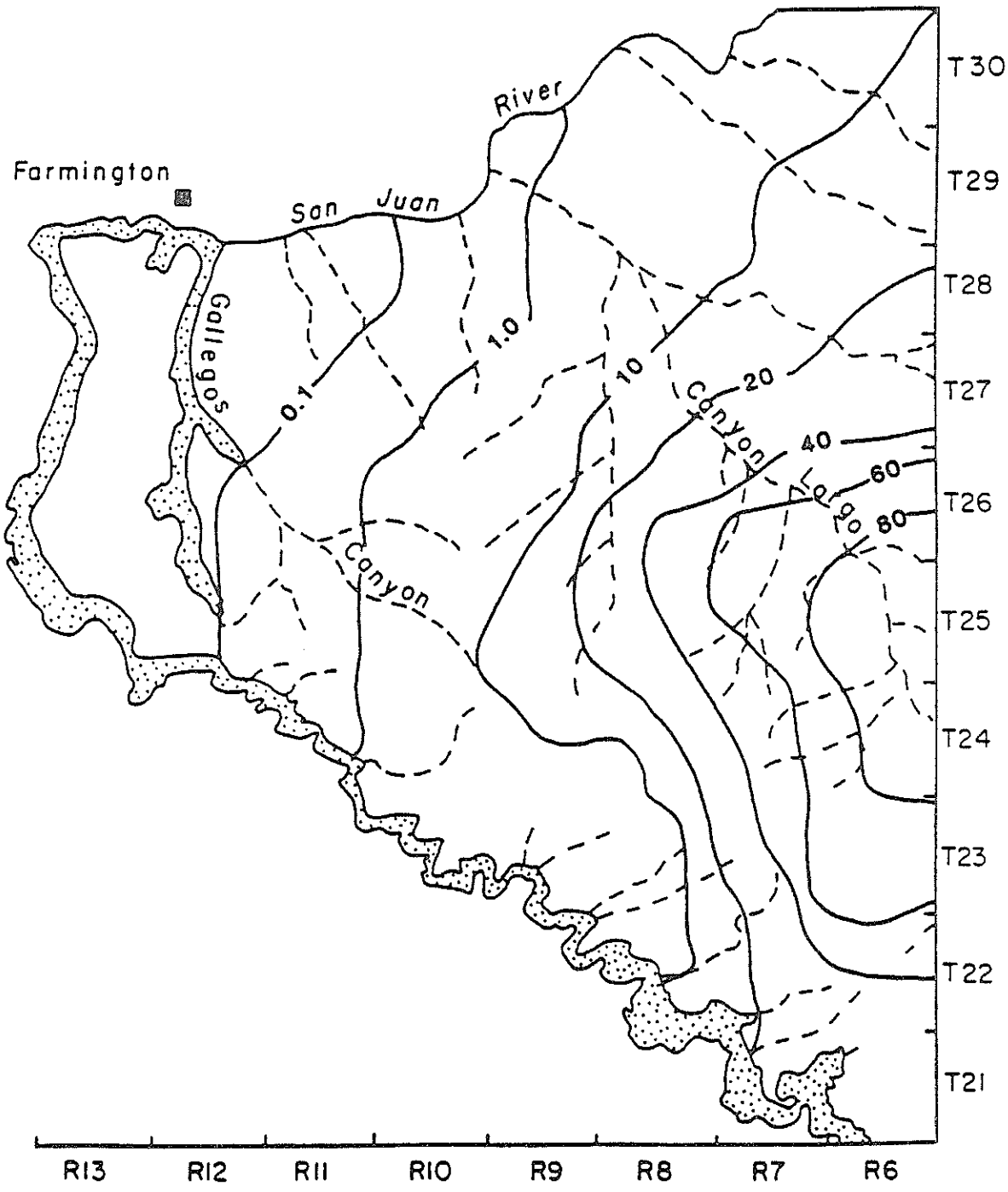

Figure 52. Drawdown (m) in the Ojo Alamo Aquifer After 10 Years of Pumping.

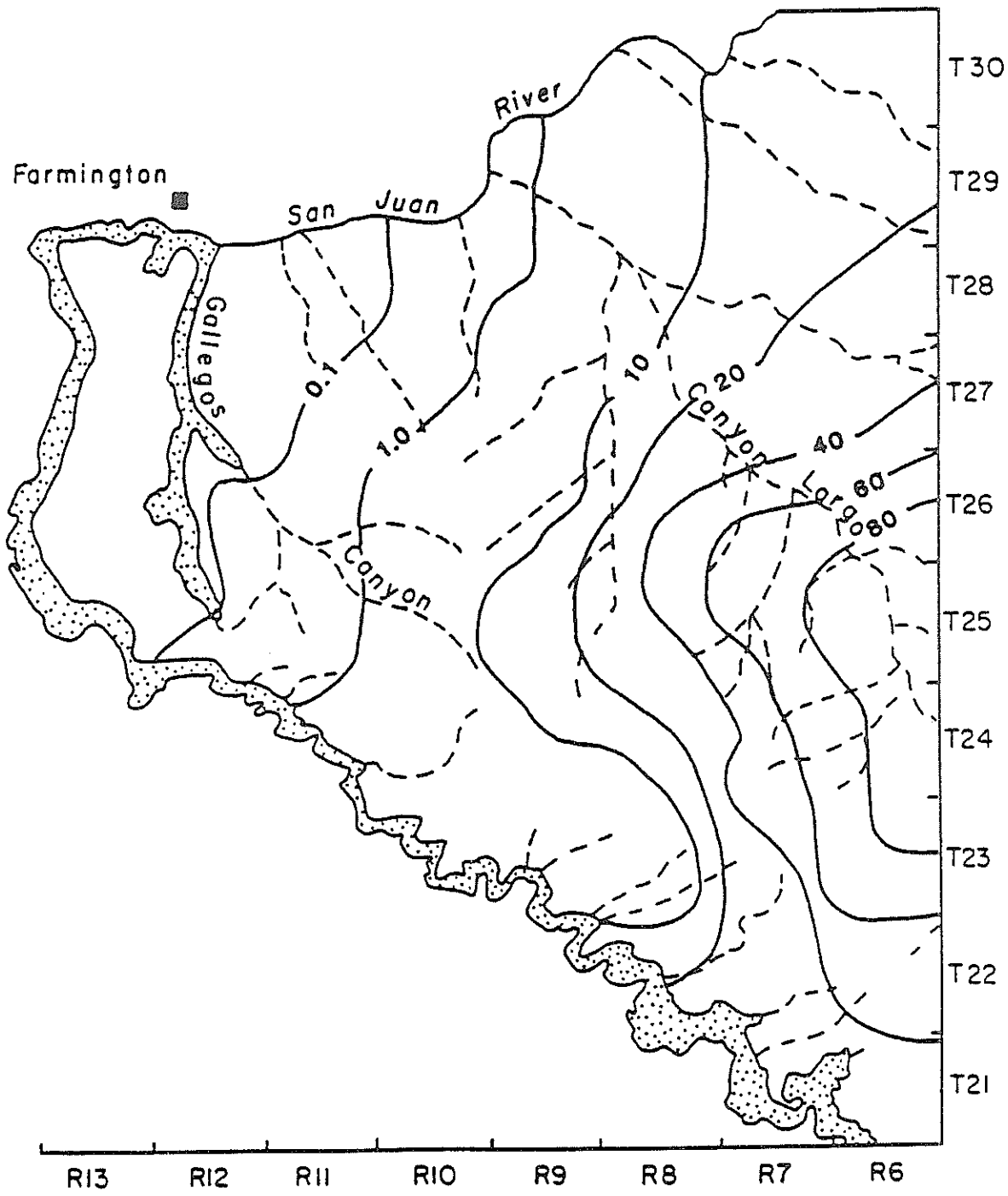

Figure 53. Drawdown (m) in the Ojo Alamo Aquifer After 20 Years of Pumping.

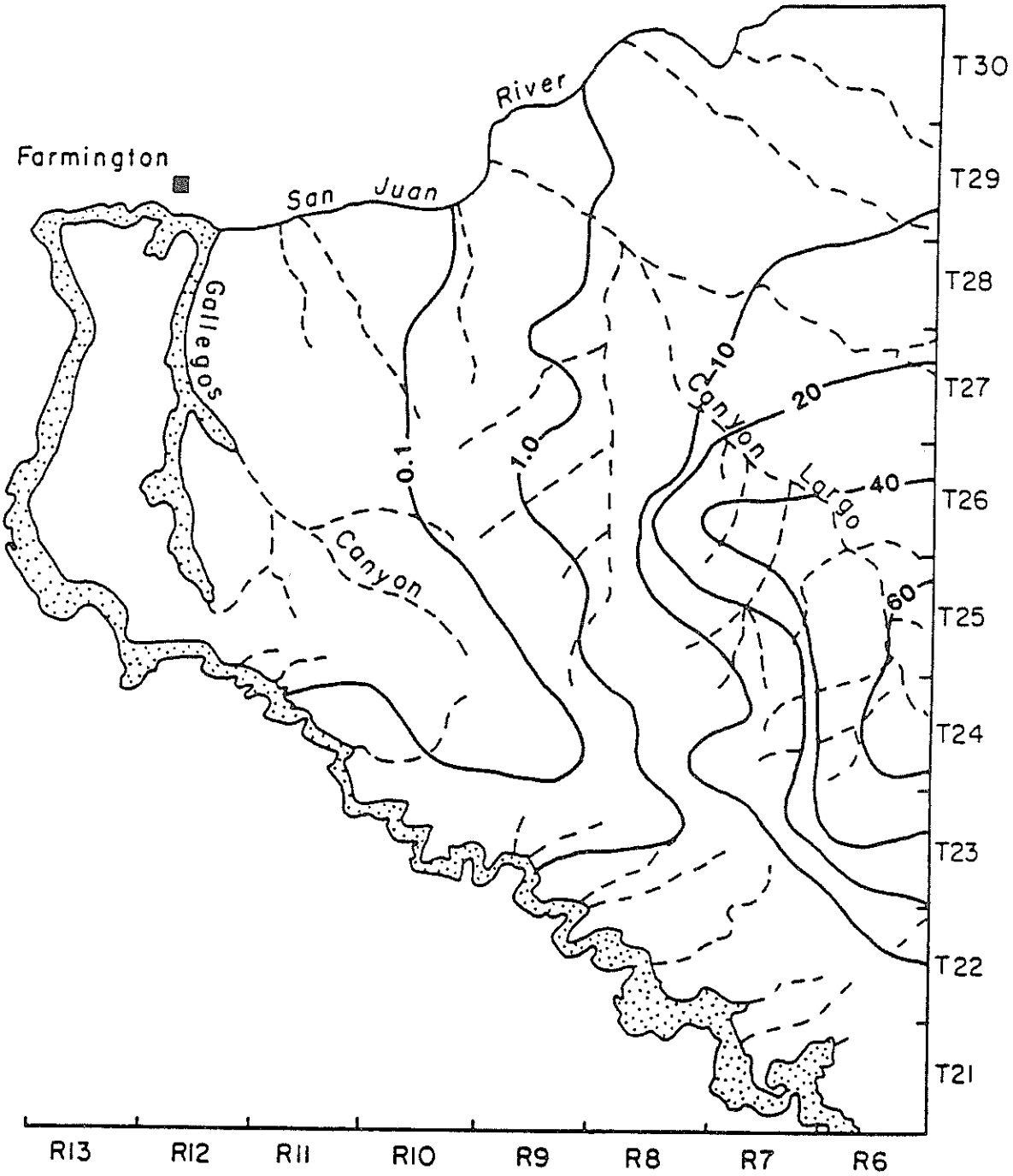

Figure 54. Drawdown (m) in the Nacimiento Aquifer After 5 Years of Pumping.

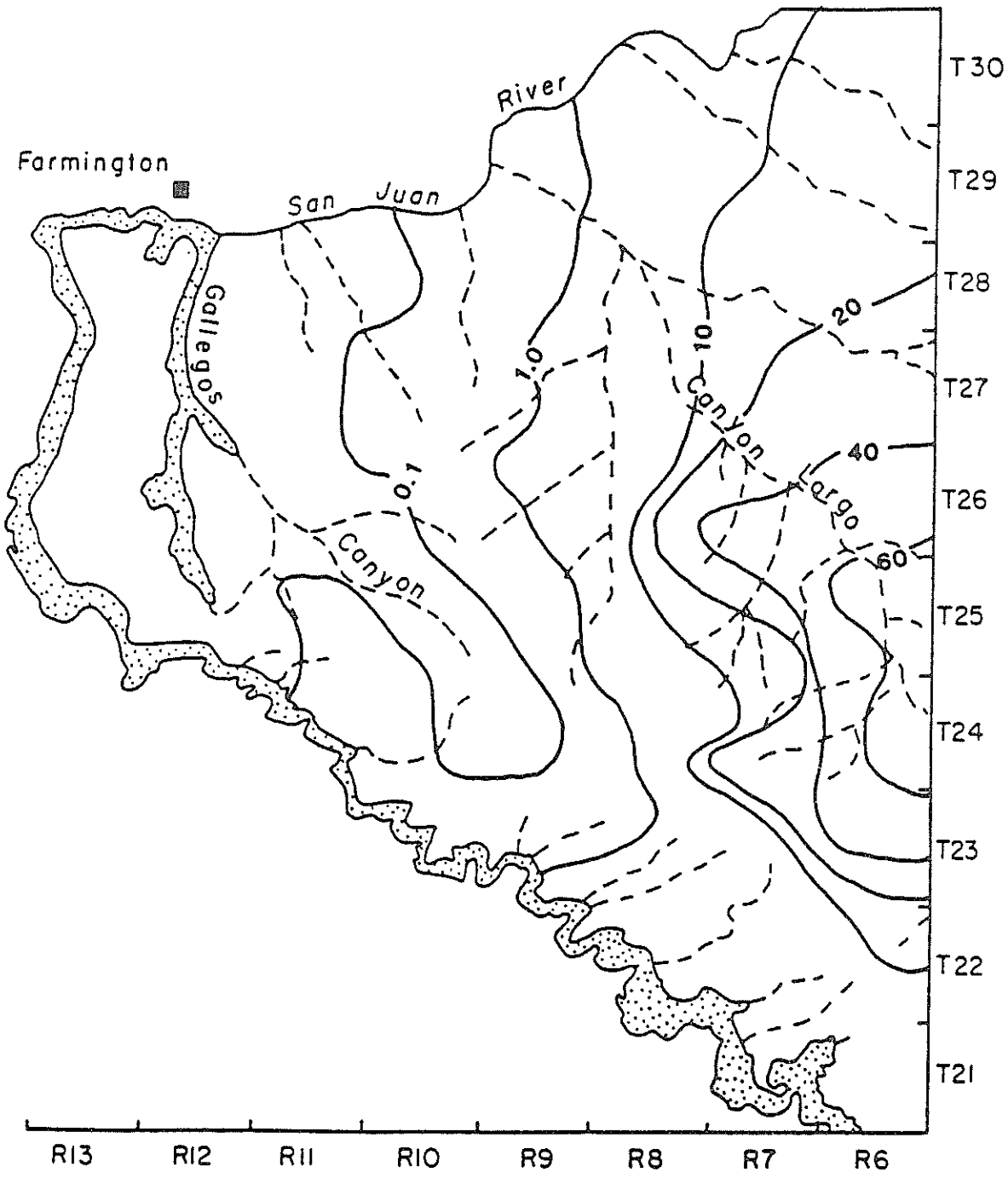

Figure 55. Drawdown (m) in the Nacimiento Aquifer After 10 Years of Pumping.

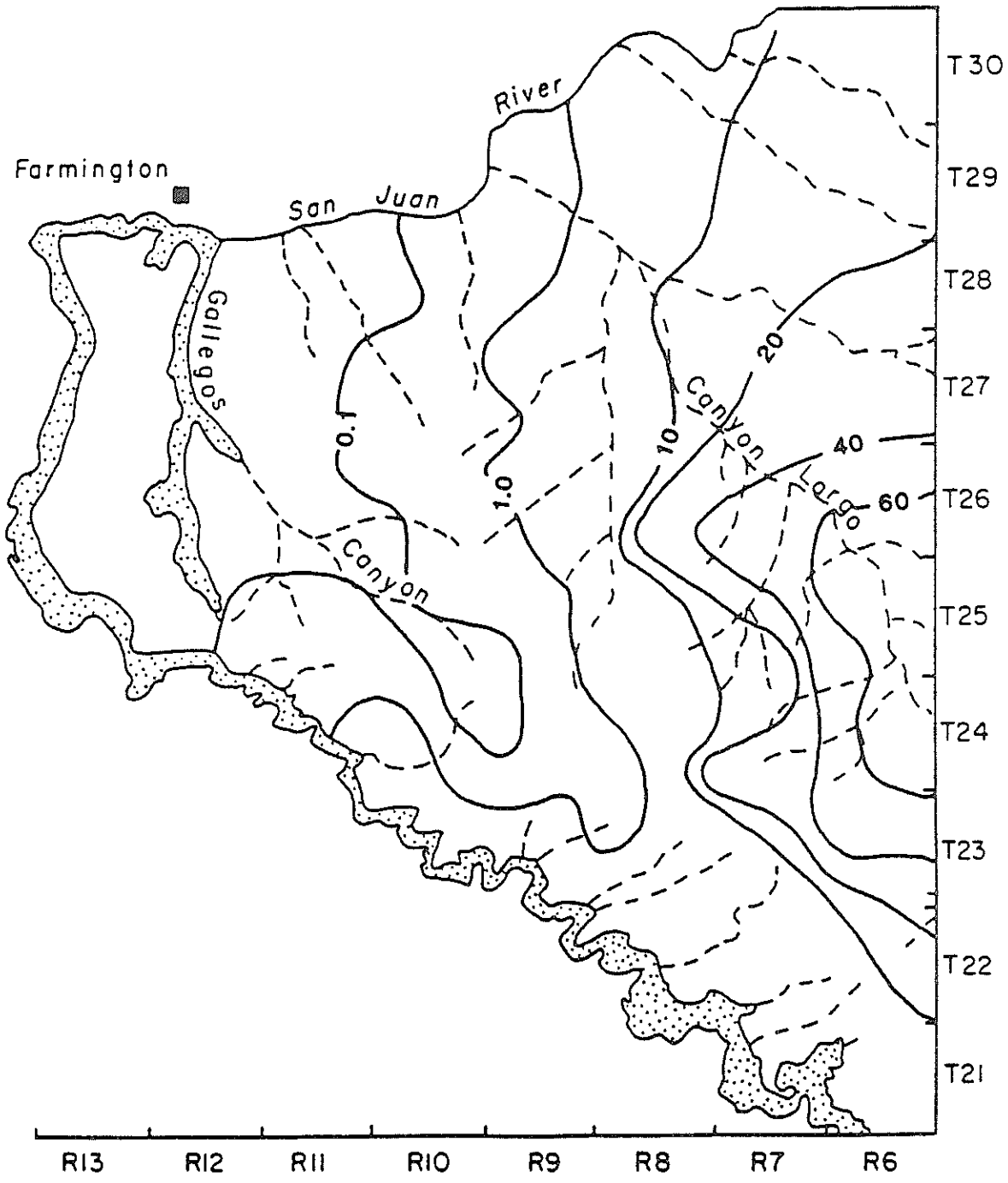

Figure 56. Drawdown (m) in the Nacimiento Aquifer After 20 Years of Pumping.

Table 13. Inflow to the San Juan River between Navajo Dam and Farmington.

Node Row	Node Colum	No Pumping Flux cfs	No Pumping Head[1/] ft	Pumping Hydraulic Heads in the Nacimiento (ft) 5 Years	10 Years	20 Years	Pumping Fluxes to the San Juan River 5 Years	10 Years	20 Years
4	4	1.0	5,391	5,391	5,391	5,391	NC[2/]	NC	NC
4	5	0.4	5,481	5,481	5,481	5,481	NC	NC	NC
4	6	1.4	5,511	5,511	5,511	5,511	NC	NC	NC
4	7	1.6	5,563	5,563	5,563	5,563	NC	NC	NC
4	8	1.5	5,651	5,651	5,651	5,651	NC	NC	NC
3	9	2.5	5,659	5,658	5,658	5,658	NC	NC	NC
2	9	0.8	5,660	5,659	5,659	5,659	NC	NC	NC
1	11	-0.3[3/]	5,715	5,707	5,700	5,696	-0.6	-0.9	-1.0
1	12	-0.8[3/]	5,709	5,698	5,688	5,683	-1.2	-1.6	-1.8

1/ These hydraulic heads were obtained from the transient simulation without pumping.

2/ NC indicates no change in flux.

3/ Aquitard hydraulic conductivity was estimated from the adjacent downstream node.

Formation. Generally, the results indicate that little change occurs during the 20-year simulation except in the vicinity of Navajo Reservoir. The two grids most significantly affected were nodes (1, 11) and (1, 12). In these nodes, the net discharge of the San Juan River to the groundwater flow system increases by 0.7 and 1.0 cfs after 20 years of pumping. These results should be regarded as qualitative at best. The uncertainty in the kriged hydraulic heads of the Nacimiento in this area is greater than 30 m. In addition, the value of the aquitard hydraulic conductivity used in the calculations was estimated from the adjacent, downstream node. This was done because the steady-state model calibration did not include calibrating the hydraulic conductivity of aquitards at boundary nodes when these aquitards were over and underlain by constant-head boundaries. This aspect of the groundwater flow model is a characteristic of the numerical code. For the transient simulations with pumping, the mass balance error for the Nacimiento was the same as for the simulations without pumping (0.001 percent difference) and the error in the Ojo Alamo mass balance improved slightly to 0.9 percent difference.

Several other features of the modeling also could have significant impacts on the validity of the quantitative analysis of the well field. The most important of these factors was the use of the San Jose Formation as a constant head boundary in the transient simulation. Due to this boundary condition, the leakage occurring naturally from the San Jose to the Nacimiento was increased by the drawdown due to the pumping. A more realistic simulation would allow the hydraulic head in the San Jose Formation to change as a result of the pumping. This would cause the leakage rate to be less than the simulated one and, consequently, the drawdowns would be larger.

The computed drawdowns cannot, however, be considered to represent simple minimum drawdowns. In any groundwater-pumping analysis, the effect of groundwater storage in both the aquifers and aquitards should be considered. In this study, a mean value

based on published data was used for aquifer storativity. Undoubtedly, the storage coefficient is not a constant value throughout the study area. Although storativity does not have as marked an influence on magnitude of drawdown as does transmissivity, it does have a proportional relationship with respect to the radius of influence of the cone of depression. This potential error would have some impact on the leakage/recharge rates occurring between the groundwater flow system and the San Juan River.

Another aspect of this numerical model is that it neglects the effect of storage of groundwater in the aquitards. In a more realistic model, the inclusion of aquitard storativity would tend to reduce the magnitude of the early-time drawdown. Finally, in this simulation, the groundwater pumping did not cause dewatering of the aquifers and, therefore, the use of a confined storage coefficient was apparently appropriate. A more realistic model might require the use of unconfined storage coefficients to simulate aquifer dewatering, should it occur.

SUMMARY

Potentiometric surface maps for the Pictured Cliffs Sandstone, Ojo Alamo Sandstone, Nacimiento Formation, and the San Jose Formation were presented. Geostatistical estimation was employed to develop the figures. In these formations, groundwater flow is generally from the southern outcrop areas toward the intersection of their northern outcrops with the San Juan River. Groundwater flowing in the San Jose Formation is also influenced by the western termination of the formation and the deep canyons disecting it. These factors cause groundwater in the San Jose to flow in a more westerly direction.

In addition, groundwater flow between the formations occurs. Over most of the study area, this flow is vertically downward. Along the San Juan River and in the vicinity of some of the larger canyons, groundwater flow is upward. In the northeastern part of the study area, the vertical flow pattern is complicated and additional data would be required before a high degree of confidence can be placed in the results.

Groundwater dating using carbon-14 and carbon-13 was performed. Ages were calculated using five methods of correcting for aqueous carbonate chemistry. The ages determined by these methods agreed satisfactorily. A range from modern to time dating back to 35,000 years was obtained for waters in the study area. The distribution of ages in the Nacimiento Formation and Ojo Alamo Sandstone form a pattern consistent with the directions of flow inferred from the hydraulic gradients. Ages and flow directions did not form such a reasonable pattern for the San Jose Formation.

A quasi-three-dimensional groundwater flow model was developed by calculating transmissivities from groundwater ages, hydraulic gradients, and statistically estimated formation thicknesses. Calibration of the model was completed by adjust-

ing aquitard hydraulic conductivity from preliminary estimates based on measured thermal gradients. The constant head boundary conditions employed in the steady state calibration were converted to equivalent constant flux boundaries for a transient simulation of a proposed future well field. The model predicts that significant water level changes will result from the groundwater pumping and that some depletion in surface flows in the San Juan River will occur.

CONCLUSIONS AND RECOMMENDATIONS

This study has employed several innovative methods in an attempt to obtain a reasonably quantitative analysis of regional groundwater flow in the Tertiary aquifers of the central San Juan Basin. From a fundamental perspective, these methods are as valid as the more standard approaches. In this case, the use of groundwater dating and the various statistical methods allowed for the development of quantitative insight into the regional groundwater flow system prior to the occurrence of any major groundwater development. This quantitative method should provide useful information to individuals, commerical interests, and government agencies concerned with the future development of groundwater resources in the San Juan Basin.

In the discussion sections, an effort has been made to evaluate the validity of the methods and results developed during this study. One of the benefits of the geostatistical technique was to provide a quantitative evaluation of the confidence to be placed in the study results. Clearly, this groundwater flow model is not an exact representation of field conditions, but it does provide a hydrologically useful tool for the understanding and evaluation of potential impacts from future groundwater development. Hopefully, future studies, employing both inovative and traditional methods, will be undertaken to improve the numerical model and the general understanding of the hydrology of the San Juan Basin.

BIBLIOGRAPHY

Anderholm, S.K. 1979. Hydrogeology and water resources of the Cuba Quadrangle, Sandoval and Rio Arriba Counties, New Mexico: New Mexico Institute of Mining and Technology, M.S. Thesis.

Bakr, A.A; Gelhar, L.W.; Gutjahr, A.L.; and MacMillan, J.R. 1978. Stochastic analysis of spatial variability in subsurface flows 1. comparison of one- and three-dimensional flow. Water Resources Research.

Baltz, E.H. 1967. Stratigraphy and regional tectonic implications of part of the upper Cretaceous and Tertiary rocks, east-central San Juan Basin, New Mexico: U.S. Geological Survey Profession Paper 552.

Baltz, E.H. Jr.; and West, S.W. 1967. Groundwater resources of the southern part of the Jicarilla Apache Indian Reservation and adjacent areas, New Mexico: U.S. Geological Survey, Water Supply Paper 1576-H.

Berry,F.A.F 1959. Hydrodynamics and geochemistry of the Jurassic and Cretaceous systems in San Juan Basin, northwestern New Mexico and southwestern Colorado: Stanford University, PhD Dissertation.

Bredehoft, J.D.; and Papadopulos, I.S. 1965. Rates of vertical groundwater movement estimated from the earth's thermal profile: Water Resources Research, 1, 325-328.

Brimhall, R.M. 1973. Ground water hydrology of Tertiary rocks of the San Juan Basin, New Mexico: Four Corners Geological Society Memoir, p. 197-207.

Brown, D.R. 1976. Hydrogeology and water resources of the Aztec quadrangle, San Juan County, New Mexico: M.S. Thesis, New Mexico Institute of Mining and Technology, p. 174.

Craigg, S.E. 1980. Hydrogeology and water resources of the Chico Arroyo-Torreon Wash area, McKinley and Sandoval Counties, New Mexico: M.S. Thesis, New Mexico Institute of Mining and Technology.

Davis, S.N.; and Bentley, H.W. 1982. Dating groundwater, A short review. Nuclear and Chemical Dating Techniques: Interpreting the Environmental Record (Currie, L.A., ed.) A.C.S. Symposium Series, No. 176.

Freeze, R.A.; and Cherry, J.A. 1979. Groundwater, Prentice-Hall, Inc., New Jersery.

Friedmann, I.; and O'Neil, J.R. 1977. Compilation of stable isotope. Fractionalization factor of geochemical interest, U.S. Geological Survey Profession Paper 440-KK.

Gabin, V.L.; and Lesperance, L.E. 1977. New Mexico climatological data, W.K. Summers and Associates, Socorro, New Mexico, p. 436.

Gelhar, L.W.; Gutjahr, A.L.; and Naff, R.L. 1979. Stochastic analysis of macrodispersion in a stratified aquifer: Water Resources Research, 15(6), p. 1387-1397.

Gelhar, L.W.; and Gutjahr, A.L. 1982. Stochastic solutions of the one-dimensional convective dispersion equation: New Mexico Institute of Mining and Technology, Report No. H-11, p. 20.

Gutjahr, A.L.; Gelhar, L.W.; Bakr, A.A.; and MacMillan, J.R. 1978. Stochastic analysis of spatial variability in subsurface flows 2. evaluation and application. Water Resources Research 14(5), p. 953-959.

Ingerson, C.W.; and Pearson, F.J. 1964. Estimation of the age and rate of groundwater by the ^{14}C method: Recent Research in the Field of Hydrosphere, Atmosphere, and Nuclear Geochemistry, Sugawara Fiestal, Mauzen Co., Tokyo, p. 263-283.

Kelley, V.C. 1950. Regional structure of the San Juan Basin: New Mexico Geological Society Guidebook, 1st field conference, p. 101-108.

Lyford, F.P. 1979. Groundwater in the San Juan Basin of New Mexico and Colorado: U.S. Geological Survey, Water Resources Investigations 79-73.

Mansure, A.J.; and Reiter, M. 1979. A vertical groundwater movement correction for heat flow: Journal of Geophysical Research, 84, p. 3490-3496.

Mook, W.G. 1972. On the reconstruction of the initial C-14 content of ground water from chemical and isotopic composition: Proc. VII Int. Conf. on C-14, Lower Hutf, New Zealand.

Mook, W.G. 1976. The dissolution-exchange model for dating groundwater with carbon-14: Interpretation of Environmental Istope and Hydrochemical Data in Groundwater Hydrology, IAEA, Vienna, p. 213-225.

Neretniks, I. 1980. Diffusion in the rock matrix: an important factor in radionuclide retardation. Journal of Geophysical Research (85), p. 4379-4397.

Nir, A.; and Lewis, S. 1975. On tracer theory in geophysical systems in steady and non-steady state, 1: Tellus, 27, p. 372-382.

Phillips, F.M.; Peeters, L.A.; and Tansey, M.K. 1984. An isotopic investigation of ground-water resources in the Ojo Alamo Sandstone, San Juan Basin: New Mexico Water Resources Research Institute Technical Report, p. 104.

Plummer, L.N.; Parkerst, D.L.; and Thorstenson, D.C. 1983. Development of reaction models for ground-water systems. Journal Geochimica et Cosmochimica Acta, 47, p. 665-686.

Powell, J.S. 1972. Paleontology and sedimentation models of the Kimbeto member of the Ojo Alamo Sandstone: Four Corners Geological Society Memoir, p. 111-122.

Renick, B.C. 1931. Geology and ground water resources of western Sandoval County, New Mexico: U.S. Geological Survey, Water Supply Paper 525-C.

Sokol, D. 1971. Ground water safety evaluation - Project gasbuggy. U.S. Atomic Energy Commission, Las Vegas, Nevada.

Stephens, D.B. 1983. Groundwater flow and implications for groundwater contamination north of Prewitt, New Mexico, USA: Journal of Hydrology, 61, p. 391-401.

Stone, W.J. 1979. Water-key to energy production, northwest New Mexico, USA: Third World Congress on Water Resources, Mexico City, p. 868-877.

Stone, W.J. et al. 1983. Hydrogeology and water resources of San Juan Basin, New Mexico: New Mexico Bureau of Mines and Mineral Resources Hydrologic Report 6, p. 70.

Sudicky, E.A.; and Frind, E.O. 1981. Carbon-14 dating of groundwater in confined aquifers: implications of aquitard diffusion. Water Resources Research, 17(4), p. 1060-1064.

Suess, H.E. 1980. The radiocarbon record in tree rings of the last 8,000 years. Proc. Tenth Int. Radiocarbon Conf. Bern, Radiocarbon 22(3), p. 200-209.

Tamers, M.A. 1967. Surface-water infiltration and groundwater movement in arid zones of Venezuela: Isotopes in Hydrology, IAEA, Vienna, p. 339-351.

Tamers, M.A. 1975. Validity of radiocarbon dates on groundwater: Geophysical Survey, 2, p. 217-239.

Vogel, J.C. 1967. Investigation of groundwater flow with radiocarbon: Isotopes in Hydrology, IAEA, Vienna, p. 355-368.

Vogel, J.C. 1970. Carbon-14 dating of groundwater: Isotope Hydrology 1970, IAEA, Vienna, p. 235-237.

Wood, W.W. 1981. A geochemical method of determining dispersivity in regional groundwater systems. Journal of Hydrology (54), p. 209-244.

EXPLANATION

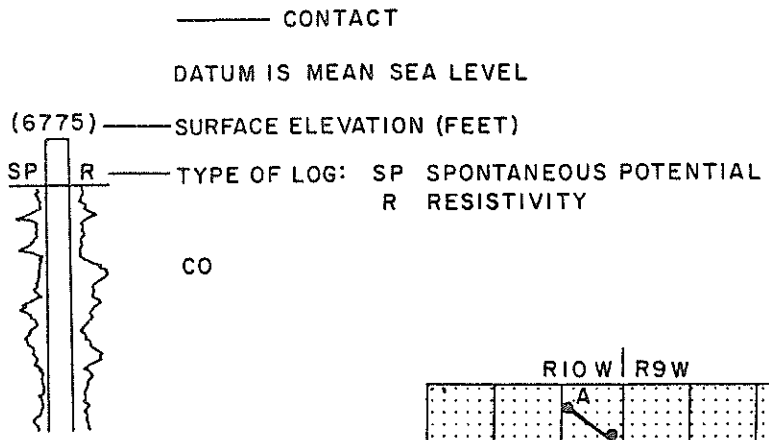

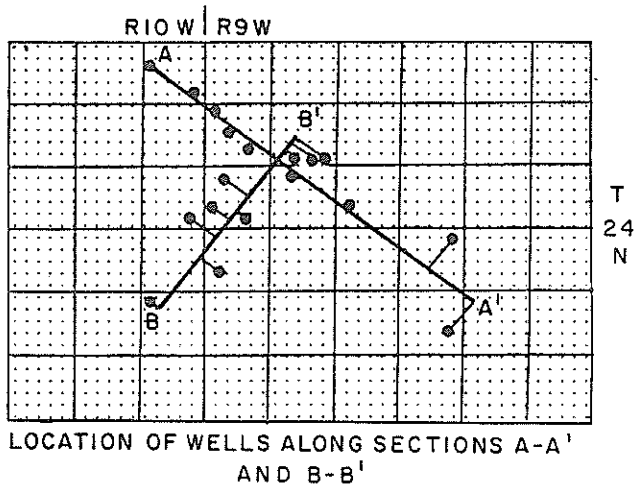

LOCATION OF WELLS ALONG SECTIONS A-A' AND B-B'

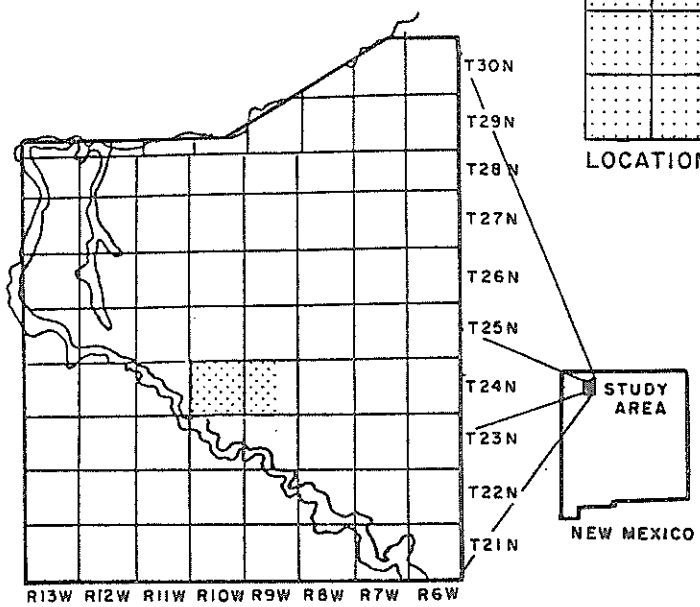

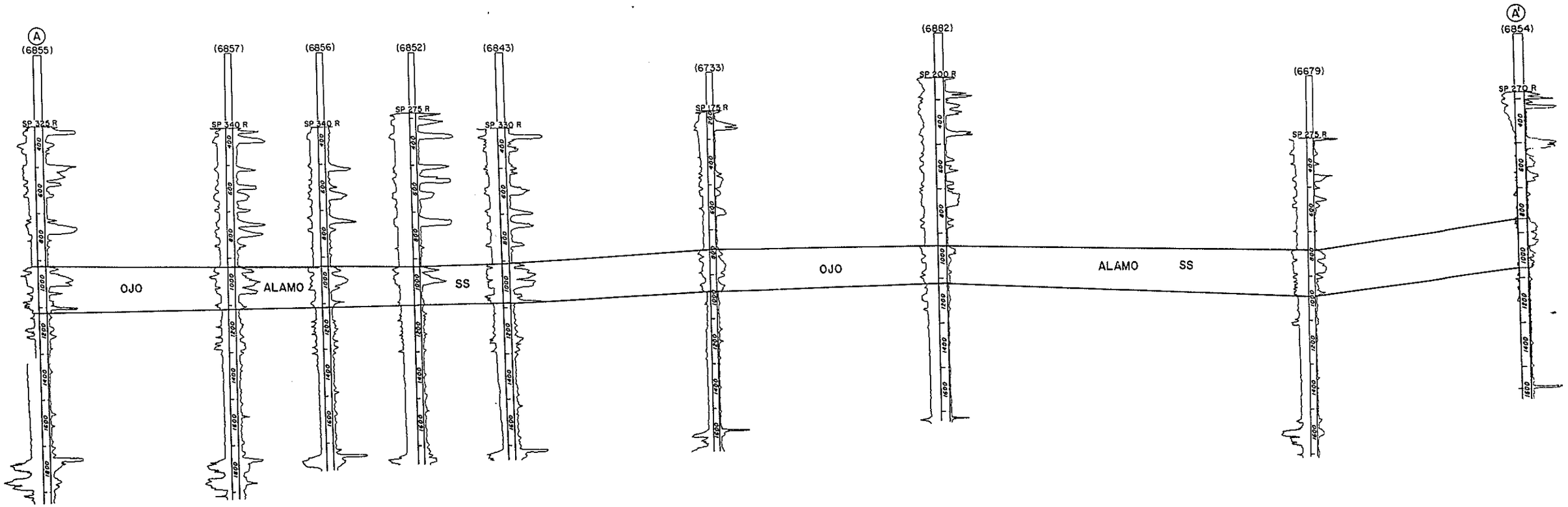

FIGURE 7. ELECTRIC LOGS ALONG DIP OF UNIT

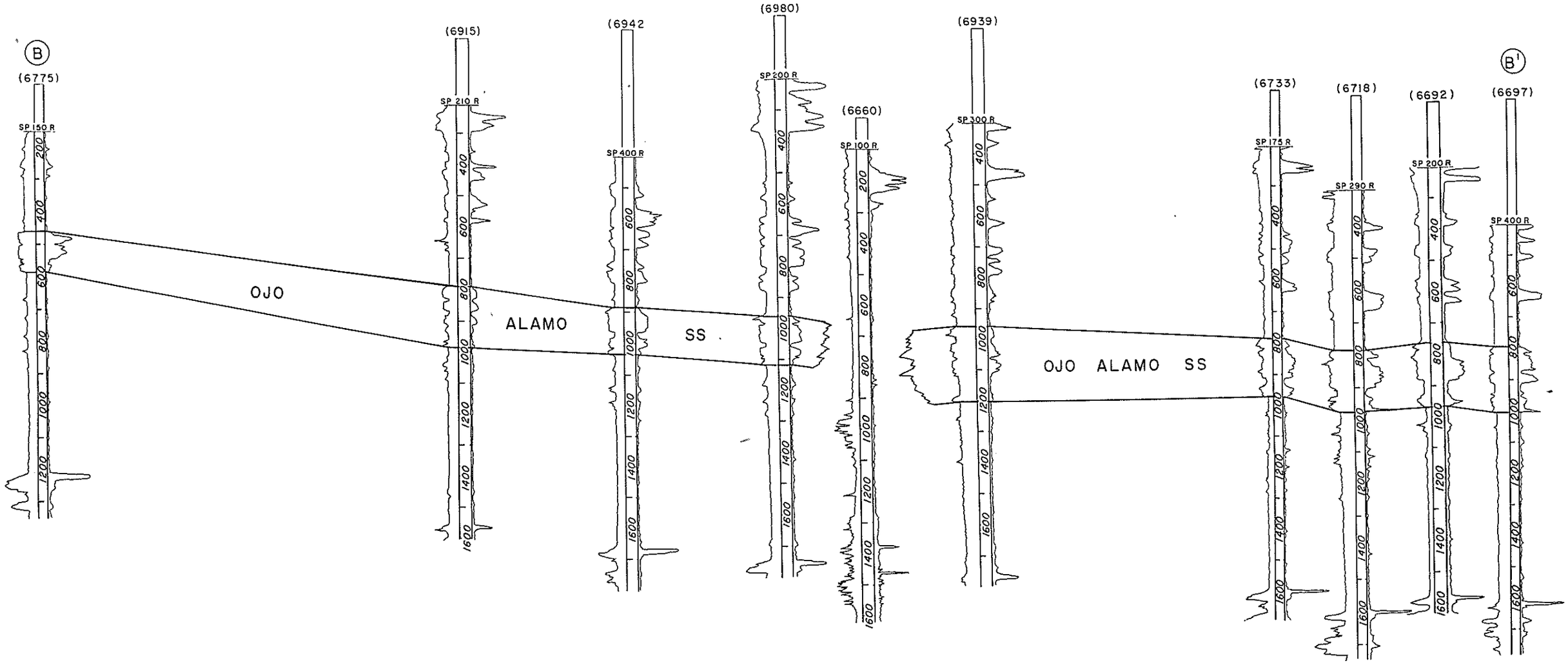

FIGURE 8. ELECTRIC LOGS ALONG STRIKE OF UNITS

APPENDIX II

Procedure for sampling of water for carbon-14 analysis.

1. Fill a 50 liter carboy with water leaving room for additional reagents. Do not let the water sample come in contact with the atmosphere and avoid introducing extraneous material.

2. Add some sample water to a vial containing 5 grams of ferrous sulfate and shake. Add to sample container and mix thoroughly.

3. Add 0.5 liter of saturated barium chloride solution and mix thoroughly.

4. Add enough "carbonate free" solium hydroxide solution to bring the pH of the water sample above 10.0.

5. Add 40 ml of Percol 156, and stir rapidly.

6. Allow barium carbonate to precipitate out.

7. Add an additional amount of barium chloride to water sample to ensure complete precipitation. If the solution shows any cloudiness, add more barium chloride.

8. After all the barium carbonate has settled to the bottom, carefully decant off the water sample. Pour the precipitate into container and cap tightly. Seal with molten max and label.

9. Rinse out the carboy with sample water and 1 N HCl.